Dynamics of Droplet Shedding and Coalescence under the Effect of Shear Flow

SARA MOGHTADERNEJAD

A Thesis

in

the Department

of

Mechanical and Industrial Engineering

Presented in Partial Fulfillment of the Requirements

for the Degree of Doctor of Philosophy (Mechanical Engineering) at

Concordia University

Montreal, Quebec, Canada

August 2014

School of Graduate Studies

This is to certify that the thesis prepared,

By: SARA MOGHTADERNEJAD

Entitled: Dynamics of Droplet Shedding and Coalescence under the Effect of Shear Flow

and submitted in partial fulfillment of the requirements for the degree of

Doctor of Philosophy (Mechanical Engineering)

Complies with the regulations of the University and meets the accepted standards with respect to originality and quality.

Signed by the final examining committee:

Dr. A. Aghdam	Chair
Dr. L. Kadem	Examiner
Dr. H. Ng	Examiner
Dr. K. Khorasani	External to the department
Dr. M. Charmchi	External to the university
Dr. N. Esmail	Co-Supervisor
Dr. A. Dolatabadi	Co-Supervisor

Approved by _____

Chair of Department or Graduate Program Director

Date _____

Abstract

DYNAMICS OF DROPLET SHEDDING AND COALESCENCE UNDER THE EFFECT OF SHEAR FLOW

SARA MOGHTADERNEJAD, Ph.D.

Concordia University, 2014

Droplet shedding and coalescence has various industrial applications from ink-jet printing to ice accretion on wind turbine blades, power lines or aircrafts. It is known that the incipience of icing phenomenon in the mentioned applications arises from the shedding and coalescence of the rain droplets. The coalesced droplets then start to form a runback flow and when temperature is below the water freezing point, ice can be accumulated on these structures which alters the performance in the mentioned technologies. Accordingly this work is dedicated to a fundamental study on dynamics of droplet shedding and coalescence as a preliminary stage of ice formation.

Sessile droplets are deposited on surfaces where various air flows are introduced to them for analyzing their shedding behavior. As it is believed that using superhydrophobic coatings decreases the amount of ice accumulation on the solid surfaces, the effect of different surface wettabilities ranging from hydrophilic to superhydrophobic is also studied on droplet dynamics.

It is shown that on a hydrophilic substrate when the air speed is high enough, rivulets are formed from merging droplets. In contrast, on a superhydrophobic substrate there is no rivulet formation. Instead coalesced droplets roll on the surface and detach from it if the air speed is sufficiently high. In addition, the results indicate a contrast in the mechanism of the coalescence and subsequent detachment between a single and two droplets on a superhydrophobic surface. At

low air speeds, the two droplets coalesce by attracting each other before detaching with successive rebounds on the substrate, while at higher speeds the detachment occurs almost instantly after coalescence, with a detachment time decreasing exponentially with the air speed.

A wind tunnel experiment was designed to characterize the rivulet dynamics on various surface wettabilities. Smoothed Particle Hydrodynamics method was performed and its results were compared with the ones obtained from the experiments. The results indicate that increasing the air speed results in formation of waves with higher frequency in comparison with the lower air speeds. It was also demonstrated that as on superhydrophobic substrates instead of rivulets series of droplets are formed these substrates can be suitable candidates for anti-icing purposes.

Contribution of Authors

This thesis is prepared in manuscript format. Except chapter 1 and 7 that are thesis introduction and conclusion the rest of the chapters are submitted to scientific journals. The first author of these manuscript is Ms. Sara Moghtadernejad who is the author of the current thesis. As the first author of the manuscripts, Sara Moghtadernejad was responsible for designing and conducting all the experiments and post processing the results. She has also performed the simulation mentioned in chapter 6, based on Smoothed Particle Hydrodynamics Method (SPH). In the following section the name of the journals to which the papers are submitted and the contribution of the co-authors will be given in detail.

Chapter 2 entitled “Shear Driven Droplet Shedding on Surfaces with Various Wettabilities” is a published paper in SAE International Journal of Aerospace, volume 6, pages 459-464, 2013. This work has been co-authored by Mr. Morteza Mohammadi, Mr. Mehdi Jadidi, Dr. Moussa Tembely, and Prof. Ali Dolatabadi. Mr. Mohammadi and Jadidi helped the first author in approximately 25% of the experimental work. Dr. Tembely has contributed in editing the manuscript and Prof. Ali Dolatabadi is the supervisor of the project.

Chapter 3 entitled “Shear Driven Droplet Coalescence and Rivulet Formation” is submitted to the Journal of Mechanical Engineering Science. This works has been co-authored by Mr. Jadidi who helped the first author in 25% of the experimental work. Research supervisors, Prof. Ali Dolatabadi and Prof. Nabil Esmail are the other co-authors of the paper.

Chapter 4 entitled “Shear Driven Droplet Shedding and Coalescence on a Superhydrophobic Surface” is submitted to the Physics of Fluids Journal. This work has been co-authored by Dr. Tembely who has performed the simulation part of the work based on Volume of Fluid (VOF)

coupled with Large Eddy Simulation (LES) turbulence model. Mr. Jadidi has helped the first author in 25% of the experimental work. Prof. Esmail and Prof. Dolatabadi are the research supervisors.

Chapter 5 entitled “Concurrent Droplet Coalescence and Solidification on Surfaces with Various Wettabilities” is submitted to the ASME Journal of Fluids Engineering. This works has been co-authored by Mr. Jadidi and Dr. Tembely who helped the first author in 25% of the experimental work and manuscript editing, respectively. Prof. Esmail and Prof. Dolatabadi are also the co-authors and research supervisors.

Chapter 6 entitled “Experimental and Numerical Analysis of Rivulet Dynamics on Surfaces with Various Wettabilities” is submitted to the SAE International Journal of Aerospace. This work has been co-authored by Mr. Jadidi who helped the first author in 25% of the experimental work and the research supervisors that are Prof. Esmail and Prof. Dolatabadi.

To my parents for their love, encouragement and endless support during my life.

Acknowledgements

I would like to, cordially, thank my supervisors Prof. Nabil Esmail and Prof. Ali Dolatabadi for their helpful ideas, comments and supports during my PhD. They have been wonderful guides for me and their advice have been priceless. I would like to thank them for encouraging me with my research during these years and allowing me to grow as a research scientist.

I would also like to acknowledge NSERC, Bombardier aerospace and Pratt& Whitney Canada for their financial support to several parts of this study. I would like to thank Dr. Moussa Tembely and Mr. Mahmoud Reza Aghighi for their helpful comments and ideas that enriched this study remarkably. Their efforts and contributions are highly appreciated. I appreciate my committee members for their useful feedback and brilliant comments during my proposal. I would like to thank Mr. Mehdi Jadidi for helping me in several experimental part of this project. Also I would like to thank my colleague Mr. Hany Gomaa for his endless help during the time I was studying at Concordia. I also appreciate the helps of Mr. Rudi Krueger, Mr. Milad Mousavi and other colleagues from the multiphase flow lab.

Finally and most importantly, I would like to thank my parents, Mrs. Mahvash Safa and Dr. Mahmoud Moghtadernejad, without them I could not make it this far. I would also like to thank my dearest, Saviz Moghtadernejad, and Behzad Mehrdad, for their understanding and encouragement in many moments of crisis.

Thank you Lord for being there for me.

This thesis is only the beginning of my journey.

Table of Contents

List of Figures

List of Tables

Nomenclature

A	Particle attribute
A_s	Smoothed particle attribute
B	Fluid bulk modulus of elasticity, $\left(\frac{kg}{m.s^2}\right)$
c	Sound speed, $\left(\frac{m}{s}\right)$
Ca	Capillary number
C_D	Drag coefficient
D	Droplet diameter, (m)
F	Force, $\left(\frac{m}{s^2}\right)$
f	Accumulated force term, $\left(\frac{N}{m^3}\right)$
f_H	Hoffman function
$\boldsymbol{F}_p$	Pressure field over the droplet surface, (Pa)
F_σ	Surface tension force, (N)
g	Gravitational acceleration, $\left(\frac{m}{s^2}\right)$
G	LES kernel
H	Maximum depth of the fluid, (m)
h	Width of the kernel, (m)
I	Turbulent intensity
k	Stiffness of the fluid, $\left(\frac{m^2}{s^2}\right)$
k_{sgs}	Turbulent SGS kinetic energy, $\left(\frac{m^2}{s^2}\right)$
L	Tube length, (m)
L_w	Wetting length, (m)
m	Mass, (kg)
$\boldsymbol{n}$	Face unit normal vector
Oh	Ohnesorge number
P	Pressure, (Pa)
r	Position vector, (m)
Re	Reynolds number

R_{eff}	Effective radius of the droplet, (m)
R_f	Roughness factor
S	Projected area of the droplet, (m^2)
$\bar{S}$	Rate of strain tensor, $(\frac{1}{s})$
T_s	Surface temperature (℃)
t	Time, (s)
u_{air}	Air velocity magnitude in the flow direction, $\left(\frac{m}{s}\right)$
U_{cl}	Contact line velocity, $\left(\frac{m}{s}\right)$
V_o	Inlet velocity, $\left(\frac{m}{s}\right)$
W	Smoothing kernel, $\left(\frac{1}{m^3}\right)$
w	Width of the droplet perpendicular to the moving direction, (m)
We	Weber number
Z	Droplet height, (m)
α	Volume fraction
Δ	Filter width in LES method, (m)
ε_t	Turbulent dissipation, $\left(\frac{m^2}{s^3}\right)$
θ	Contact angle, (°)
κ	Interface curvature
ν_{sgs}	Turbulent viscosity, $\left(\frac{m^2}{s}\right)$
ξ	Fractional geometrical area
ρ	Density, $\left(\frac{kg}{m^3}\right)$
σ	Surface tension, $\left(\frac{N}{m}\right)$
τ	Experimental time scale, (s)
φ	Volume flux, $\left(\frac{m^3}{s}\right)$
μ	Dynamic viscosity, $\left(\frac{\mathrm{kg}}{m.s}\right)$
LES	Large eddy simulation
SPH	Smoothed particle hydrodynamics
VOF	Volume of fluid

Subscripts

adh	Adhesion
drop	Droplet
g	Gas
inj	Surface hole
l	Liquid
lg	Liquid-gas
max	Maximum
min	Minimum
sg	Solid-gas
sgs	Sub-grid scale
sl	Solid-liquid
w	Water

Chapter 1

Introduction

Droplet dynamics is a subject which is involved in different scientific and industrial applications such as ink-jet printing, spray coating, as well as ice accretion on wind turbine blades, power lines and airfoils [1-4]. The motivation of the present work however comes from the fact illustrated in Figure 1.1 where on a surface with low adhesion to water no ice accumulation is observed. In contrast on a hydrophilic surface (such as aluminum with high adhesion to water) substantial amount of ice is accumulated. Being able to control the amount of accumulated ice on surfaces such as turbine bales or airfoils is of utmost importance for industries due to the hazards of icing phenomenon on their surfaces. In aircraft icing condition for example, the performance of the aircraft will be significantly affected by accumulation of ice on its wings; there will be a decrease in the maximum lift and the stall angle [5, 6]. If ice is gathered on the span wise section of the aircraft wings, the flow over the aileron changes leading to variation in hinge moments of control [6]. In addition, in small aircrafts, the added weight of the accreted ice can be another harmful effect. Hence, ice creation distorts aircraft aerodynamics and may cause serious damages. As a result, preventing ice from adhering to the airfoil or removing it, once it has been adhered is very important. In other words, developing better de-icing or anti-icing systems for aircrafts is a critical point in aerospace industry. Apparently optimized system design cannot be delivered for these cases while there is a lack of full understanding of droplet dynamics.

It is known that icing phenomenon that occurs on wind turbine power lines or aircrafts is mainly driven by rain droplets shedding and coalescence due to air shear effect. The coalesced droplets turn into narrow streams of water known as rivulets and in subzero temperatures ice will be accumulated on the substrates. There is a variety of parameters that are involved in icing phenomenon such as surface wettability, shedding and coalescence mechanism, and the effect of shear flow and temperature variations, among many others. Hence in the following sections a brief description of surface wettability and shear driven droplet dynamics is provided to shed more light in the fundamentals of these subjects.

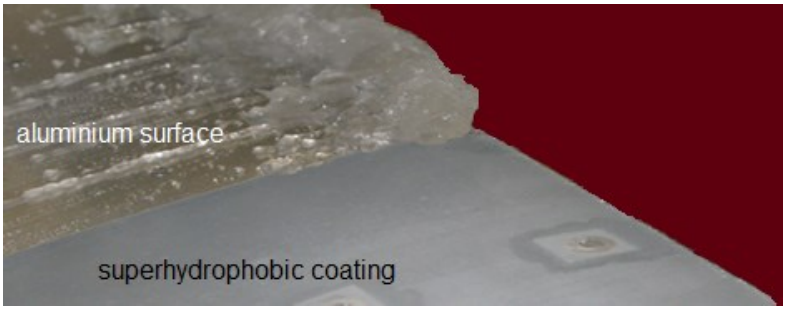

Figure 1.1 Performance of a superhydrophobic coating compared to aluminum surface in icing conditions

1.1 Surface Wettability

The wettability of a surface is typically demonstrated by the surface contact angle. Under static conditions, when a droplet is placed on a surface, the angle between the droplet and the surface is called the static contact angle (see Figure 1.2). Based on different surface characteristics such as surface energy and its roughness this value is subject to change. The contact angle that a liquid makes with an ideal (rigid, flat, chemically homogeneous, insoluble and nonreactive) solid surface is called "intrinsic" contact angle and can be calculated from Equation 1.1 (Young's equation [7]);

$$cos\,\theta = (\sigma_{sg} - \sigma_{sl})/\sigma_{lg}$$ **Equation 1.1**

where θ is the intrinsic contact angle. σ_{sg}, σ_{sl} and σ_{lg}, are the solid-gas, solid-liquid, and liquid-gas interfacial tensions, respectively. The schematic of Young's contact angle on a solid surface is shown in Figure 1.2.

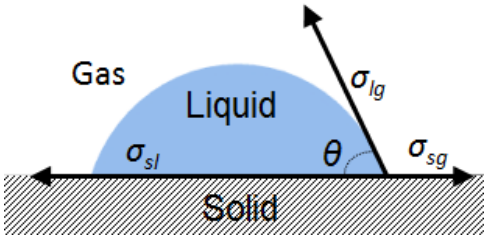

Figure 1.2 Schematic of droplet contact angle on a solid surface

In contrast to the ideal solid surfaces, real surfaces are usually chemically heterogeneous and rough. On these surfaces the contact angle is called "actual" rather than intrinsic [8]. Thus, the actual contact angle may vary from point to point and it is not clear whether its values are necessarily the same as the intrinsic ones [8]. If the static contact angle is less than 90°, the surface is called hydrophilic which means that the water droplet scatters on the surface rather than forming a spherical shape. The surface is hydrophobic when the static contact angle is between 90° and 150°, and if this angle is larger than 150°, then the surface is called superhydrophobic.

Surface chemistry is not the only factor that affects solid surfaces wettability. It is shown that surface morphology (roughness) also plays an important role on surface wettability [9]. In general there are two distinct wetting regimes for a liquid in contact with a rough solid surface. The first regime is the Wenzel regime (see Figure 1.3 a) in which the entire contact area consists of liquid and solid phases only [10]. Wenzel developed the first analytical model to determine

how roughness affects surface wettability by considering net energy decrease during the spreading of a droplet on a rough surface [11]. According to Wenzel model for a droplet in contact with a rough surface without asperities, the liquid can follow the surface topography and show strong pining [12]. Wenzel equation [11] is suitable for describing this situation

$$\cos\theta = R_f \cos\theta_0 \qquad \textbf{Equation 1.2}$$

Where the contact angles of rough and smooth surfaces are denoted by θ and θ_0, respectively. In addition the roughness factor (R_f), is defined as the ratio of the total surface area of the rough surface to its apparent area. The roughness factor is equal to 1 if the surface is flat. In contrast, adding roughness to the surface, increases R_f [12]. Wenzel-type wetting clearly shows that the contact angle of a rough surface is different from the one of a smooth surface (intrinsic contact angle). From Wenzel model, it can be understood that if $\theta_0 > 90^o$, roughness enhances hydrophobicity. If $\theta_0 < 90^o$, the contact angle for the rough surface decreases with increasing R_f. According to Wenzel model, the roughness increases the surface area of the solid, which geometrically modifies hydrophobicity [12]. It can be shown that Wenzel equation is only valid when $-1 \leq R_f \cos\theta_0 \leq 1$.

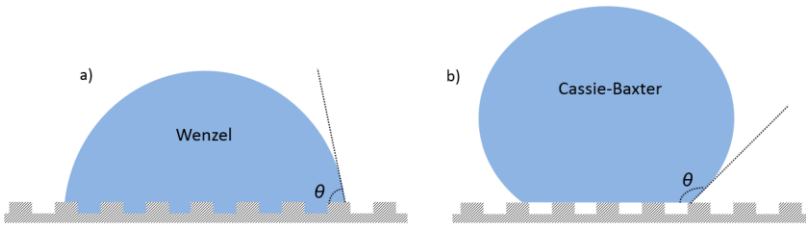

Figure 1.3 Schematic of the wetting phenomena; a) Wenzel type and b) Cassie-Baxter type

The second wetting regime which is suitable for describing the wettability of high roughness surfaces is called the Cassie and Baxter regime [11] in which the contact area consists of liquid, solid and gas phases (see Figure 1.3 b). For surfaces with high roughness, a wetting liquid is

completely adsorbed by the rough surface cavities while a non-wetting liquid may not penetrate into surface cavities [13]. As a result, air pockets will be generated between the liquid and the surface. Creation of air pockets results in having a solid-liquid-air interface. In this case, the liquid can bridge from asperity to asperity while enclosing air under it [13]. Hence, there will be two sets of interfaces: a liquid-air interface with the ambient environment surrounding the droplet, and a flat composite interface under the droplet involving solid-liquid, liquid-air, and solid-air interface. Therefore, in this situation, since Wenzel equation cannot be used, Cassie and Baxter model, modifies Wenzel's equation for the composite surfaces [14];

$$\cos\theta = R_f \xi_{sl} \cos\theta_0 - \xi_{lg} \qquad \textbf{Equation 1.3}$$

It should be noted that Equation 1.3 neither provides any particular form of dependence of the areas of the solid-liquid and liquid-gas interfaces, nor explains under which conditions the composite interface is formed [13]. In Equation 1.3, ξ_{sl} and ξ_{lg} are fractional geometrical areas of the solid-liquid and liquid-gas interfaces under the droplet, respectively. As mentioned above, according to the Cassie model, air can remain trapped below the droplet, forming air pockets. Since the droplet sits partially on air, hydrophobicity is strengthened [12].

Based on what was mentioned above it can be said that in Wenzel type of wetting, surface roughness results in an increase of surface wettability. As a result, when roughened, an intrinsically hydrophilic surface becomes more hydrophilic and an intrinsically hydrophobic surface becomes more hydrophobic. In contrast in Cassie-Baxter wetting type surface wettability reduces due to the presence of air pockets between the solid and liquid phases. Therefore when roughened in a proper manner, an intrinsically hydrophilic surface may show hydrophobic characteristics. Various geometrical parameters of surface roughness such as height of the

features, the width of the gap between features and the presence of secondary scale roughness determine the surface dominant wetting regime [15].

Superhydrophobicity

Recently, superhydrophobic surfaces have been the center of attention in industry as they are involved in various applications such as anti-icing coatings [16, 17], oil-repellent and corrosion resistance surfaces, self-cleaning purposes and turbulent reduction in water-bearing pipes [18]. The idea of superhydrophobicity comes from studying the lotus leaf wetting behavior [19] which is a natural superhydrophobic surface (see Figure 1.4). Scanning Electron Microscopy (SEM) imaging of lotus leaves surfaces shows that there is a "hierarchical" microstructure that contains micro asperities of 20– 40 μm apart. Each asperity is covered with a smaller scale "epicuticular wax crystalloids" roughness. Lotus leaf superhydrophobicity originates in these crystalloids both chemically and structurally. Other natural superhydrophobic surfaces have more or less similar structures [20]. The combination of the hierarchical roughness together with a small surface free energy material results in a superhydrophobic surface. Biomimetic superhydrophobic surfaces are widely produced based on this fact [21, 22]. Superhydrophobic surfaces can be constructed either by using low surface energy materials or by chemically treating surfaces with materials such as silicon, or wax [13]. Another technique that can be used to increase the hydrophobicity of a hydrophobic surface is to increase the surface area by increasing the surface roughness [13]. The droplet rests on various nanostructures on these surfaces, which results in the existence of air pockets under the droplets [23].

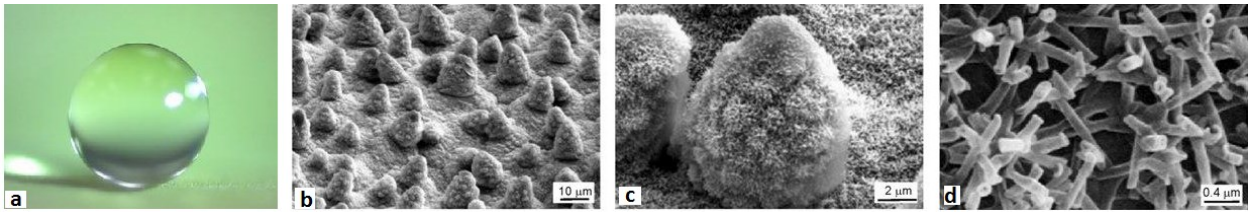

Figure 1.4 a) Water droplet sitting on the Lotus leaf; b, c, and d) SEM images of Lotus leaf with different magnifications [9]

The reason that makes superhydrophobic surfaces an ideal candidate to be used in a wide range of applications is their extreme water repellency and high water mobility properties [24]. Water repellency of superhydrophobic surfaces comes from their high contact angles (more than 150°). Water mobility on the other hand, defines how easily a droplet of water can roll and move on a surface and can be determined by contact angle hysteresis. There are different methods to measure the contact angle hysteresis on a surface; one of these methods is to tilt the plate that the droplet is resting on, until the droplet starts to move. Advancing (θ_A), receding (θ_R) and sliding (ϕ) angles are obtained from this experiment that are schematically shown in Figure 1.5. The difference between the advancing and the receding contact angles is known as the contact angle hysteresis. Smaller hysteresis results in more mobility for the droplet. For example, the contact angle hysteresis of a superhydrophobic substrate is usually less than 10° [25]. The substrate sliding angle is the angle required for the droplet to begin sliding. Apparently the smaller α, the easier the droplet moves on the substrate.

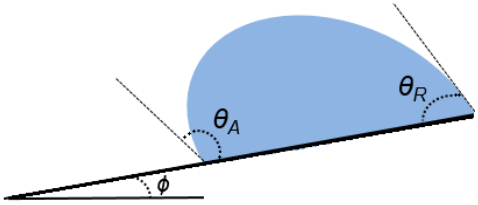

Figure 1.5 Droplet advancing (θ_A), receding (θ_R) and sliding angles (ϕ) on a tilted plate

The effect of contact angle hysteresis on hydrophobicity was first addressed in [26] by the following equation;

$$mg \sin \phi = w\sigma(\cos \theta_R - \cos \theta_A) \quad \textbf{Equation 1.4}$$

where the surface tension of the droplet, the gravitational acceleration, mass and width of the droplet perpendicular to the moving direction, are denoted by *σ, g, m* and *w*, respectively.

It is found that the variation of droplet size provides useful information about the quality of the surface [27]. Contact angle hysteresis remains invariant in hydrophilic surfaces with varying droplet size for close-to-ideal systems (homogeneous and smooth solid surfaces). For non-ideal systems with heterogeneous or rough solid surfaces, different contact angle/droplet size correlation can be found. In these systems, the contact angle hysteresis increases with decreasing the droplet size [27]. However, the advancing contact angle is much less sensitive to solid surface imperfections than the receding contact angle. Thus, the receding contact angle should receive more attention in the analysis of surface morphology. For hydrophobic surfaces, by changing the droplet size, no significant changes in the advancing contact angle were found, however the receding contact angle decreased by decreasing the droplet volume [27]. A similar variation can be observed in receding contact angles by changing the droplet size for heterogeneous, rough and unstable surfaces.

To summarize the wetting phenomenon, when a droplet is placed on a solid surface, it wets the surface to a certain degree. The amount of wetting depends on the ratio between the energy necessary for the enlargement of the surface and the gain of energy due to adsorption [20]. At equilibrium, the energy of the system is minimized. In case of water-repellent rough (hydrophobic) surfaces, air is enclosed between the droplet and surface; forming a composite interface as described with Cassie-Baxter equation which enlarges the water-air interface while

the solid/water interface is minimized. On such a rough, low energy surface, water gains very little energy from adsorption to compensate for any enlargement of its surface. In this situation, spreading does not occur, water forms a spherical droplet, and the contact angle of the droplet depends almost entirely on the surface tension of the water [20]. Using this kind of surfaces is suggested for many applications such as anti-icing purposes.

1.2 Droplet Impact Dynamics

Droplets impact on a solid surface is an important factor in different technical applications such as plasma spraying, ink-jet printing, and liquid atomization [28-30]. When a droplet impacts on a solid surface, it may spread over the surface, recede or rebound from it and breaking into smaller drops called satellites. It should be noted that these different behaviors mainly depend on the droplet size, properties of the liquid/solid interface and also the impact velocity of the droplet [31]. To investigate the effect of the mentioned parameters, the following dimensionless groups are used;

$$\begin{cases} We = \frac{\rho u^2 D}{\sigma} \\ Re = \frac{\rho u D}{\mu} \\ Oh = \frac{\mu}{(\rho \sigma D)^{0.5}} \end{cases}$$ **Equation 1.5**

where ρ, μ and σ represent liquid density, viscosity, and surface tension, respectively. Droplet diameter is denoted by D and U is its impact velocity. *We, Re* and *Oh* denote the Weber, Reynolds, and Ohnesorge numbers, respectively. Weber number is used as a relative measure of the fluid inertial force to its surface tension. Reynolds number gives the ratio of fluid inertial to its viscous forces and finally Ohnesorge number gives the ratio of viscous forces to surface tension. It is important to mention that by knowing two of the above stated dimensionless

parameters, one can derive the third one i.e. there are only two independent dimensionless groups to describe the droplet impact dynamics on smooth surfaces.

Study of droplet impact began over a century ago with the work of Worthington [32, 33]. He formulated the bouncing and resting of droplets on a liquid pool in addition to different types of splashes by observing these behaviors with what was called high speed imaging at the time. About two decades ago Chandra *et al.* [34] studied the impact of a droplet on a solid surface using a flash photographic method. They provided a clear image of the droplet structure during the deformation process while impacting on a solid metallic surface. During the past decades a lot of work was performed in the field of droplet impact on a solid substrate most of them related to deriving the maximum spreading diameter of the droplet after impact. One of the first models based on energy balance was presented by Pasandideh-Fard *et al.* [35] which is valid for the cases when the droplet Weber number is high enough to reach the spreading phase. There are other methods proposed in literature which show a better agreement with experimental results [36, 37]. It should be noted that in addition to spreading if the droplet Weber number is high enough, splashing may occur during the spreading phase and satellite droplets will be produced [38]. It has been proven that not only the inertia of droplets but also the morphology of substrate is important in droplet splashing [38]. It is worth mentioning that all the above mentioned models [35-37] are valid for smooth surfaces, in other words the effect of surface texturing/roughness were not taken into account. Despite the vast usage of textured substrates in industrial applications, a few models have been developed to account for the effect of roughness on droplet impact. Lee *et al.* [39] proposed a model for determining the droplet spreading diameter impacting on hydrophobic textured surfaces. They showed that the width and height of the pillars are important factors in droplet spreading behavior.

In addition to droplet impact phenomenon, the study of droplet shedding and coalescence are also important due to their various scientific and industrial applications. It is believed that icing phenomenon on critical components such as aircraft wings and wind turbine blades is mostly driven by the effect of shear flow resulting in shedding and coalescence of droplets. In the following section droplet shedding and coalescence driven by shear flow will be discussed in detail.

1.3 Droplet Shedding and Coalescence Dynamics

There are various natural circumstances when droplet shedding and coalescence plays a vital role such as rain drop formation in clouds [40-42] and icing phenomena that occur on turbine blades, power lines and aircraft components [5, 43]. As an example, in in-flight icing condition, when rain droplets hit the aircraft wing, under the effect of air shear over the airfoil they may coalesce and form a larger droplet. Due to the airfoil surface properties and the air shear effect, the merged droplets may also create a runback flow in the form of narrow stream films (i.e. rivulet). At temperatures below the water freezing point, rain droplets and rivulets turn into ice. Ice accumulation on airfoil surface leads to the pressure drop increase around the airfoil. Consequently the aerodynamic characteristics of the airplane change significantly. For example the drag force increases and the lift force decreases [6] which may cause problems in aircraft control system and possible damages [5]. Details of shedding and coalescence under the effect of shear flow will be discussed in the following sections, as the preliminary stage of ice accumulation on industrial components.

Droplet Shedding

Sessile droplet movement under the effect of air shear flow is called shedding and occurs if the so-called shear flow overcomes the droplet adhesion to the substrate (see Figure 1.6). The droplet then moves along the surface [44].

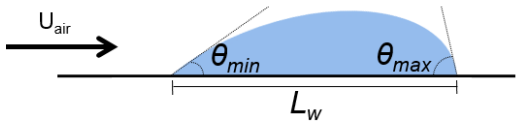

Figure 1.6 Schematic of the shedding phenomenon

The drag force created by the shear flow and the adhesion force of the droplet to the substrate can be described by the following correlations [44];

$$F_{drag} \propto \frac{1}{2}\rho u_{air}^2 S C_D \qquad \textbf{Equation 1.6}$$

$$F_{adh} \propto L_w \sigma (cos\,\theta_{min} - cos\,\theta_{max}) \qquad \textbf{Equation 1.7}$$

where, ρ and σ are the density and surface tension of the droplet, respectively. Air shear speed and the droplet wetting length are denoted by u_{air} and L_w, respectively (see Figure1.6). The area of the droplet facing air flow and the drag coefficient are S and C_D, respectively. Since droplet contact angle variations results in different drop shapes, both S and C_D are dependent on surface wettability. During the shedding process, droplet deformation occurs as a result of droplet contact angle variation upstream and downstream (i.e. θ_{min} and θ_{max}) of the flow. It should be noted that these angles are measured at and after the starting point of the droplet movement (incipient motion). Consequently, during the shedding process, droplet wetting length (L_w) on the substrates changes.

It should be noted that there exist only a few studies on the physics governing the shedding of droplets under the influence of shear flow. Milne and Amirfazli [44] performed wind tunnel

experiments to analyze droplet shedding phenomenon under the effect of air shear speeds as high as 20 m/s. They investigated the effect of surface wettability on dynamics of shedding based on droplet adhesion to the substrates.

Droplet Coalescence

Although droplet shedding is an important factor in icing phenomenon that occurs on wind turbines, power lines or aircrafts, in practice there are more than one droplet involved in icing conditions. As a result due to the presence of air shear flow droplets may coalesce with each other. Droplet coalescence is a phenomenon in which two droplets come together and form a larger one [45]. During the coalescence process the two droplets touch each other from their circumference. As a result a neck shape bridge is formed at the two drop interface (see Figure 1.7). The height of this bridge (h) grows with time up to the point that the two droplets merge completely and form a single droplet. The resulting droplet has a lower surface area which corresponds to surface energy minimization [45].

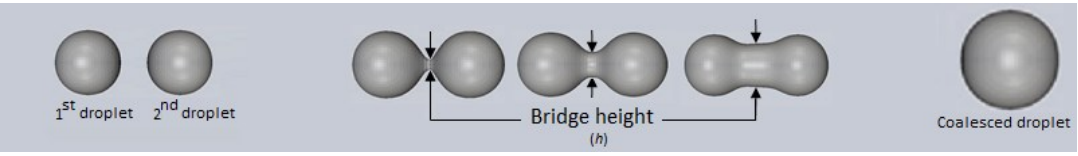

Figure 1.7 Schematic of the bridge height growth during coalescence process

The coalescence study of two highly viscous droplets that are not touching any surface was first investigated about 70 years a go by Frenkel [46]. He concluded that when two free droplets (not touching any surface) are touching each other the flow is initially in the viscous regime because the bridge height (shown in Figure 1.7) is significantly smaller than the viscous characteristic length. For droplets with low viscosity because the neck and consequently the

bridge radius starts to grow after merging, the flow regime changes from viscous to inertial. When the inertial flow regime becomes dominant, the droplets' merging is subjected to the competition between the inertia and the surface tension. As a result in this case an inviscid assumption is valid [30, 47, 48]. However, if the droplets have high viscosity, the coalescence phenomenon happens in a longer time. Coalescence of the two droplets in a viscous regime was done with direct numerical simulation in the work of Van de Vorst [49, 50].

The coalescence phenomenon of the droplets placed on a surface is different from the free droplets especially in the case of wettable substrates. The reason is that when the droplets wet the substrate the coalescence dynamics is mainly affected by the viscous stresses that the substrate imposes on the droplets [51]. In the work of Ristenpart *et al.* [51] it was also mentioned that the droplet geometry has an important influence on the coalescence rate. If the surface is partially wettable the coalescence dynamics tends to be similar to the free droplet case [40, 52, 53]. Various experimental and theoretical work have been reported on coalescence of the droplet on partially wettable surfaces [45, 54]. The evolution of the bridge height during droplet coalescence on partly wettable surfaces was covered in the work of Lee *et al.* [45]. They concluded that as the droplets used in their work were sufficiently small, the coalescence process corresponds to the viscosity dominant creeping flow. The authors also mentioned that coalescence process in their work was affected by both the viscous bulk stress and the viscous friction caused by the substrate. Accordingly their results deviated from the coalescence of highly viscous free drops described by Frenkel in [46].

In addition to the mentioned work dedicated to the physics of coalescence only, this phenomenon was also studied under the effect of different surface wettabilities. Numerical and experimental analyses of normal droplet impact on already rested sessile droplet on a

superhydrophobic surface was studied by Farhangi *et al*. [23]. They showed that due to the impact of the second drop on the first one, the resulting merged droplet bounces on the superhydrophobic surface. Graham *et al*. [55] investigated similar work on surfaces with various wettabilities ranging from hydrophilic to super hydrophobic both numerically and experimentally.

Despite the above mentioned studies, the effect of shear driven shedding and coalescence of droplets especially with high air shear speeds that corresponds to the flight situation has not yet been reported. As mentioned before, one of the applications of the concurrent droplet shedding and coalescence is in aerospace industry especially for in-flight icing condition. To prevent damages that icing causes during flight and to increase the aircraft safety, being able to decrease or prevent ice accretion on airfoil surface is an important issue in aerospace industry. A deep analysis of the simultaneous droplet shedding and coalescence under the effect of high shear flow can be one of the key points to this goal.

1.4 Rivulet Dynamics

A narrow stream of liquid moving along a solid substrate is called a rivulet. Exceeding a certain amount of flow, a rivulet may start meandering resulting in instability on the interface [56]. A good example of a rivulet is the water stream on a window during a rainy day (Figure 1.8). Rivulet dynamics is involved in different scientific and industrial applications such as the flow of surface active materials in chemistry [57], and rain flow on structural systems such as power lines, wind turbines and aircrafts [6].

Figure 1.8 Rivulet on a window pane

Rivulets may have different patterns based on their flow rate [58]. A rivulet starts with a sequence of droplets that merge into a linear straight narrow film. At higher flow rates a rivulet starts meandering with instabilities at its interface with air [56]. Increase in flow rates leads to the formation of oscillating rivulets [56]. Based on the axial velocity, rivulets are divided into two categories. One is the static rivulet which does not have the axial velocity component [59]. The other is the dynamic rivulet that has the axial velocity component [60]. There are varieties of situations that can affect rivulet flow. For example, the velocity of the rivulet, the substrate inclination angle, the temperature and the morphology of the surface are significant factors that should be taken into consideration.

Mathematical description of rivulet dynamics is complicated due to the existence of free boundary interfaces which must be determined as a part of the solution to the governing equations. The problem becomes even harder if the film unit depth goes to zero, because linearized equations will not be sufficient to study the phenomenon. Thus, nonlinear film disturbances must be taken into consideration. Lubrication theory or long-wave-theory is one of the methods to study thin film flow on a solid surface. In this method, the governing equations and boundary conditions are simplified to a system that usually contains a single nonlinear partial differential equation that is formulated in terms of the local film thickness [61] . Other

unknowns such as fluid temperature and velocity are determined by functional solution of the initial differential equation. In this case the free boundary complication can be eliminated from the system [62]. Marshall and Ettema [63] used lubrication approximation in their experiments with low Reynolds number to investigate the effect of gravity and shear flow on rivulets. They showed that for low speed shear flows (less than 5 m/s) shear driven flow and gravity effects have nearly the same influence on rivulets behavior. However, at high sheer speeds of 10 m/s there is a large difference between the flows driven by wind shear and the flow of rivulets under the effect of gravity. In addition in the latter case, they reported that the effect of microgravity and terrestrial gravity is also considerably different for the case of rivulet flow.

As mentioned before, surface morphology is one of the factors that should be taken into consideration while studying rivulets behavior. Gajewski [64, 65] conducted experiments with rivulets on three different surfaces: aluminum, copper and brass while heating [64] and cooling [65] these surfaces. It was shown that lowering the temperature improves the hydrophilic behavior of the metal surface, thus, the rivulet width increases. In addition when the number of electrons on the last metal shell is higher, the metal shows more hydrophilic properties [65]. This is the reason that the worst wetting property is for copper. The rivulet is the narrowest on this plate and the contact angle is the highest. In contrast, among these metals the best wetted surface is aluminum. It has the widest rivulet flow and the contact angle is the lowest on this plate [65].

Simulation of thin film flow patterns, flowing down inclined and horizontal planes was performed by Diez *et al*. [57, 66]. Their model has the capability to show the effect of capillary force and fluid-solid interactions for analyzing the rivulets wave lengths. Daerr *et al*. [67] found that the fluid inertia is the main cause of the meandering behavior while doing theoretical work on rivulets stability. Saber *et al*. [68] obtained analytical results for rivulet thickness, wetting rate

at break up by using the idea that total energy of the stable rivulet would be minimized after the break up process. Their analysis was performed by assuming that the fluid is flowing down or climbing on a vertical or inclined surface while the surface is subjected to the interfacial shear flow.

It should be mentioned that up to now a complete understanding of rivulet dynamics especially under the effect of different surface wettabilities has not yet been achieved. Being able to predict the rivulet behavior under the effect of shear flow and different surface wettabilities is of utmost importance for understanding the underlying physics of rivulet dynamics under practical conditions, i.e. in-flight icing.

1.5 Icing Phenomenon

Generally there are two types of ice generation on aerodynamic components; Glaze and Rime [69]. Glaze or clear icing is transparent and has a smooth surface. Its formation is due to the impact and spreading of supercooled droplets under the influence of cold air flow along the surface. Rime ice is blurred and brittle and forms immediately after the impact of the droplet. Glaze ice can runback along the airfoil and covers more area, and also it is hard to be seen from the inside of the aircraft. The last two characteristics make the Glaze ice more harmful that the Rime [69].

Droplet size, air temperature and liquid water content are factors that are important in icing type. For example Rime ice is associated with small droplets, low temperature and low liquid water content. These three factors are all significant for Glaze icing [69]. Glaze and Rime ice can be observed in Figure 1.9 which shows the leading edge of the left wing of a Twin Otter aircraft in NASA Glenn Research Center.

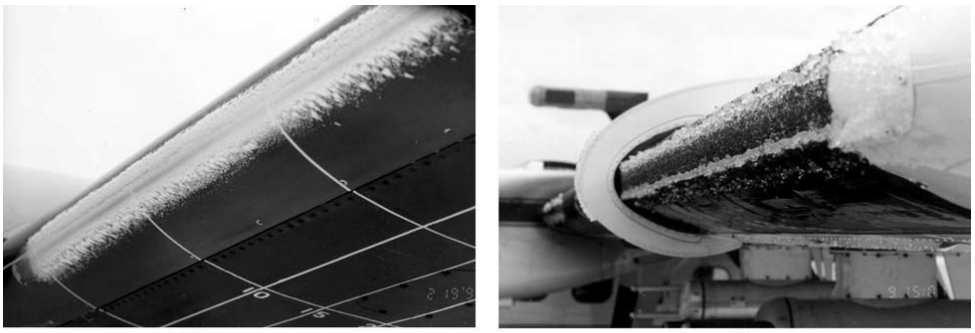

a) Rime ice b) Glaze ice

Figure 1.9 a) Light rime ice and b) Sever Glaze ice [69]

One of the proposed methods for reducing the amount of accumulated ice is using superhydrophobic coatings [70]. Icing of supercooled water on superhydrophobic surfaces is a complex phenomenon that depends on surface morphology, as well as ice adhesion, hydrodynamic conditions, and structure of the water film on the surface.

Antonini *et al*. [71] showed that using a superhydrophobic coating on airfoil can reduce the amount of accreted ice due to low water adhesion on these surfaces. Hence, the amount of power required to remove ice from a superhydrophobic surface is significantly reduced in comparison with an uncoated hydrophilic surface. Boinovich *et al.* [72] studied the nucleation kinetics of supercooled water droplets on surfaces with various wettabilities. They showed that at subzero temperatures and saturated water vapor atmosphere, superhydrophobic surfaces show a significant delay in ice formation in comparison with the hydrophilic and even hydrophobic surfaces. Cao *et al.* [73], used nanoparticle-polymer composites to show the anti-icing capability of superhydrophobic surfaces. In their work one side of the aluminum plate was compared to its other side that was coated with nearly 50 nm organosilane modified silica particles. The authors showed that the coated surfaces were able to prevent the formation of ice upon the effect of supercooled water.

It was discovered by Cao *et al*. [73] that in addition to hydrophobicity of the surface, the size of the particles exposed on the surface is also effective in anti-icing capability. Ice was not formed on the samples prepared with 20 and 50 nm particles. However, by enlarging the particles diameter to greater than 50 nm, icing possibility increased to distinctive amounts. The reason is that when the samples are prepared with less than 50 nm particles, according to Cassie-Baxter equation less than 15% of the surface area was in direct contact with water. As a result, ice is created through a heterogeneous nucleation process at the contact between water and the particles exposed on the surfaces at the time that supercooled water hit such surfaces. Hence in addition to the superhydrophobicity of the substrate, the size of the particles exposed to the surface is also an important parameter that determines the kinetics of the ice nucleation process [73].

1.6 Objectives

This study is dedicated to understanding the onset of droplet accumulation on surfaces of various wettabilities ranging from hydrophilic to superhydrophobic, by analyzing the shedding and coalescence dynamics of one and two sessile droplets under the effect of various air shear flows. The study is further expanded to analyze rivulet formation and evolution driven by the effect of air shear flow. The main application of the work can be found in industries with the purpose of ice reduction on critical components.

The objectives are summarized below;

1. *Experimental study on droplet shedding and coalescence;* Shedding and coalescence behavior of single and two sessile droplets placed on hydrophilic and superhydrophobic substrates are investigated under the influence of air speed from 5 to 90 m/s at room temperature.

2. *Experimental study on droplet shedding and solidification;* Concurrent droplet shedding and solidification is investigated on hydrophilic and superhydrophobic substrates under the influence of air shear flow from 5 to 90 m/s when the substrate temperatures is as low as -5 ^{o}C.

3. *Experimental and numerical study on the formation and dynamics of rivulet;* Rivulet dynamics and evolution is investigated on surfaces with various wettabilities ranging from hydrophilic to superhydrophobic using Smoothed Particle Hydrodynamic (SPH) method.

1.7 Thesis Layout

This thesis is organized in a paper-based format to present fundamental study on droplet shedding and coalescence on surfaces with various wettabilities under the effect of shear flows as high as 90 m/s. This study can be considered as the onset of rivulet formation and propagation which then can result in ice formation on surfaces if the temperature is below the freezing point. This work consists of seven chapters with the outlines described below.

Chapter 1 is dedicated to an introduction on the most important parameters affecting droplet dynamics and icing phenomenon. The physics of droplet shedding, coalescence and rivulet formation is provided as a building block for the ice formation on critical components such as aircraft wings, nacelle, and wind turbine blades together with a brief literature to describe the scientific advances in this area.

In chapter 2 a fundamental experimental study is described on shear driven shedding phenomenon of a single sessile droplet on hydrophilic and superhydrophobic substrates. The effect of surface wettability on dynamics of droplet shedding is demonstrated based on the formation of rivulets and droplet detachment from the hydrophilic and superhydrophobic substrates, respectively. In addition droplet shedding mechanism under the effect of air flows as

high as 90 m/s is compared with the same phenomenon under the effect of lower air speeds such as 5 m/s.

In chapter 3 a detailed study of droplet coalescence on an aluminum (hydrophilic) substrate under the effect of various air speeds ranging from 5 to 90 m/s is provided which can serve as a building block for the formation of rivulet. High speed imaging is used to characterize the differences in droplet coalescence, deformation and propagation mechanisms under the effect of low and high shear flows which leads to understanding the onset of rivulet formation.

In chapter 4 details of droplet coalescence under the influence of air speeds as high as 90 m/s on a superhydrophobic substrate are provided. Droplets deformation and detachment during coalescence is analyzed and compared with the results of single droplet shedding on the same substrate. The experimental results are then compared with the results of numerical simulation based on Volume of Fluid (VOF) method to give a better understanding of the coalescence phenomenon by analyzing the aerodynamic forces, velocity vectors and stream lines on the droplets.

In Chapter 5 a fundamental study on concurrent droplet shedding and solidification is carried out under the effect of shear flows as high as 90 m/s. The difference between the primary stages of ice formation on substrates with temperatures as low as -5 ^{o}C and different wettabilities are analyzed based on the mechanism of droplet shedding under the effect of low and high air speeds.

Chapter 6 is dedicated to the analysis of rivulet formation and evolution under the effect of air flows as high as 20 m/s on different surface wettabilities ranging from hydrophilic to superhydrophobic. The results taken from the controlled and steady state experiments inside a wind tunnel were compared and validated with those achieved by performing simulation based

on Smoothed Particle hydrodynamics (SPH) method to analyze the formation and evolution of rivulet. Variation of rivulet thickness and its wavy patterns along the flow were analyzed and compared based on the air shear flow and the surface wettability.

Finally in Chapter 7 summary of the findings and recommendations for future research is provided. For easier tracking, the thesis layout is given in the below flowchart.

Thesis layout

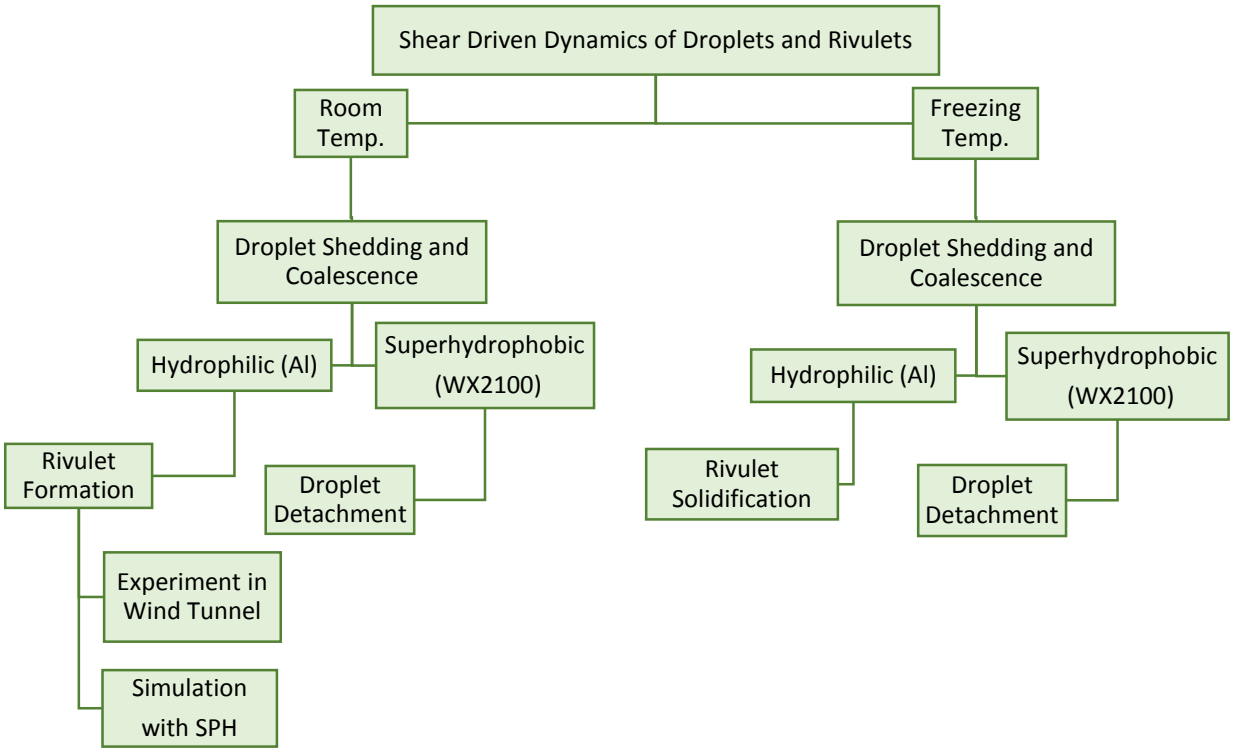

Chapter 2

Shear Driven Droplet Shedding on Surfaces with Various Wettabilities

Abstract

Experimental study is performed to analyze the shedding behavior of droplets with different shear flow speeds typical of those in flight conditions. Droplet shedding phenomenon has significant effect on ice accumulation on critical components such as airfoils and nacelles. In order to mimic this scenario experimental setup is designed to generate shear flow as high as 90m/s. The high shear effect is combined to the surface wettability impact by using hydrophilic and superhydrophobic surfaces. It is shown that the wetting length of the droplet on hydrophilic surface increases by shear speed while on the superhydrophobic surface a drastic reduction on wetting length is detected. Furthermore, it is observed that the droplet is detached from the superhydrophobic surface with moderate air speeds.

2.1 Introduction

Exposing shear flow to a sessile droplet which is placed on a substrate makes the droplet move. This movement is called shedding and happens when the shear flow overcomes the droplet adhesion to the substrate. After the start of the droplet shedding, which is called the incipient motion, the droplet moves downstream along the surface [44]. Shear driven droplet shedding has various industrial applications such as in icing phenomenon that occurs on airplane airfoils, wind turbine blades and power lines [43]. The knowledge can also be used in enhancing the performance of oil recovery systems [75]. In the following study, different air shear speeds ranging from 5 m/s to 90 m/s are used as the driving force to move the water droplet. Therefore, the outcome of the work can be more applicable for ice accumulations on airfoils, wind turbines and power lines. The reason is that in the mentioned applications, the droplets impact on the surfaces and later on start to move along the surfaces due to the air shear flow. Generally, on hydrophilic surfaces, the runback flow of the droplets results in the formation of narrow streams of liquid known as rivulets [76]. Based on the surface morphology and shear driven forces rivulet can propagate on the surface and covers more area. When the ambient temperature is lower than the water freezing temperature, droplets and rivulets will be frozen and lead to significant damages on various components. For example, in the case of airplane, ice accumulation significantly reduces the aerodynamic efficiency of the airplane by increasing drag and decreasing lift forces [6]. There are limited insights into fundamentals of air shear driven drop shedding in the literature especially on superhydrophobic surfaces. Although in the work of Milne and Amirfazli [44], droplet incipient motion due to lower shear flow speed (below 30 m/s) was studied on different surface wettabilities, but the investigation at higher speed, close to those occur in aerospace applications is missing. In the following experimental study, different range

of air speeds are used on both hydrophilic and superhydrophobic surfaces. Study of the drop behavior on superhydrophobic surface is an active research area due to the high water repellency characteristics of these surfaces. As mentioned before, shedding occurs when the drag force overcomes the adhesion forces. It is known that both drag and adhesion depend on, contact angle of the surface (wettability), the size and shape of the droplet. Since the last two parameters are also a function of contact angle, the surface wettability is highly important in droplet shedding process [77]. As a result, except the shear flow and surface material, all other parameters like the droplet shape, size, temperature and humidity is kept constant in the experimental procedure.

2.2 Experimental Setup

The experimental setup enables recording the behavior of a sessile droplet while facing air shear flow. The shedding time is of the order of micro seconds; to capture the process precisely, a Photron SA1.1 high speed camera (Photron, California USA) operating at 5400 frames/s with an UltraZoom 6000 lens (Navitar, New York USA) was used throughout the experiments. In order to illuminate the droplet shedding progression, an LED light (Schott, California USA) was used. In these experiments backlight method was used for capturing the images. To be able to see the droplet deformation completely, side view and top view images were taken from the shedding process. The air shear speed varies between 5m/s and 90m/s. Experiments were carried out on two rectangular plates with a size of $150\times75\times2$ mm^3. The first plate is a polished aluminum which acts as a hydrophilic substrate with a contact angle of 75^o. The second surface acts as a superhydrophobic with a contact angle of 155^o, that surface is a polished aluminum plate coated with WX2100 spray (Cytonix, Maryland USA). A high pressure tank was applied to create the shear flow. Air was introduced on the substrate from the tank by using a tube with the inlet diameter of 10 mm. The air velocity was controlled with a high pressure valve and the tube

was attached to the substrate leading edge. Distilled water droplet was deposited on the surface from a sterilized syringe at about 10 mm away from the beginning of the substrate. The reason to choose 10 mm away from the substrate leading edge, is that air stream is smooth and without any vortices at and after this location. The droplet diameter for each test was around 2.1 mm which was subjected to the air flow at speed of approximately 5, 18, 34, and 90 m/s. This is the air velocity that was measured with a pitot tube at the droplet position. It should be noted that each test was repeated fifteen times to reach an acceptable degree of accuracy. The reported results are the ensemble average of these fifteen experiments for each case. It should also be noted that all the experiments are performed at room temperature (22 °C).

Table 2.1 Test Matrix

Surface Material	Aluminum		WX2100	
Contact Angle (°)	75±1		155±1	
Contact Angle Hysteresis(°)	18±2		8±2	
Shear Speed (m/s)	5±2	18±2	34±2	90±2

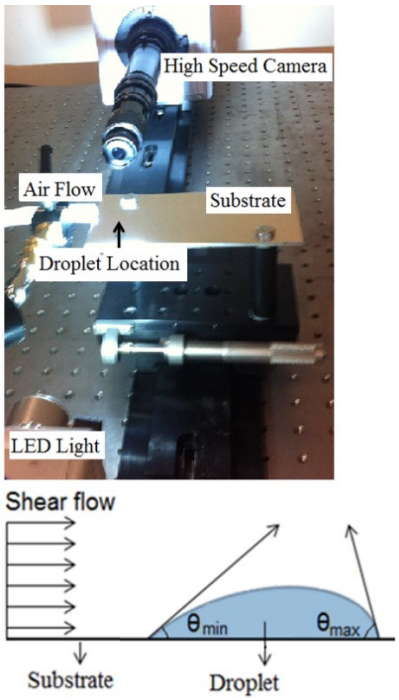

Figure 2.1 Experimental setup and schematic of the shear driven droplet shedding

Table 2.1 shows the test matrix in addition to the surface characteristics. All the measurements in this work were post-processed with ImageJ software [78]. The details of the post processing methodology can be found in the work of Abramo *et al.* [78]. The experimental setup and schematic of the droplet shedding under the effect of air shear are shown in Figure 2.1.

2.3 Results and Discussions

Considering the droplet behavior during shedding, one of the interesting parameters to be measured is the wetting length of the droplet on the substrate. Wetting length (L_w) variation depends on substrate contact angle, droplet size and the air shear speed. Since in this study we have mainly focused on the effect of surface wettability and the air shear speed, the size of the droplets were kept constant in all the tests (2.1 mm). To observe the effect of surface wettability and shear speed separately, one of these parameters was kept constant during one test and the other one was being changed. The top view and side view images that were recorded at different stages of the droplet movement are shown in Figure 2.2 and 2.3.

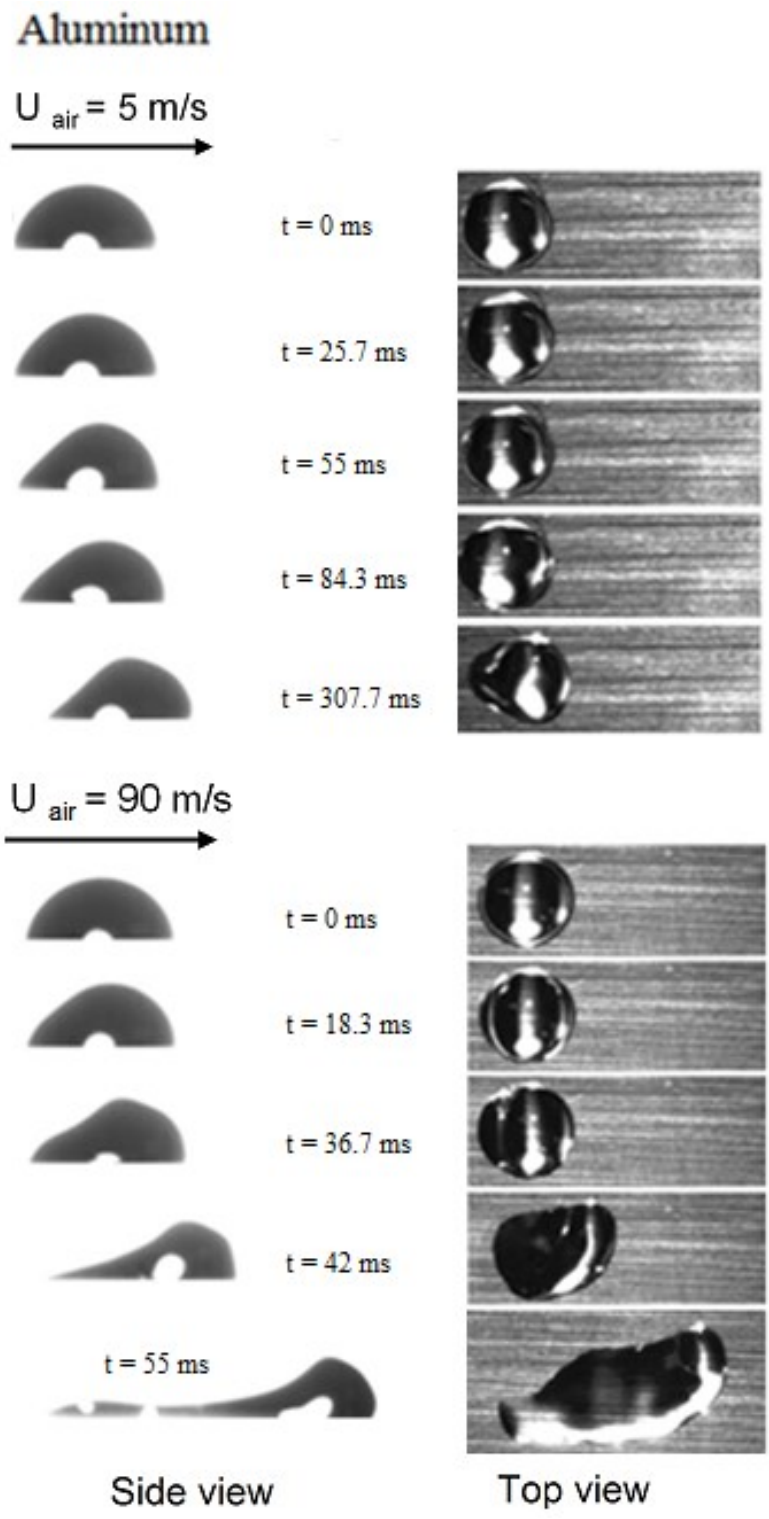

Figure 2.2 Sequence images of droplet shedding and deformation on the aluminum substrate; Rivulet formation can be seen in the last image of the sequence

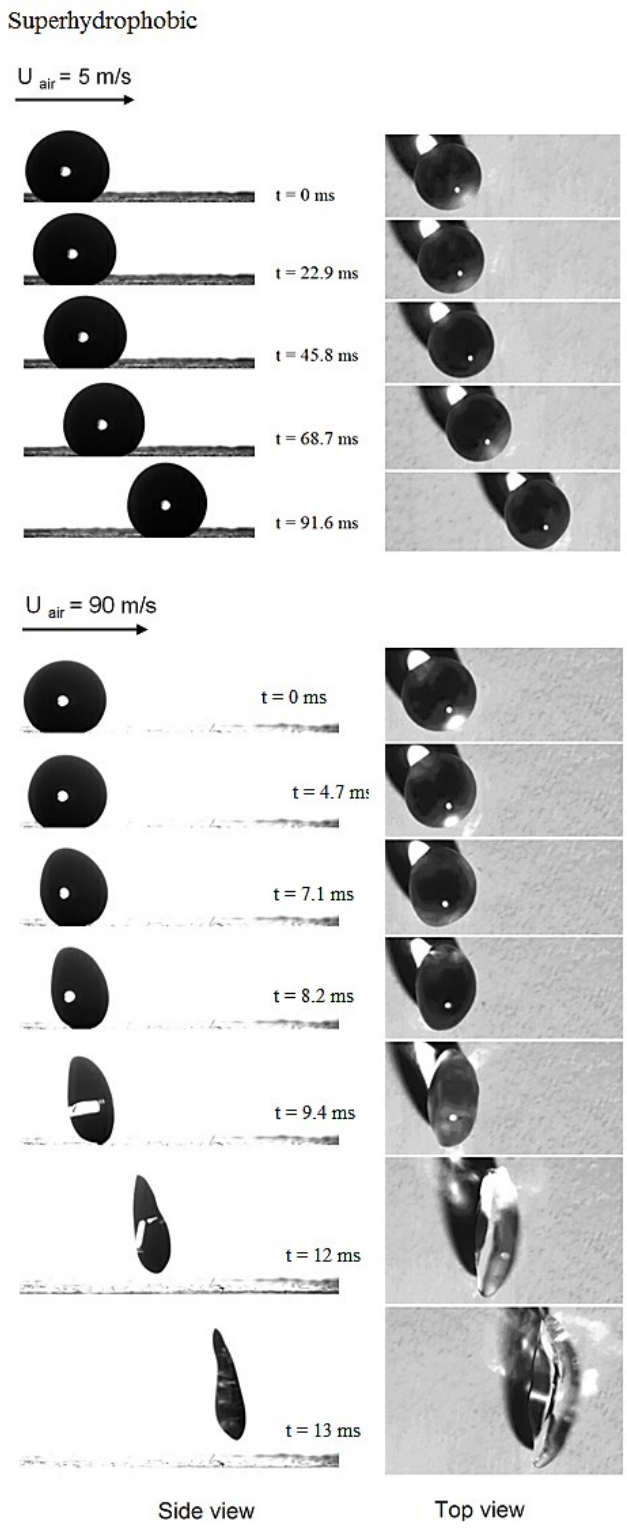

Figure 2.3 Sequence images of droplet shedding and deformation on the superhydrophobic substrate

In the mentioned figures, the image sequences are associated to the lowest (5 m/s) and highest (90 m/s) air speeds. As can be seen in Figure 2.2 when the air velocity is low the droplet only oscillates on the substrate with a slow movement. However, for the case of high speed shear flow, the deformation of the droplet is in a way that a rivulet forms on the aluminum surface. In contrast, on superhydrophobic surface (SHS) in Figure 2.3, the droplet only rolls over the surface for low shear speed of 5 m/s. For high shear flow (90 m/s) the droplet deforms to an oval shape. After about 10 ms the droplet detaches from the surface. As the droplet wetting length on SHS is less than hydrophilic surface due to the lower adhesion of the superhydrophobic material, the amount of ice accretion on superhydrophobic surfaces is less than hydrophilic surface. Hence, superhydrophobic surfaces can be an ideal material for anti-icing purposes.

The results of the experimental tests are reported in two different sets of graphs for each substrate. The first sets that are plotted in Figures 2.4 and 2.5 describe the variation of wetting length versus time for four different air shear speeds on aluminum and SHS, respectively. As can be seen in the mentioned figures the droplet behavior on aluminum surface is completely opposite to its behavior on SHS. On the aluminum surface by increasing the velocity, the wetting length increases and this cause the formation of a thin-narrow film (rivulet) on the substrate. With low air speed of about 5 m/s there is no significant change in droplet wetting length. With this low shear speed, the droplet only oscillates on the surface and does not spread on it. Increasing the air flow speed to 18 m/s, shows that after approximately 65 ms the droplet starts to deform and spread on the surface. Hence 15% of increase in the wetting length can be seen and rivulet forms after about 80 ms. Deformation due to the air shear flow occurs faster with higher shears and droplet spreads more on the surface; therefore, its wetting length increases. Figure 2.4 clearly shows that with the shear speed of 34 m/s, the deformation process starts at about 55 ms

and rivulet forms after about 70 ms. The deformation time decreases to 35 ms when the shear speed is 90 m/s and rivulet forms after about 45 ms. It is important to mention that wetting length increases after rivulet formation.

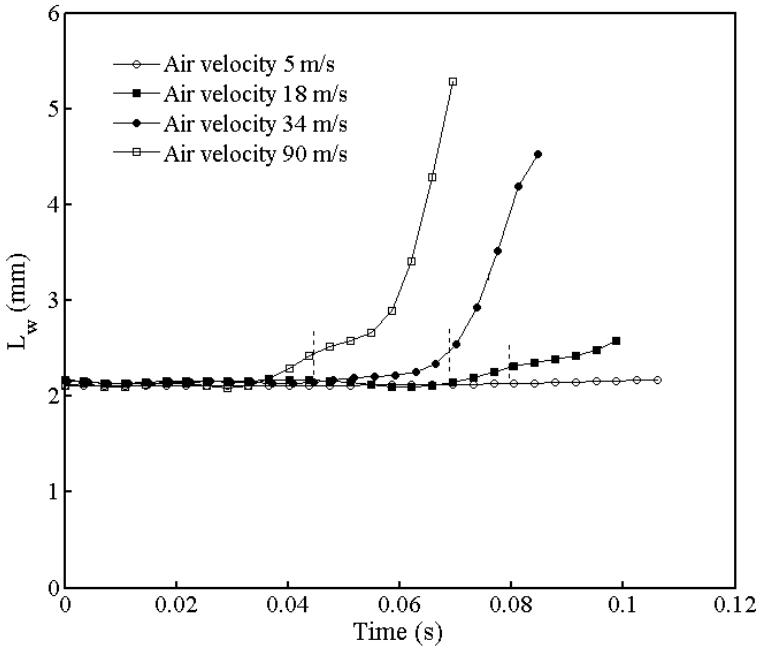

Figure 2.4 Wetting length vs. time on the aluminum substrate; dash lines show the start of rivulet formation

Figure 2.5 shows the wetting length variation of the droplet on SHS versus time. When the air flow is 5 m/s the droplet rolls over the surface and after about 55 ms the droplet wetting length slightly decreases. Within 100 ms of the recording time droplet rolls over the surface and exits the camera's field of view. It should be noted that there is no detachment from the substrate with this air velocity. As expected, the decrease in the wetting length occurs faster by increasing the shear speed. For instance, for 18 m/s of air flow, the droplet jumps off the surface after about 40 ms. Therefore, the wetting length cannot be defined beyond this time. It should be noted that at 90 m/s air speed, 1.1 mm decrease in the wetting length occurs in less than 10 ms and droplet separation occurs afterwards (see Figure 2.3).

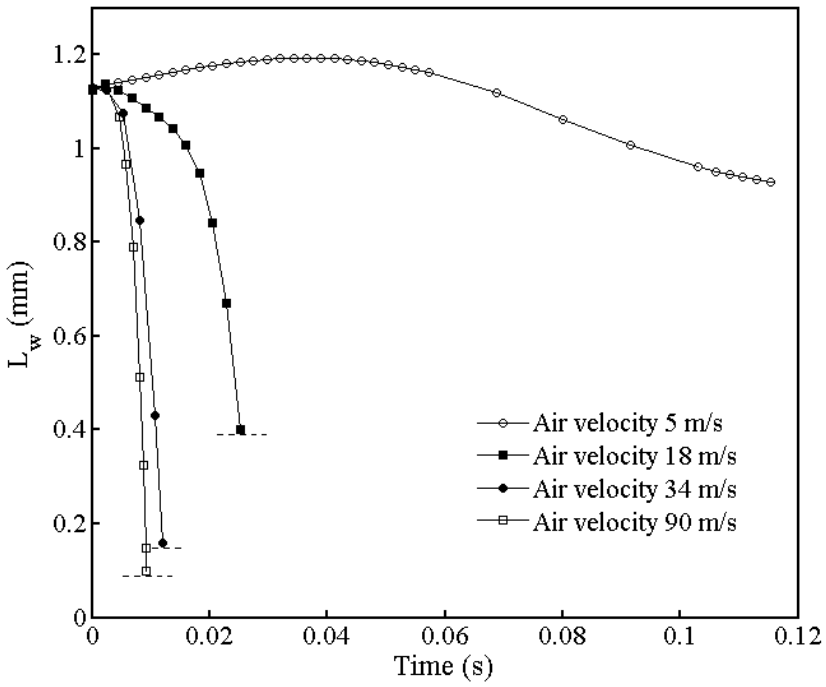

Figure 2.5 Wetting length vs. time on the superhydrophobic substrate; dash lines show the separation point of the droplet from the substrate

As indicated earlier, the droplet starts to move (shed) while the drag force caused by the airflow overcomes the adhesion force between the droplet and the substrate. These forces can be calculated from the following equations [44];

$$F_{drag} \propto \frac{1}{2}\rho u_{air}^2 S C_D \qquad \textbf{Equation 2.1}$$

$$F_{adh} \propto L_w \sigma(cos\,\theta_{min} - cos\,\theta_{max}) \qquad \textbf{Equation 2.2}$$

where, ρ and σ are the density and surface tension of the droplet, respectively. The air speed is u_{air} and the wetting length of the droplet is L_w (see Figure 2.1). The area of the droplet facing air flow is S and C_D is its drag coefficient. As variation of contact angle results in different drop shapes, both S and C_D are dependent on this parameter. When shedding occurs, the droplet starts to deform. This deformation arises from the variation of its contact angles upstream and downstream (θ_{min} and θ_{max}), which result in the variation of L_w. These contact angle values are measured at and after the starting point of the drop movement (incipient motion). According to

Equation 2.2, the value of $(cos\,\theta_{min} - cos\,\theta_{max})$ is an indication of the amount of the adhesion force. The second sets of graphs describe the variation of $(cos\,\theta_{min} - cos\,\theta_{max})$ versus time.

In Figure 2.6 variations of $(cos\,\theta_{min} - cos\,\theta_{max})$ versus time on the aluminum substrate can be seen. On this surface, increasing air speed causes droplet deformation in a way that $(cos\,\theta_{min} - cos\,\theta_{max})$ increases with time. As higher shear flow enhances the droplet deformation, the slope of the diagrams in Figure 2.6 increases from 5 to 90 m/s of air speed. The increase in the amount of $(cos\,\theta_{min} - cos\,\theta_{max})$, results in an increase in the adhesion force of the droplet. Therefore, the droplet stays on the surface, spreads over it due to shear effect and finally rivulet forms.

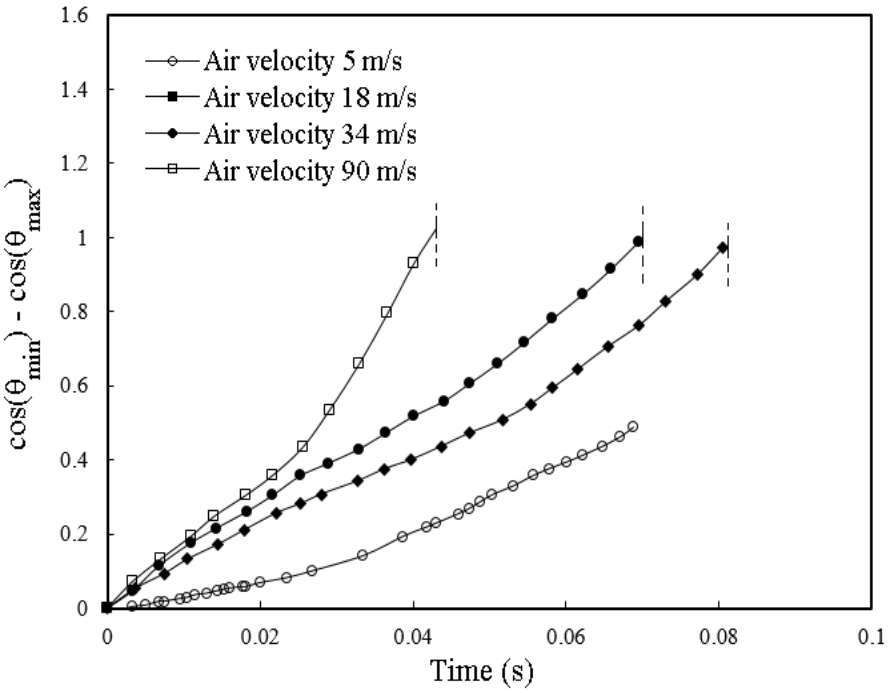

Figure 2.6 $(cos\,\theta_{min} - cos\,\theta_{max})$vs. time on the aluminum substrate; dash lines show the start of rivulet formation

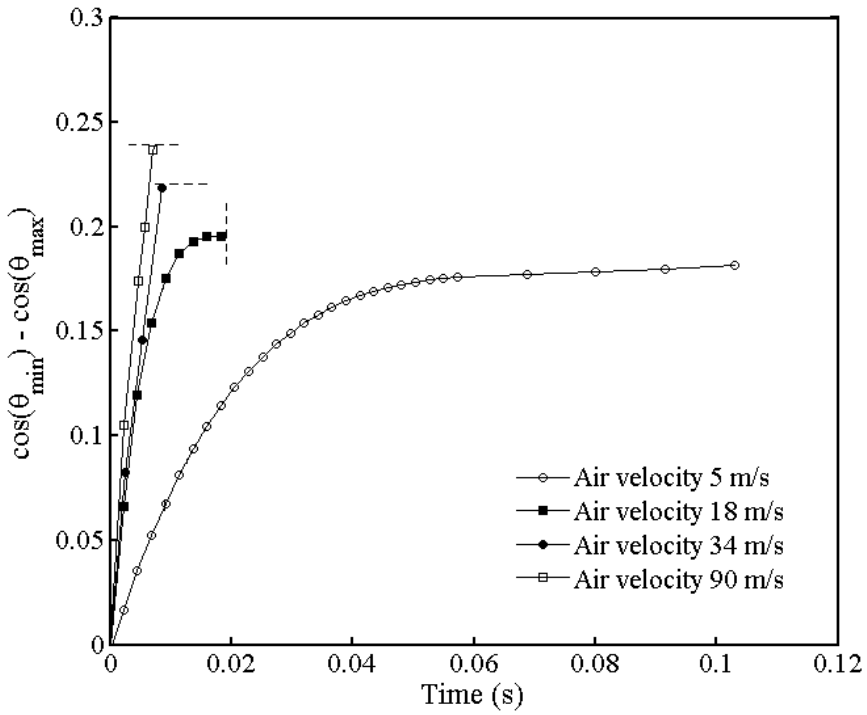

Figure 2.7 ($cos\,\theta_{min} - cos\,\theta_{max}$)vs. time on the superhydrophobic substrate; dash lines show the deformation point of the droplet

Variations of ($cos\,\theta_{min} - cos\,\theta_{max}$) versus time on the superhydrophobic substrate is plotted in Figure 2.7. As shown in the diagram, right after setting the airflow ($t = 0$ ms) the ($cos\,\theta_{min} - cos\,\theta_{max}$) value starts to increase. Larger values of ($cos\,\theta_{min} - cos\,\theta_{max}$) together with larger amount of L_w on aluminum substrate in comparison with these values on SHS, confirms the higher value of F_{adh} on the hydrophilic surfaces. It is important to mention that on SHS the droplet deforms before getting detached from the surface (as shown in Figure 2.3 when the air velocity is 90 m/s). The droplet deformation is in a way that it's wetting length decreases and the droplet gets an oval shape before detachment. The dash lines in Figure 2.7 display the starting point of the mentioned deformation (turning to an oval shape). Apparently, higher shear flow enhances the deformation process and makes the droplet to detach from the substrate faster.

Due to the low adhesion force of the droplet on the superhydrophobic surface the droplet rolls over the surface, this phenomenon is known as self-cleaning characteristic of these surfaces [20]. As mentioned above, shear effect enhances the drop shedding process and consequently its self-cleaning phenomenon. If the shear speed is high enough, the droplet detaches from the superhydrophobic surface. The period during which, the droplet detaches from the SHS, is called the detachment time. Being able to decrease or increase the droplet detachment time from the SHS has different industrial applications. For example decreasing the rain droplets detachment time, decreases ice accretion on airfoils. On the contrary, increasing the detachment time of foliar fertilizers on superhydrophobic leafs enhances the fertilizer's adsorption ratio.

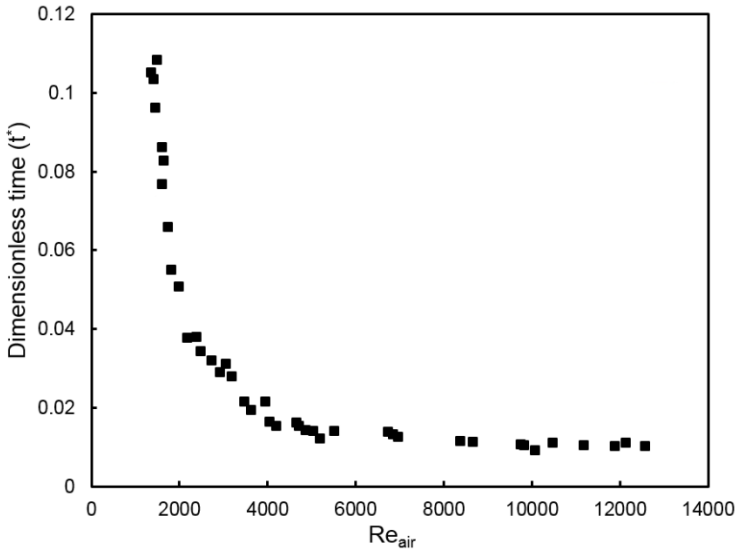

Figure 2.8 Dimensionless detachment time vs. Reynolds number on the superhydrophobic substrate

The detachment time of the droplet on SHS versus the air speed is shown in Figure 2.8. To draw the figure both detachment time and air velocity are nondimensionalized. The dimensionless time is chosen as follows;

$$t^* = \frac{t\mu_{air}}{2\rho_{air}\pi R_{eff} Z} \qquad \textbf{Equation 2.3}$$

where t is the detachment time, ρ_{air} and μ_{air} are density and viscosity of the air, respectively. R_{eff} and Z are the effective radius and height of the droplet respectively that are shown in Figure 2.9. The value of R_{eff} was calculated from Equation 2.4;

$$R_{eff} = R_o \left[\frac{4}{3} \times \frac{1}{\frac{2-\cos^3\theta}{3}+\cos\theta}\right]^{1/3} \quad \textbf{Equation 2.4}$$

where R_o is the initial radius and θ is the static contact angle of the droplet on the superhydrophobic surface. Air shear speed was nondimensionalized using the Reynolds number given by Equation 2.5.

$$Re = \frac{2\rho_{air} u_{air} R_{eff}}{\mu_{air}} \quad \textbf{Equation 2.5}$$

where u_{air} is the air shear velocity.

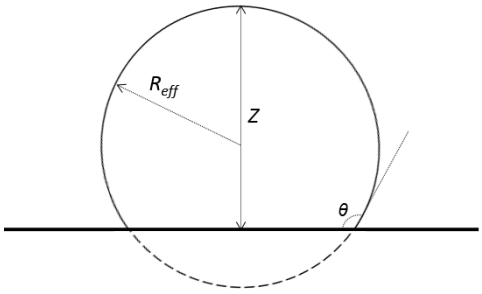

Figure 2.9 Schematic of R_{eff} and Z on a droplet placed on the superhydrophobic substrate

As it is shown in Figure 2.8, the experimental data was plotted by doing a dimension analysis. As it is clear from the figure, increasing the Reynolds number causes decrease in the detachment time of the droplet from the superhydrophobic surface. In other words, droplet detaches from the superhydrophobic surface faster by increasing the Reynolds number.

2.4 Summary and Conclusions

The shear driven shedding behavior of single droplet with high speed was investigated on hydrophilic and superhydrophobic surfaces. It was presumed that high enough shear flow causes the droplet to form rivulets while moving on hydrophilic surface. In contrast on superhydrophobic surfaces high shear speed causes the droplet to deform to an oval shape and subsequently easily detaches from the surface. It was also shown that the contact time of the droplet on the superhydrophobic substrate decreases by increasing the Reynolds number. The low adhesion of droplet to the superhydrophobic surface makes this kind of surface an ideal choice for anti-icing purposes as the amount of ice accretion is low in comparison with hydrophilic surfaces. This study can be further expanded for lower temperature to investigate the icing phenomena. Supplementary analysis can be done on droplet size effect in addition to numerical simulation of the shedding phenomenon.

Chapter 3

Shear Driven Droplet Coalescence and Rivulet Formation

"Reprinted from Journal of Mechanical Engineering Science paper JMES-14-0714.R1[79]."

Abstract

Icing on aerodynamic surfaces occur due to the accumulation of rain droplets when surrounding temperature is below the freezing temperature. It is well known that icing phenomenon alters the aircraft aerodynamics forces and may cause serious damages. Therefore, studying water droplet behavior i.e. shedding and coalescence serves as the primary step which can lead to understanding the fundamental physics of airplane icing phenomena. Hence, in this study an experimental approach is used to investigate the shear driven droplet shedding and coalescence on a hydrophilic substrate which can serve as the building block for the formation of rivulets.

3.1 Introduction

After rain droplets impact on aircraft's wings, the accumulated droplets start a run backflow on the airfoils. Under the effect of air shear flow, narrow streams of water known as rivulet form on the airfoils' surface. At temperatures lower than the water freezing point, droplets and rivulets turn into ice which may lead to significant damages on different components. For instance, the aerodynamic performance of the aircraft is dramatically affected by increasing drag and

decreasing lift forces [6]. Hence, understanding the complex mechanism of aircraft icing and consequently being able to suppress ice formation during flight is crucial in aerospace industry.

Sessile droplet movement under the effect of air shear flow is called shedding and occurs if the drag force on the droplet induced by shear flow overcomes the droplet adhesion force to the substrate. The droplet then moves along the surface [44]. Practically there is more than one droplet on aerodynamic surfaces; therefore imposing shear flow to the droplets may cause droplet coalescence in addition to the shedding phenomenon. Coalescence or sintering is a phenomena in which two droplets come together and form a larger one [45]. There are many industrial applications that benefit from the detailed knowledge of droplet shedding and coalescence such as various coating processes and ink-jet printing [30]. In addition to the industrial applications, there are many natural situations that droplets coalescence involve in such as rain drop formation in clouds [40-42] and icing phenomenon that occurs on turbine blades, power lines and aircraft components [43]. The outcome of the current study, however, can be more applicable to the latter cases.

There are variety of parameters that are important in analyzing shear driven droplet shedding and coalescence. Some of the most important factors are the shear speed [44, 74], morphology of the surface on which the droplets are moving [23, 52, 54, 55], droplet properties such as viscosity, surface tension, size and geometry [46, 51], and finally the substrate and the ambient temperature [71, 72, 80, 81]. It is important to mention that advances in theoretical and numerical approaches made it easier for researchers to understand the hydrodynamics of droplet coalescence [47, 82]. However, as the incipient of coalescence phenomenon occurs very fast, experimental approach for analyzing its preliminary stages are few in the literature [82].

Despite the above mentioned studies, the effect of shear driven coalescence of two droplets especially with high air shear speeds that can correspond to flight condition has not yet been reported. As mentioned before, being able to decrease or prevent ice accretion on an airfoil is an important issue in aerospace industry. A deep analysis of the simultaneous droplet shedding and coalescence under the effect of high shear flow can be one of the key points to this goal. In this study, the effect of concurrent shedding and calescence of droplets under the effect of various air shear speeds is investigated experimentally on aluminum substrate.

3.2 Experimental Setup

The experimental setup is designed to capture the shear driven coalescence behavior of two sessile droplets. As shown in Figure 3.1 the setup consists of the droplet positioner, the airflow injection and the high speed imaging systems. In this section detailed description of each part is provided.

Experiments are performed on a rectangular aluminum plate with a size of 150×75 mm^2 and thickness of 1 mm. The static contact angle of a water droplet on the polished aluminum plate is 75°± 1 which makes it hydrophilic. The contact angle hysteresis of the aluminum plate in these experiments is 18°± 2 which is measured based on the proposed method of Milne and Amirfazli [44]. They showed that in droplet shedding phenomenon, using the difference between the maximum (θ_{max}) and the minimum (θ_{min}) contact angles instead of the traditional method of hysteresis measurement (the difference between the advancing and receding contact angles) is more meaningful [44]. For the shear driven droplet shedding, θ_{max} and θ_{min} refer to the droplet contact angles downstream and upstream of the flow, respectively. As surface wettability is affected by dust and other impurities, the substrate was washed thoroughly with ethanol and distilled water and dried for 15 minutes before performing the experiments.

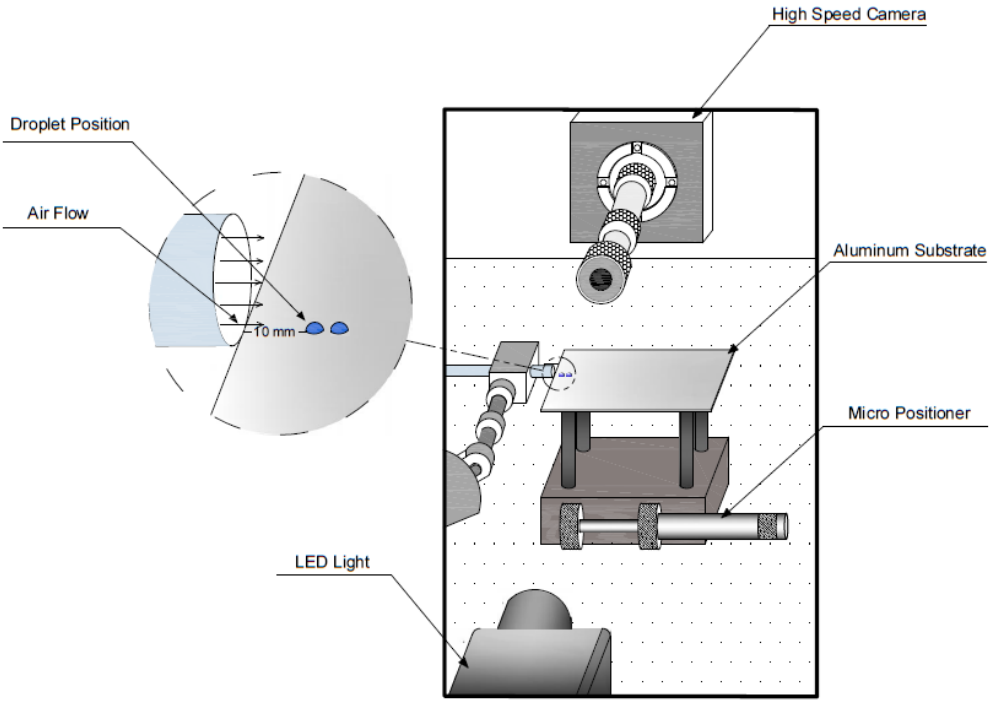

Figure 3.1 Experimental setup

It is known that in practical applications such as in-flight icing, the number of the droplets is more than one, and droplet coalescence occurs due to the air shear effect. Thus, in the present work the concurrent shedding and coalescing of the droplets are investigated under the effect of shear flow. Distilled water droplets were placed on the aluminum plate with a sterilized micro pipette (Sartorius, IL, USA). As the effect of air shear speed is the main focus of this study, the size of the droplets were kept constant at 5 µl in all the tests which corresponds to a spherical drop with a diameter of 2.1 mm. There was about 1 mm space between the two droplets (shown in Figure 3.2). The ambient and the droplets temperature was also preserved constant at 22 °C. As illustrated in Figure 3.2, the first droplet was deposited at 10 mm away from the leading edge of the substrate, as air stream is almost uniform and without any recirculating flow at and after this location.

Air flow was introduced on the aluminum substrate from a high pressure tank by using a tube with the length and the inlet diameter of 800 and 10 mm, respectively. The tube was placed at the substrate leading edge. Placing the substrate on a micro positioner (New Port, CA, USA) enables the precise movement of the substrate toward and from the tube (Figure 3.1). A high pressure valve was used to control the air speed. In the present study the air speed varied between 5 and 90 m/s and was measured with a Pitot tube (calibrated with the flow meter before experiments) at the point that the droplet was deposited on the substrate.

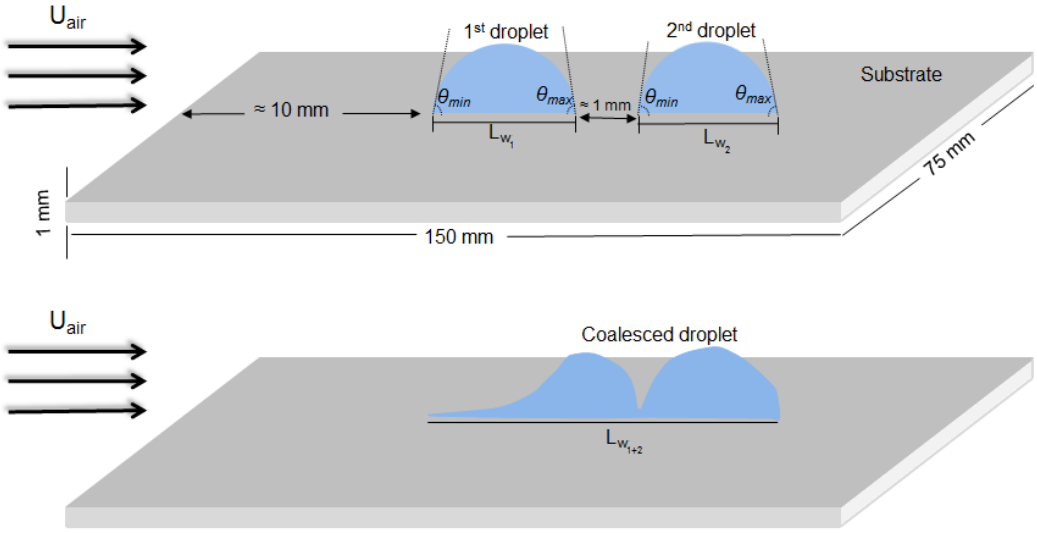

Figure 3.2 Schematic of the droplets' position on the substrate

Coalescence phenomenon occurs within micro seconds therefore, a Photron SA1.1 high speed camera (Photron, California USA) operating at 5400 frames/s with an UltraZoom 6000 lens (Navitar, New York USA) was used to record the process during the experiments. Shadowgraphy technique with backlighting was performed using an LED light (Schott, California USA) to capture the images throughout the whole process. By taking side and top view images from the shedding progression, a complete analysis can be conducted on droplet behavior. The experimental results of this work were processed with ImageJ software [78]. The

details of the post processing methodology with ImageJ can be found in [78]. To reach an acceptable degree of accuracy and repeatability each test was repeated minimum fifteen times and the results are reported based on the average of these fifteen experiments.

3.3 Results and Discussions

To observe the concurrent droplet coalescence and shedding, both side and top views of the coalescing droplets for the lowest (5 m/s) and the highest (90 m/s) air speeds are shown in Figure 3.3 and 3.4, respectively. As shown in Figure 3.3 for the air speed of 5 m/s the droplets only vibrate on the surface without resulting in shedding or droplet coalescence. In other words, the drag force on the droplet caused by 5 m/s of air speed is not high enough to overcome the droplets high adhesion force on the hydrophilic aluminum substrate. Consequently, increasing the air speed results in droplet movement on the substrate. Later on the droplets merge together and form one larger deformed droplet along the direction of the imposed shear flow. Due to the high adhesion of the droplets on the aluminum surface, under the effect of high air speed the coalesced droplet start to form a narrow stream of liquid known as rivulet. Rivulet formation on the aluminum substrate increases the surface area which is covered by water.

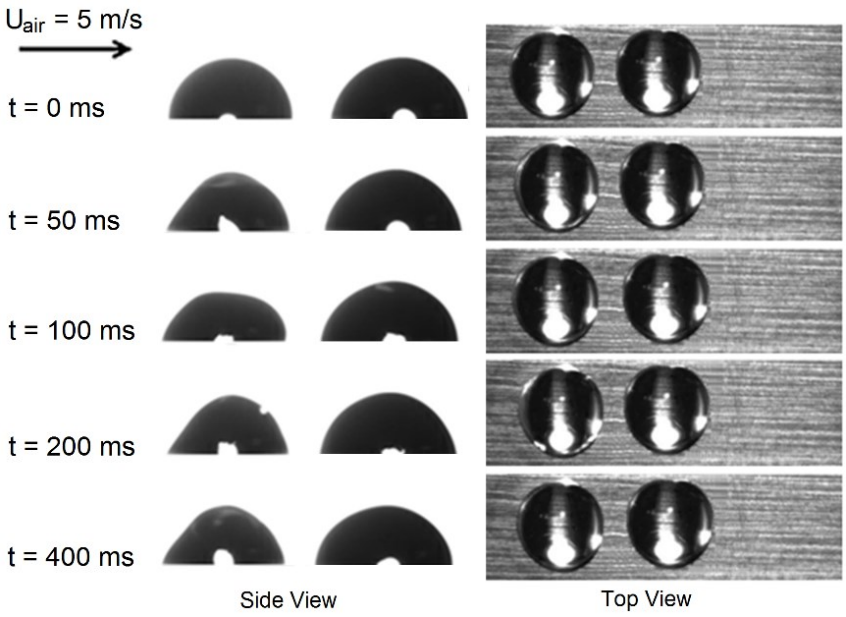

Figure 3.3 Sequences of the droplet shedding for an air speed of 5 m/s

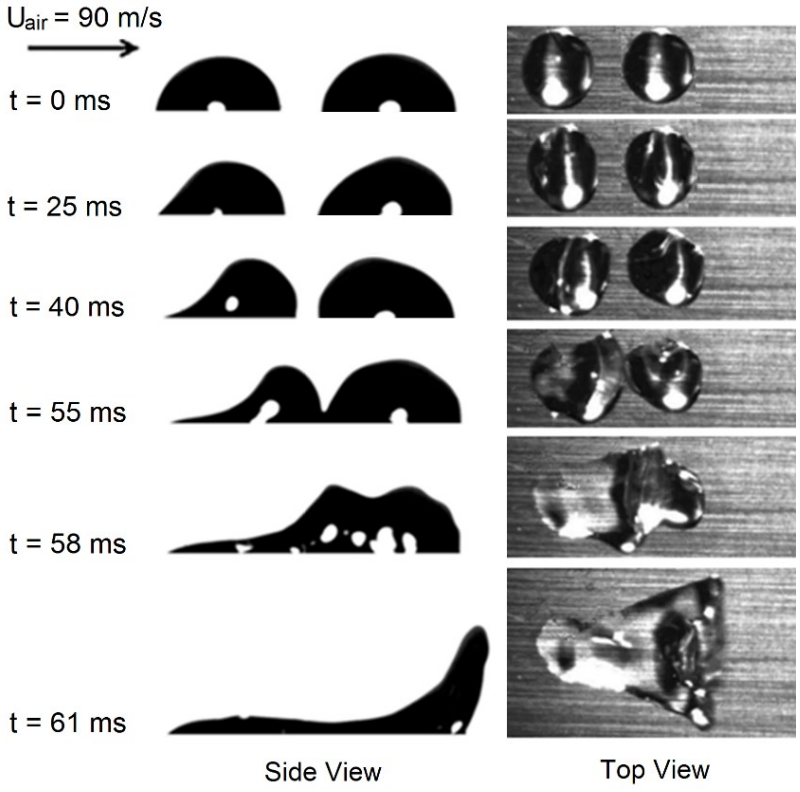

Figure 3.4 Sequences of the droplet shedding and coalescence for an air speed of 90 m/s

It is known that the droplet starts to move (shed) while the drag force caused by the airflow overcomes the adhesion force between the droplet and the substrate. These forces can be calculated from the following equations [44];

$$F_{drag} \propto \frac{1}{2}\rho u_{air}^2 S C_D \quad \textbf{Equation 3.1}$$

$$F_{adh} \propto L_w \sigma (cos\,\theta_{min} - cos\,\theta_{max}) \quad \textbf{Equation 3.2}$$

where, ρ and σ are the density and surface tension of the droplet, respectively. u_{air} and L_w are the air shear speed and the droplet wetting length, respectively (see Figure 3.2). S is the area of the droplet facing air flow and C_D is its drag coefficient. Variations of contact angle results in different droplet shapes. Therefore, both S and C_D are dependent on the droplet contact angle.

Droplets deformation during shedding arises from the variation of their upstream and downstream contact angles (i.e. θ_{min} and θ_{max}). These contact angle values were measured versus time at and after the incipient motion. According to Equation 3.2, the value of $(cos\,\theta_{min} - cos\,\theta_{max})$ is an indication of the amount of the adhesion force. Variations of the term $(cos\,\theta_{min} - cos\,\theta_{max})$ versus time are shown in Figure 3.5 and 3.6 for the first and the second droplets, respectively before getting coalesced. It is important to mention that the result of the contact angle variations is not plotted after coalescence because at that stage instead of the droplet, rivulet is formed on the aluminum plate.

As it is clearly shown in Figure 3.5, increasing air speed causes droplet deformation in a way that the term $(cos\,\theta_{min} - cos\,\theta_{max})$ increases with time. In other words the top part of the first droplet tends to move in the direction of the airflow toward the second droplet while its contact line is remained on the substrate. As higher shear flow enhances the droplet deformation, the slope of the diagrams in Figure 3.5 increases by increasing the airflow from 5 to 90 m/s. The increase in the amount of $(cos\,\theta_{min} - cos\,\theta_{max})$, results in an increase in the adhesion force of

the droplet. Therefore, the droplet stays on the surface, merges to the second droplet, and finally forms a runback flow (i.e. rivulet).

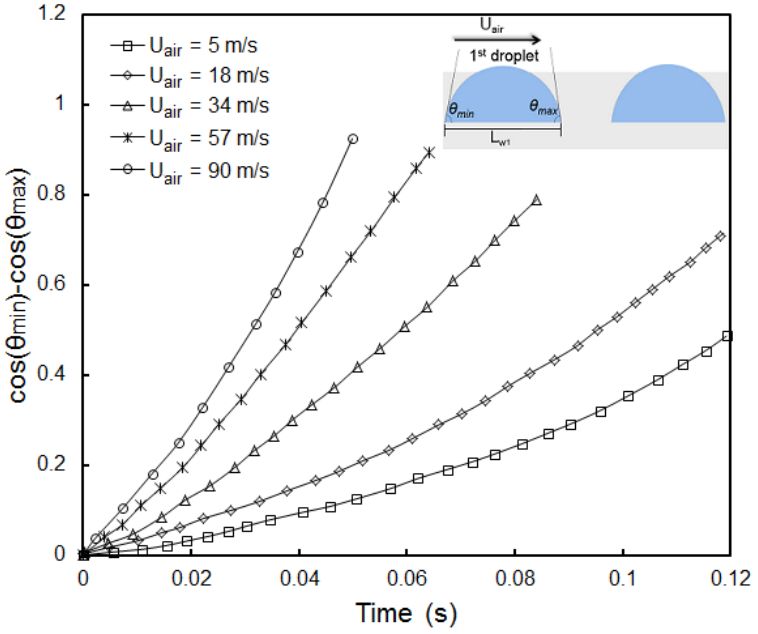

Figure 3.5 Variations of $(cos\,\theta_{min} - cos\,\theta_{max})$vs. time before coalescence for the first droplet

As shown in Figure 3.6, contact angle variations of the second droplet are in a way that the term $(cos\,\theta_{min} - cos\,\theta_{max})$ increases with time. Increasing the air speed results in faster increase of the $(cos\,\theta_{min} - cos\,\theta_{max})$. However, it should be noted that although at the beginning of the shedding process, $(cos\,\theta_{min} - cos\,\theta_{max})$ increases and the second droplet is moving in the direction of the air flow, at a certain point suddenly the second droplet tends to go toward the first droplet which results in decrease of the $(cos\,\theta_{min} - cos\,\theta_{max})$. The mentioned phenomenon occurs due to the presence of the first droplet. In other words, the wake formed behind the first droplet results in a drag force reduction on the second droplet. Consequently the second droplet's top part moves toward the first droplet and in the opposite direction of the air flow. After this point the droplets merge together and the coalescence occurs. Obviously, the second droplet's merge toward the first one and the decrease in the term $(cos\,\theta_{min} - cos\,\theta_{max})$

is more significant for higher speeds of 57 and 90 m/s. The coalescence time of the droplets for 18, 34, 57 and 90 m/s of air speed is about 0.12, 0.095, 0.07 and 0.05 s, respectively. It is clear from Figure 3.5 and 3.6 that higher air speed results in faster droplet coalescence and rivulet formation on the aluminum plate.

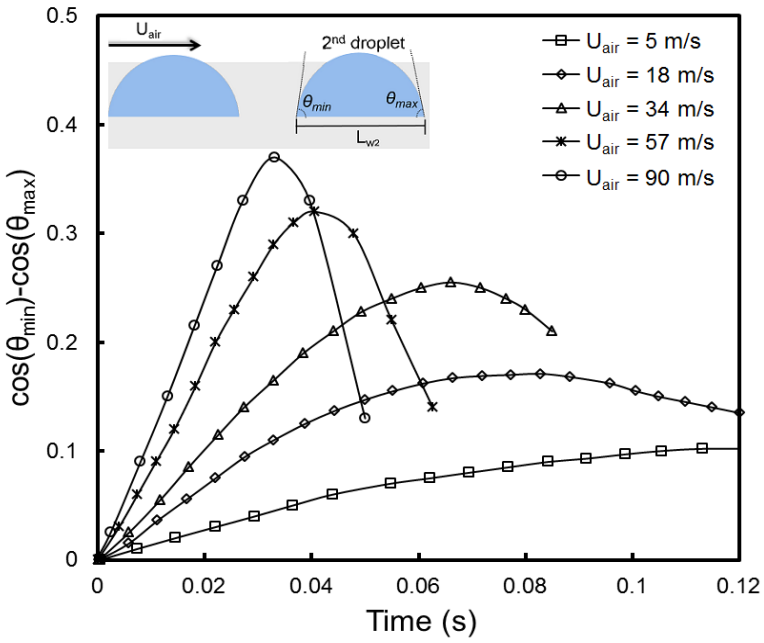

Figure 3.6 Variations of $(\cos\theta_{min} - \cos\theta_{max})$vs. time before coalescence for the second droplet

To probe the droplets behavior during shedding, the droplets wetting length on the substrate (L_w), was experimentally measured by image processing. Wetting length variation depends on contact angle, contact angle hysteresis, droplet size and the air shear speed. Among the mentioned parameters the effect of the shear speed is the aim of the current work. Hence, other parameters were kept constant during the experiments.

Variations of the first and coalesced droplets wetting length versus time for different air speeds are shown in Figure 3.7. As the second droplet's wetting length does not vary significantly with time it is not plotted in a separate graph. It is clear from Figure 3.7(a) that

when the air speed is low (5 m/s) there is no significant change in the wetting length of the first droplet (L_{w1}), and it does not move significantly on the surface. However, due to the high adhesion of the droplet to the aluminum substrate, higher air speeds result in an increase of the droplet wetting length. Shedding the merged droplets create a rivulet on the plate. Apparently the higher the air speed, the faster the coalescence and rivulet formation on the aluminum substrate.

To make the analysis easier, the variations of the droplets' wetting length after the coalescence (L_{w1+2}), is plotted in Figure 3.7(b) for different air speeds. It should be noted that in Figure 3.7(b), the results of the air speed of 5 m/s is not included as coalescence does not occur with this air speed. It is clearly shown in Figure 3.7(b) that rivulets form much faster by increasing the air shear speed. For example for the air speeds of 18, 34, 57 and 90 m/s the rivulets form at about 0.2, 0.15, 0.09 and 0.05 s, respectively. It should be noted that after the coalescence of the droplets, the wetting length of the coalesced droplet does not change significantly for a while, and suddenly an increase in (L_{w1+2}), is observed which is due to the complete rivulet formation. This delay is about 0.05 and 0.04 s for lower speeds of 18 and 34 m/s, respectively; which is higher than the delay for the higher speeds of 57 and 90 m/s that are about 0.015 and 0.005 s, respectively.

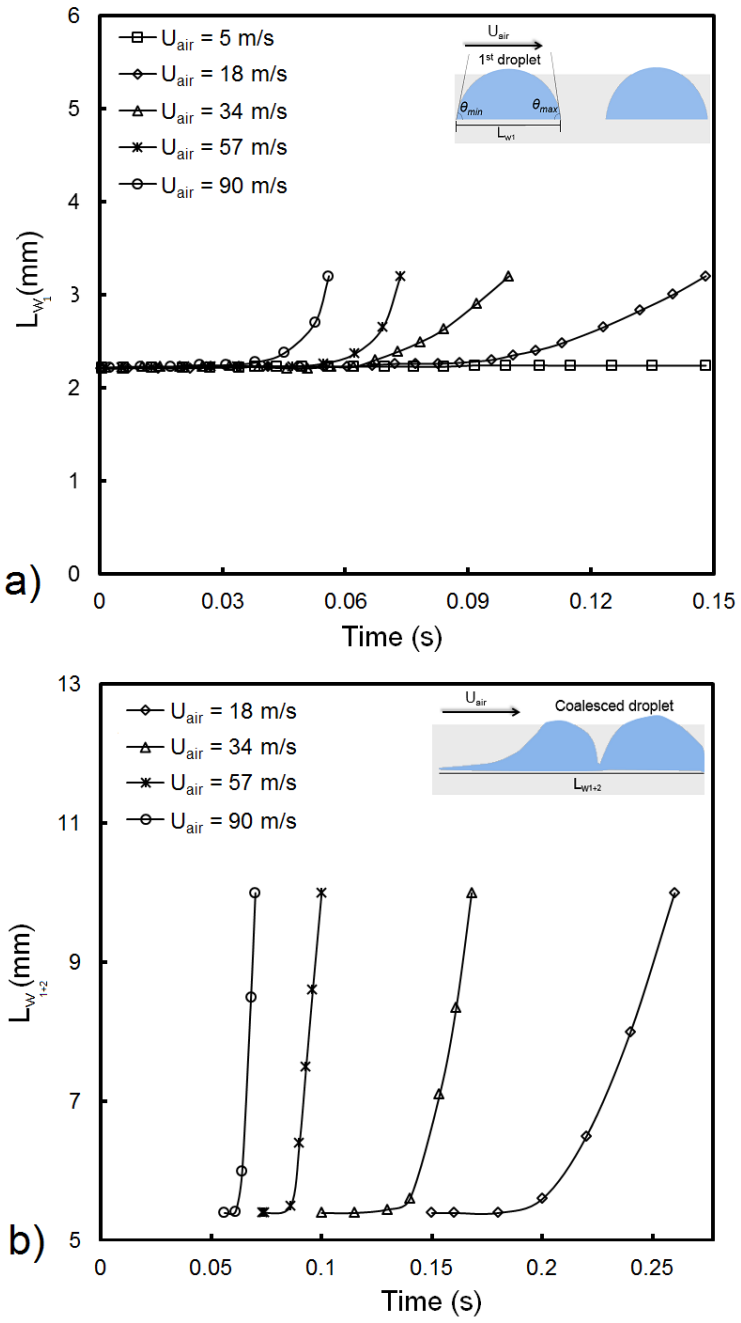

Figure 3.7 Variations of the wetting length vs. time for; a) first droplet and b) coalesced droplet

In this paper the period during which the coalesced droplet wetting length does not change significantly is called the residence time (T_r). The residence time of the coalesced droplets for different air speeds are shown in Figure 3.8. Increasing the air speed results in decrease of the residence time. In other words, the low air speed changes the shape of the coalesced droplet (see

Figure 3.8) in a way that at the earlier stages of the coalescence a thick oval shape droplet is formed on the plate. The amount of the drag force created by the low air speed of 18 m/s is not high enough to overcome the adhesion between the droplet and the aluminum plate. As a result for a period of t_r = 0.05 s, the leading and trailing edges of this oval shape drop is pinned on the substrate; hence its wetting length does not change significantly. After 0.05 s the oval shape droplet starts to become thinner and its leading edge moves downstream along the plate which leads to increase of the wetting length and the complete rivulet formation. Conversely, for the high air speed of 90 m/s the first droplet hits the second one with a higher momentum in comparison with the case of low air speed which results in the formation of a narrow rivulet with a semi spherical leading edge on the surface. The drag created by the high air speed is high enough to overcome the adhesion between this rivulet and the aluminum plate, as a result there will be a short residence time of 0.005 s for the coalesced droplet to form a complete rivulet on the substrate.

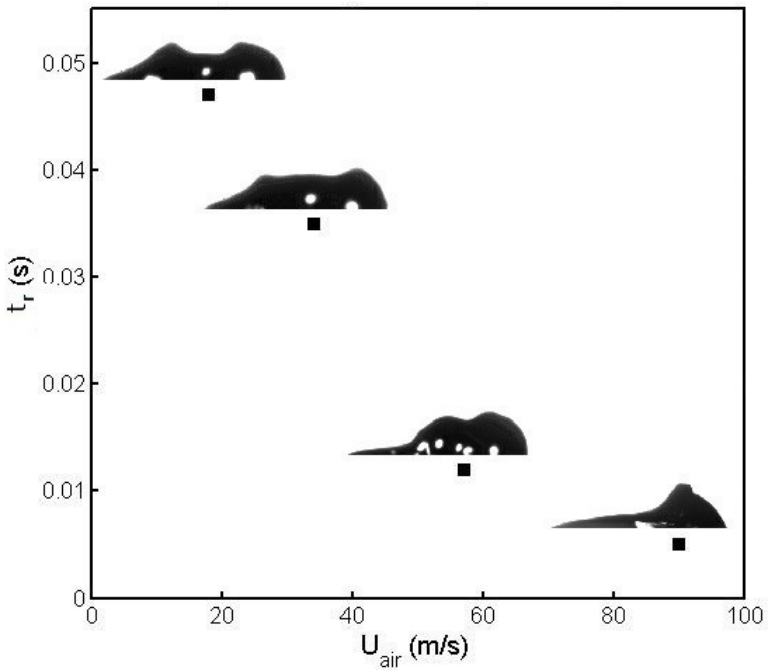

Figure 3.8 Residence time of droplet versus air speed after the coalescence point

3.4 Summary and Conclusions

An experimental study was conducted to investigate the effect of various air speeds as high as 90 m/s on droplet coalescence. It was shown that introducing shear flow to sessile droplets on an aluminum plate, results in droplet shedding, coalescence and formation of rivulets. It was displayed that during the coalescence process the first droplet moves in the direction of the air flow towards the second one. However, the second droplet moves in the opposite direction of the air flow towards the first droplet due to the wake that is created between the droplets. The droplets deformation was characterized based on the variation of their wetting length and contact angles for different air speeds during the coalescence phenomenon. It was demonstrated that the coalesced droplet is pinned to the aluminum plate and its wetting length does not change with time at the initial stages of the coalescence. It was observed that the residence time of the coalesced droplet on the plate increase by decreasing the air speed which is mainly due to the formation of a thick oval shape droplet with high adhesion to the aluminum plate. This study can be considered as a building block to analyze the rivulet formation caused by concurrent droplet shedding and coalescence especially for studying ice formation on aerodynamic components.

Chapter 4

Shear Driven Droplet Shedding and Coalescence on a Superhydrophobic Surface

"Reprinted with permission from Physics of Fluids Journal paper PF#14-1090GB [83]."

Abstract

The interest on shedding and coalescence of sessile droplets arises from the importance of these phenomena in various scientific problems and industrial applications such as ink-jet printing, painting, ice formation on wind turbine blades, power lines, nacelles and aircraft wings. For example in the case of aircraft icing the system aerodynamic efficiency is significantly reduced which may cause serious damages. It is shown recently that one of the ways to reduce the probability of ice creation is to have airfoils with superhydrophobic surface on which rain droplets can roll off instead of getting accumulated. Therefore, studying water droplet behavior i.e. shedding and coalescence is an important stage that leads to understanding the underlying physics of icing phenomenon on critical components such as airfoils, power lines or wind turbine blades. In this study a combined experimental and numerical approach is used to investigate droplet shedding and coalescence phenomena under the influence of air shear flow on a superhydrophobic surface. Droplets with a size of 2 mm are subjected to various air speeds ranging from 5 to 90 m/s. A numerical simulation based on the Volume of Fluid (VOF) method coupled

with the Large Eddy Simulation (LES) turbulent model is carried out in conjunction with the validating experiments to shed more light on droplets coalescence and detachment phenomena through a detailed analysis of the aerodynamics forces and velocity vectors on the droplet and the streamlines around it. The results indicate a contrast in the mechanism of two-droplet coalescence and subsequent detachment with those related to the case of a single droplet shedding. At lower speeds (i.e. 5 m/s) the two droplets coalesce by attracting each other with successive rebounds of the merged droplet on the substrate, while at higher speeds (i.e. 90 m/s) the detachment occurs almost instantly after coalescence, with a detachment time decreasing exponentially with the air speed. It is shown that coalescence phenomenon assists droplet detachment from the superhydrophobic substrate at lower air speeds.

4.1 Introduction

Droplet movement under the effect of air shear flow is called shedding which has various industrial applications among them the prominent ones are ink-jet printing, spray coating [29, 30], rain drop formation in clouds [40, 41] and icing phenomenon that occurs on turbine blades, power lines and airfoils [43]. Droplet shedding happens if the drag force caused by the air shear flow overcomes the droplet adhesion force to the solid substrate (see Figure 4.1).

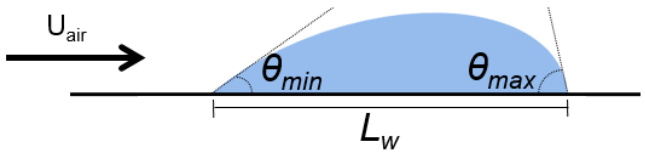

Figure 4.1 Schematic of the shedding phenomenon

The drag force created by the shear flow and the adhesion force of the droplet to the substrate can be described by the following equations [44];

$$F_{drag} \propto \frac{1}{2}\rho u_{air}^2 S C_D \quad \textbf{Equation 4.1}$$

$$F_{adh} \propto L_w \sigma(cos\,\theta_{min} - cos\,\theta_{max}) \quad \textbf{Equation 4.2}$$

where, ρ and σ are the density and surface tension of the droplet, respectively. S is the droplet area facing air flow. Air shear speed and the droplet wetting length are denoted by u_{air} and L_w, respectively (see Figure 4.1). The starting point of the droplet shedding is called the incipient motion and after this point the droplet starts to move along the surface [44].

In the above mentioned applications as the number of droplets is usually more than one, simultaneous droplet shedding and coalescence may occur. This study is mainly driven by the interest in mitigating ice on aerodynamic surfaces using superhydrophobic coatings. When rain droplets hit an aircraft wing, under the effect of shear flow over the airfoil they may coalesce and form a larger droplet. Depending on the airfoil surface properties and the air shear effect, the merged droplets may create a runback flow in the form of a thin film (i.e. rivulet). At temperatures below the water freezing point, the rain droplets and rivulets turn into ice. Ice accumulation adversely effects the aerodynamic characteristics of the airplane by increasing the drag and reducing the lift forces [6].

Droplet coalescence is a phenomenon in which two droplets join together and form a larger one. During the coalescence process the two droplets touch each other from their circumference. As a result a neck shape bridge is formed at the droplets interface (see Figure 4.2). The height of the bridge (h) grows with time up to the point that the two droplets merge and form a single droplet. The coalesced droplet has a lower surface area which corresponds to surface energy

minimization [45]. Although droplet coalescence phenomenon has been investigated over a centenary [46], it is still an active topic of research due to its both scientific and industrial applications.

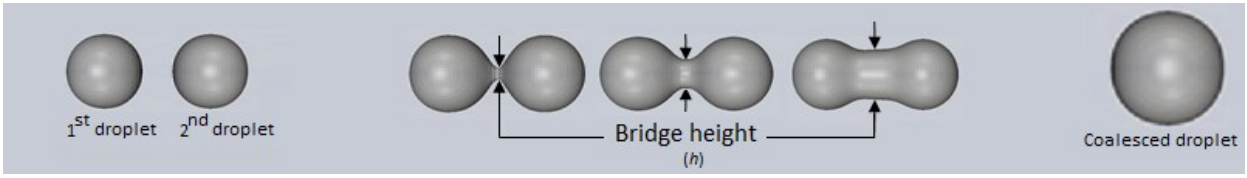

Figure 4.2 Schematic of the bridge height growth during coalescence process

The coalescence of two highly viscous droplets that are not touching any surface was first investigated about seventy years ago by Frenkel [46]. He concluded that when two free droplets (not touching any surface) touch each other, the flow is initially in the viscous regime since the bridge height (depicted in Figure 4.2) is significantly smaller than the viscous characteristic length. For the droplets with low viscosity because the neck and consequently the bridge radius starts to grow after merging, the flow regime changes from viscous to inertial. When the inertial flow regime is dominant the droplets' merging is subjected to the competition between the inertia and the surface tension. Therefore in this case an inviscid assumption can be made as emphasized in the literature [30, 47, 48]. However, if the droplets have high viscosity, the coalescence phenomenon occurs in a longer time. Coalescence of two droplets in a viscous regime was done with direct numerical simulation in the work of Van de Vorst [49, 50].

The mechanism of coalecencing droplets that are placed on a surface is different from that of the free droplets especially in the case of hydrophilic substrates. The reason is that when the droplets wet the substrate the coalescence dynamics is mainly affected by the viscous stresses that the substrate imposes on the droplets [51]. In the work of Ristenpart *et al.* [51] it was shown that the droplet geometry also plays an important role on the coalescence growth rate. Various

experimental and theoretical studies are performed on the coalescence of a droplet placed on wettable surfaces with contact angles of less than 60^o [45, 54]. If the surface is partially wettable the coalescence dynamics tends to be similar to the free droplet case [40, 52, 53]. The evolution of the bridge height during droplet coalescence on partially wettable surfaces was studied extensively in the work of Lee *et al*. [45]. They concluded that as the droplets used in their work were sufficiently small, the coalescence process corresponds to the viscosity dominant creeping flow. They also pointed out that coalescence process in their work is affected by both the viscous bulk stress and the viscous friction caused by the substrate. Accordingly their results deviate from the coalescence of highly viscous free drops described by Frenkel in his work [46].

In addition to the mentioned works which were dedicated to the physics of coalescence only, this phenomenon was also studied under the effect of different surface wettabilities. Numerical and experimental analyses of droplet impact on already rested sessile droplet on a superhydrophobic surface was studied by Farhangi *et al*. [23]. They showed that due to the normal impact of the second droplet on the first one, the resulting coalesced droplet will be removed from the superhydrophobic surface. Graham *et al*. [55] investigated similar work on surfaces with various wettabilities ranging from hydrophilic to super hydrophobic both numerically and experimentally.

Despite the above mentioned studies, the effect of shear driven shedding and coalescence of droplets especially with high air shear speeds that corresponds to the flight condition has not yet been reported. As mentioned before, one of the applications of the concurrent droplet shedding and coalescence is in aerospace industry especially for in-flight icing condition. A deep analysis of the simultaneous droplet shedding and coalescence under the effect of high shear flow can be one of the key points to this goal. Milne and Amirfazli [44] investigated the incipient motion of

single droplet under the effect of air flows as high as 30 m/s on different surface wettabilities. To address the effect of higher air speeds Moghtadernejad *et al*. [74] performed the single droplet shedding analysis on hydrophilic and superhydrophobic substrates with air speeds as high as 90 m/s. Despite the above mentioned studies, the coalescence of droplets under the effect of air shear flow is still a questionable topic. Due to the importance of this topic from both scientific and industrial point of view, in this work the concurrent shedding and coalescence phenomena of two droplets under the effect of air speeds as high as 90 m/s (similar of those in flight condition) will be investigated in detail both experimentally and numerically based on the Volume of Fluid (VOF) method coupled with Large Eddy Simulation (LES) turbulence model.

4.2 Experimental Setup

The experimental setup is designed to capture the concurrent shedding and coalescence behavior of two droplets under the effect of air shear flow. As shown in Figure 4.3 the setup consists of a droplet positioning system, air flow injection system and imaging tools (high speed camera and LED light). To create the superhydrophobic surfaces, rectangular polished aluminum plates with a size of 150×75 mm^2 and a thickness of 1 mm were coated with WX2100 spray (Cytonix, Maryland, USA). As dust and other impurities can affect surface wettability, the substrates were cleaned with ethanol and distilled water and dried for 15 minutes. The cleaned substrates were then coated with WX2100 spray three times. The substrates were dried for two hours before applying the second and the third coatings. The SEM images of the superhydrophobic substrate with the magnification of 2500X and 15000X is shown in Figure 4.4

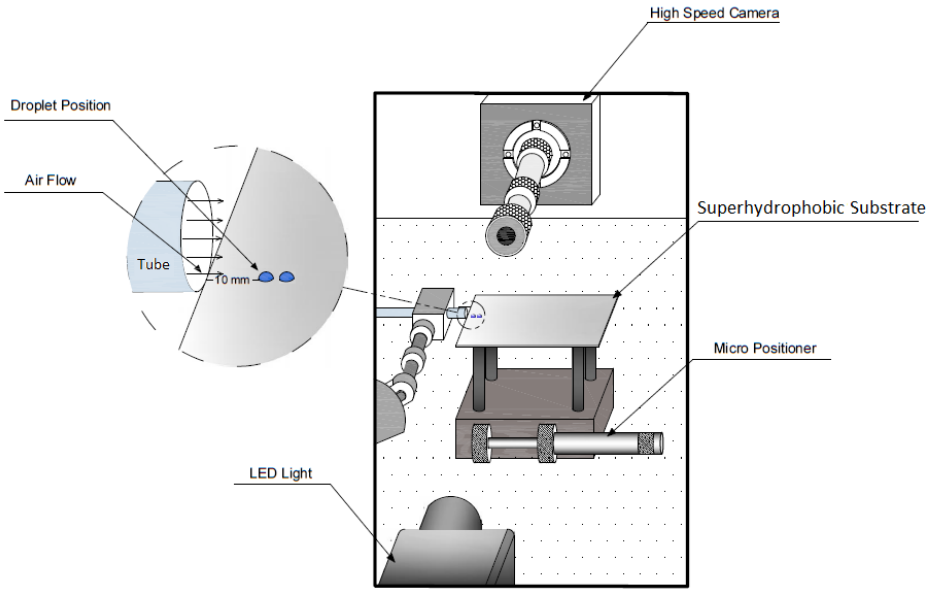

Figure 4.3 Experimental setup

The water droplet static contact angle on the produced superhydrophobic coating was around 155±1 º which was measured at different locations of the coated plate. The contact angle hysteresis on the superhydrophobic plate was 8±2 º which was measured based on the proposed method of Milne and Amirfazli [44]. They showed that during droplet shedding phenomenon, using the difference between the maximum (θ_{max}) and minimum (θ_{min}) contact angles is more representative [44]. For the shear driven droplet shedding, θ_{max} and θ_{min} refer to the droplet contact angles downstream and upstream of the flow, respectively.

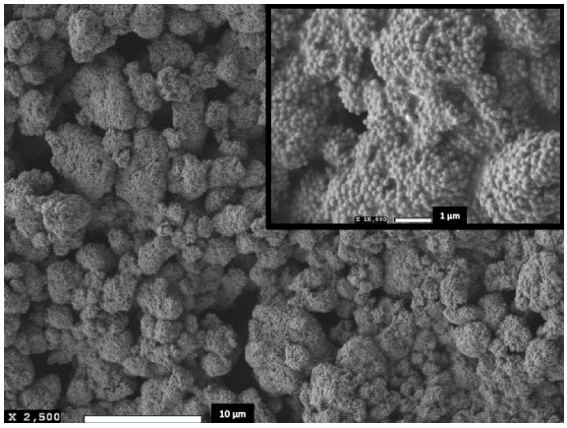

Figure 4.4 SEM image of the WX2100 substrate with 2500X magnification. The specified area at the top right corner has the magnification of 15000X [80]

Air was introduced on the substrate from a high pressure tank by using a tube with a length and diameter of 800 and 10 mm, respectively. The tube is placed at the substrate leading edge as shown in Figure 4.3. Placing the substrate on a micro positioner (New Port, CA, USA) enables the precise movement of the substrate toward and from the tube. To control the air speed a high pressure valve was used. The air speed varied from 5 to 90 m/s and was measured with a pitot tube at the location that the droplet was deposited on the substrate. Distilled water droplets were deposited on the surface with a sterilized micro pipette (Sartorius, IL, USA). As the effect of the air speed is the main focus of this study, the size of the droplets were kept constant at 5 µl in all the tests which corresponds to a spherical 2.1 mm diameter droplet. The water droplet temperature was also kept constant at 22 ^{o}C. As schematically shown in Figure 4.5, the first droplet was deposited 10 mm away from the leading edge of the substrate as the air stream is smooth and without any significant vortices at and after this location. The second droplet was deposited at about 1 mm distance from the first one. The droplets were subjected to the air flow immediately after placing them on the superhydrophobic substrate.

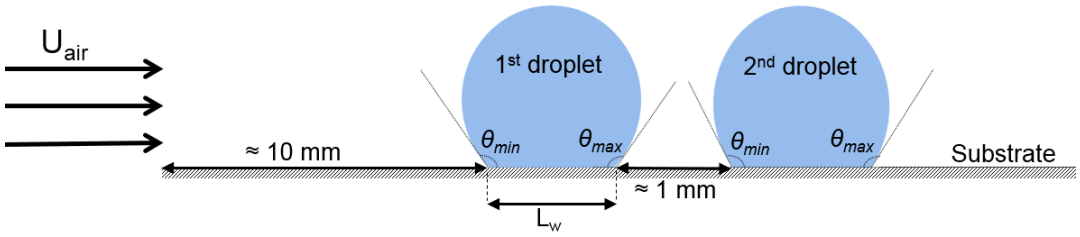

Figure 4.5 Schematic of the position of two droplets on the substrate

As the coalescence phenomenon occurs within micro seconds, a Photron SA1.1 high speed camera (Photron, California USA) operating at 5400 frames/s with an UltraZoom 6000 lens (Navitar, New York USA) was used to capture the process throughout the experiments. Shadowgraph technique with backlighting was performed to capture the shedding progression

using an LED light (Schott, California USA). The droplets deformation were analyzed by taking the side and top view images from the shedding evolution. To reach an acceptable degree of accuracy and repeatability each test was repeated at least fifteen times and the results are reported based on the average of these fifteen experiments. The experimental results in this work were post-processed with ImageJ software, the details of which can be found in [78].

4.3 Numerical Method

The numerical approach used in the current study is based on the VOF coupling with LES turbulence model. An incompressible Navier Stokes set of equations is considered based on an OpenFOAM code [84] including continuity and momentum equations.

$$\nabla . \boldsymbol{V} = 0 \qquad \textbf{Equation 4.3}$$

$$\frac{\partial \rho \boldsymbol{V}}{\partial t} + \nabla . (\rho \boldsymbol{V}\boldsymbol{V}) = -\nabla p + \rho \boldsymbol{g} + \nabla . \left(\mu(\nabla \boldsymbol{V} + \nabla \boldsymbol{V}^{\boldsymbol{T}})\right) + \sigma \kappa \nabla \alpha \qquad \textbf{Equation 4.4}$$

where $\boldsymbol{V}$ is the velocity vector, t is time, p is the pressure, $\boldsymbol{g}$ is the gravitational acceleration, σ is the surface tension, κ is the surface curvature and α is the volume fraction whose value is unity in the liquid phase and zero in the gas. When a cell is partially filled with liquid, α has a value between zero and one [85]. The weighted average mixture density and viscosity based on the distribution of the liquid volume fraction are described below;

$$\rho = \alpha \rho_l + (1-\alpha)\rho_g \qquad \text{and} \qquad \mu = \alpha \mu_l (1-\alpha)\mu_g \qquad \textbf{Equation 4.5}$$

where the subscripts l and g denote the liquid and gaseous phases, respectively.

The continuum surface force (CSF) method of Brackbill *et al*. [86] is used to model surface tension as a body force (F_σ) that acts only on interfacial cells;

$$F_\sigma = \sigma\kappa\nabla\alpha \quad \textbf{Equation 4.6}$$

$$\kappa = -\nabla.\left(\frac{\nabla\alpha}{|\nabla\alpha|}\right) \quad \textbf{Equation 4.7}$$

It is crucial in numerical simulations of free surface flows using VOF model, to assure boundedness and conservativeness of the phase fraction. Following the method detailed in [87], the volume fraction equation is formulated with a bounded compression scheme, which facilitates a sharp interface between phases. This is achieved by introducing an extra artificial compressive term into the volume fraction equation given below;

$$\frac{\partial\alpha}{\partial t} + \boldsymbol{V}.\nabla\alpha + \nabla.[\boldsymbol{V}_c\alpha(1-\alpha)] = 0 \quad \textbf{Equation 4.8}$$

where, $\boldsymbol{V}_c$ is the vector of relative velocity normal to the interface which is used to compress the interface;

$$\boldsymbol{V}_c = \boldsymbol{n}min\left[C_a\frac{|\varphi|}{|S_f|}, max\frac{|\varphi|}{|S_f|}\right] \quad \textbf{Equation 4.9}$$

where φ, S_f, C_α and $\boldsymbol{n}$ are the face volume flux, cell face area vector, compression coefficient and face unit normal flux, respectively. C_α is an adjustable coefficient used to adjust the amount of compression. Here C_α = 1.5, which is also shown by Rusche [87] to provide a sharp interface between phases. The main benefit of such formulation is in the possibility of capturing the interface region much more sharply in comparison to the classical VOF approach. The face unit normal also is defined by the equation below. Nothing that in practical computations, due to avoiding zero value at the denominator of $\boldsymbol{n}$, a small value of δ_n is used (e.g. 10^{-5}).

$$\boldsymbol{n} = \frac{(\nabla\alpha)}{|(\nabla\alpha)+\delta_n|} \quad \textbf{Equation 4.10}$$

The interaction with the substrate is handled through the dynamic contact angle. The accuracy in droplet dynamics is highly related to the way that the dynamic contact angle (θ_D) is modeled. Here the contact angle is implemented using the correlation by Kistler [88];

$$\theta_D = f_H\left[Ca + {f_H}^{-1}(\theta_E)\right] \quad \textbf{Equation 4.11}$$

where the capillary number is $Ca = \mu U_{cl}/\sigma$ while the Hoffman function (f_H), [88] is given by;

$$f_H(s) = arc\cos\left\{1 - 2\tanh\left[5.16\left[\frac{s}{1+1.31s^{0.99}}\right]^{0.706}\right]\right\} \quad \textbf{Equation 4.12}$$

The contact line velocity is U_{cl} which is approximated by using the velocity at the interface in the first computational point above the wall. In order to account for the hysteresis effect in the numerical model, the equilibrium contact angle θ_E in Equation 4.11 is replaced by either the advancing contact angle, θ_A, or the receding contact angle, θ_R, depending on the direction of the velocity at the contact line. This implementation makes our model unlike the one reported in the literature, to not rely systematically on experiments for imposing the contact angle.

In order to accurately capture vortices including in both gas and the liquid, LES turbulence model is coupled with the VOF method. To capture the high speed shedding of the droplet an eddy-viscosity model is used, which is robust in practice and accounts for the dissipative nature of turbulent flow [89]. In LES, the coherent structures and large-scale turbulence are resolved, while the Sub Grid Scale (SGS) effects on the large or grid scale, is modelled.

In LES it is assumed that the velocity $\boldsymbol{V} = \overline{\boldsymbol{V}} + \acute{\boldsymbol{V}}$, corresponds to the contribution of both the GS and SGS components. The filtered fields, $\overline{\boldsymbol{V}} = G * \boldsymbol{V}$ results from the convolution of **V** by the kernel $G = G(\mathbf{x}, \Delta)$, which is a function of **x** and the filter width (Δ). By filtering the Navier-Stokes (Equation 4.4), the resulting equation expresses as follows;

$$\frac{\partial(\rho\overline{\boldsymbol{V}})}{\partial t} + \nabla.(\rho\overline{\boldsymbol{V}}\overline{\boldsymbol{V}}) = -\nabla\overline{p} + \rho\boldsymbol{g} + \nabla.(\overline{\boldsymbol{S}} - \boldsymbol{B}) + \sigma\kappa\nabla\alpha \quad \textbf{Equation 4.13}$$

The SGS modelling of the tensor ($\boldsymbol{B}$) is derived based on the fact that the deviatoric part of the SGS stress tensor is locally aligned with the filtered rate of the strain tensor deviatoric contribution [89] as is given below.

$$\boldsymbol{B} = \overline{\boldsymbol{V}\boldsymbol{V}} - \overline{\boldsymbol{V}}\,\overline{\boldsymbol{V}} = \frac{2}{3}k_{sgs}\boldsymbol{I} - 2v_{SGS}(\overline{\boldsymbol{S}} - \frac{1}{3}\,tr(\overline{\boldsymbol{S}}))I \qquad \textbf{Equation 4.14}$$

Finally, to close the system, the constant coefficient one-equation eddy-viscosity model can be described following the evolution of the turbulent kinetic energy [90, 91].

$$\frac{\partial k_{sgs}}{\partial t} + \nabla.\left(k_{sgs}\overline{\boldsymbol{V}}\right) = \nabla.\left[(v + v_{SGS})\nabla k_{sgs}\right] - \varepsilon_t - v_{SGS}\bar{S}^2 \qquad \textbf{Equation 4.15}$$

In Equation 4.15, the left-hand side corresponds to the change of the turbulent SGS kinetic energy with respect to time. The second term describes convection and the third, diffusion. The other parameters $\boldsymbol{S}$, ε_t and v_{SGS} are given by the following relations;

The rate of strain tensor; $\overline{\boldsymbol{S}} = \frac{1}{2}(\nabla\overline{\boldsymbol{V}} + (\nabla\overline{\boldsymbol{V}})^T)$

The turbulent dissipation; $\varepsilon_t = \Delta c_\varepsilon {k_{sgs}}^{1.5}$, $\quad c_\epsilon = 1.05$

The turbulent viscosity; $v_{SGS} = \Delta c_k {k_{sgs}}^{0.5}$, $\quad c_k = 0.07$

The simulations are performed in parallel using domain decomposing mesh. The PIMPLE algorithm combining the Pressure Implicit with Splitting of Operators (PISO) and the SIMPLE algorithms are used to calculate the pressure and velocity fields using a geometric-algebraic multi-grid (GAMG) solver. In addition, using a dynamic adaptive mesh refinement technique enables simulating the similar conditions as the experimental observations.

Geometry and boundary conditions

The computational domain for investigating the droplet shedding is depicted in Figure 4.6. 2574000 cells are used with finer mesh near the wall, about 40 cells per diameter of the droplet, and coarser mesh above the deposit droplet. The boundary conditions of this geometry are fixed pressure on the outlet, a periodic boundary on the lateral side, while a fixed velocity is applied at the inlet. The no-slip boundary is used for the velocity at the wall. The value of turbulent kinetic energy $k = 1.5(u_{air}I)^2$ is implemented using a turbulence intensity of *I*= 5%. The droplets are

initially deposited on the surface until reaching their equilibrium position. Following the droplets deposition, an inlet air velocity is increased uniformly which subsequently causes the droplet to move more or less rapidly depending on the velocity magnitude. To compare with the experiments, a temporal ramp evolution is used for the inlet velocity (V_o) the timescale (τ) of which is found based on the tube length (L= 800 mm) as follows;

$$\tau = {}^{L}/_{u_{air}} \qquad \textbf{Equation 4.16}$$

$$V_o = \frac{u_{air}}{\tau} t = {u_{air}}^2 Lt \qquad \textbf{Equation 4.17}$$

where u_{air} is the velocity measured with the pitot tube at the droplet location. Although the initial inlet velocity may play a role in the droplet dynamics quantitatively, the overall droplet dynamics is well captured by this choice.

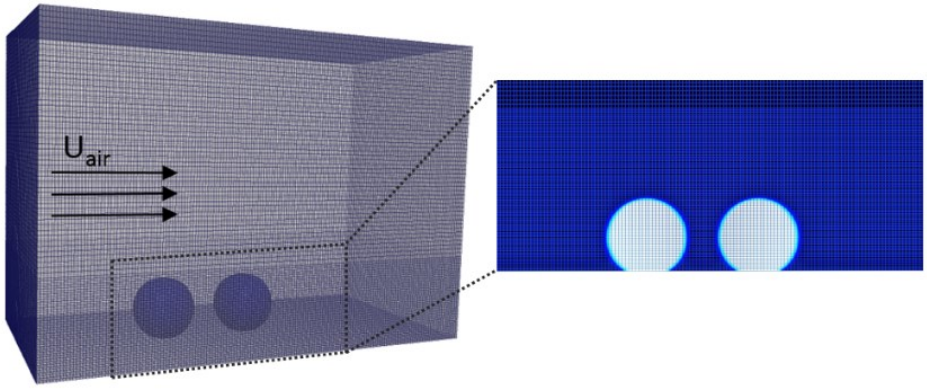

Figure 4.6 Computational domain

4.4 Results and Discussions

As mentioned above, the experiments in this paper were performed with two droplets at room temperature (22 ^{o}C) to analyze the concurrent shedding and coalescence phenomena on the superhydrophobic substrate under the effect of air speeds as high as 90 m/s. To probe the shedding and coalescence behavior of the droplet during the process, the results of this study are

categorized based on the lowest (5 m/s) and the highest (90 m/s) air speeds to avoid repeating the details of the medium speeds (more than 18 m/s) that are phenomenologically the same as the results of 90 m/s.

Droplet coalescence at low speed

The side and top view images of the coalecencing droplets are shown in Figure 4.7 for the lowest (i.e. 5 m/s) air speed. In addition to the experimental results, the results of numerical simulations at the same time intervals are presented for comparison. As shown in the figure, by introducing the air flow, the first droplet starts to roll on the surface, interestingly the second droplet tends to go towards the first one. The two droplets first touch each other at about 55 ms after imposing the shear flow. Due to the merging of the two droplets and the subsequent oscillation resulting from the conversion between surface energy and kinetic energy, the coalesced droplet detaches from the substrate at about t= 72 ms. However, as the drag and lift forces resulting from 5 m/s of air speed are not high enough to overcome gravity, the droplet comes back to the surface at t= 83 ms. Hence, for the low speed of 5 m/s unlike the single droplet case shown in the work of Moghtadernejad *et al*. [74] that the coalesced droplet only rolls on the superhydrophobic plate, in the two droplets case the coalesced droplet detaches from the surface and consequently lands on the substrate.

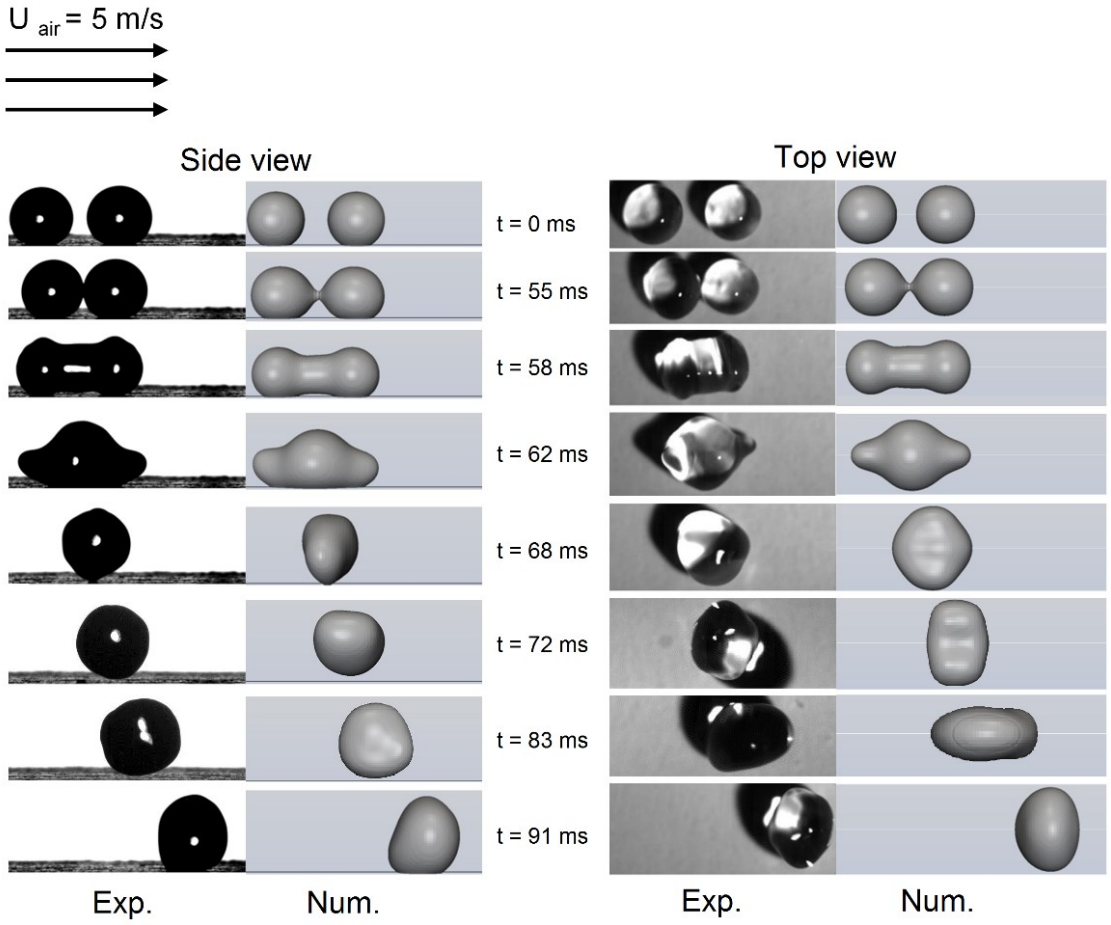

Figure 4.7 Sequences of the two droplets shedding and coalescence at an air speed of 5 m/s

To analyze the details of the coalescence phenomenon for the case of 5 m/s air speed, the simulated streamline colored by the pressure over the droplets in addition to the velocity vectors on the droplet surface during the coalescence phenomenon are shown in Figure 4.8.

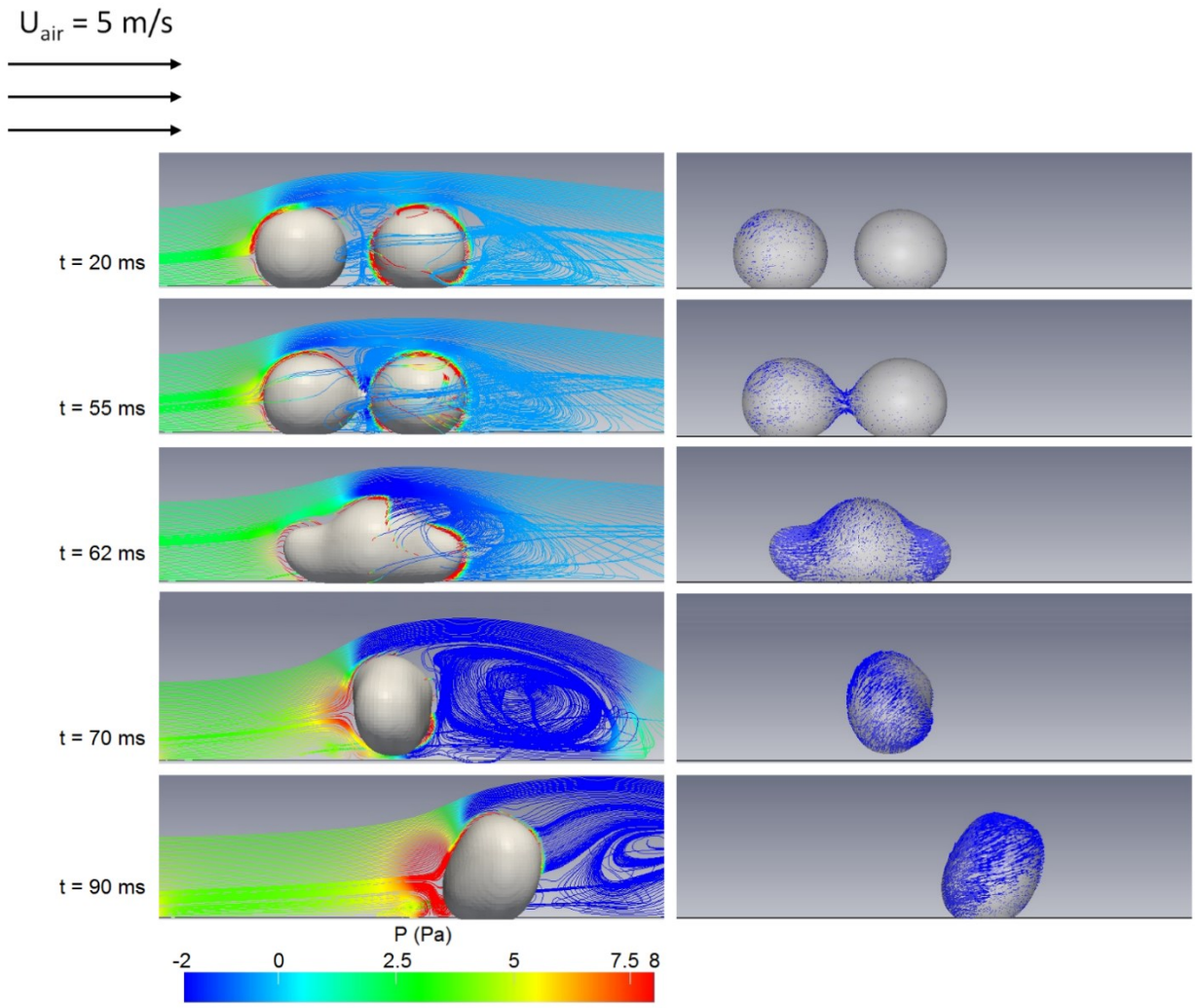

Figure 4.8 Simulation results for the coalescence of two droplets at an air speed of 5 m/s

As it is demonstrated in Figure 4.8 at the earlier stages of the coalescence phenomenon (t= 20 s) the first droplet is rolling on the surface in the direction of the air flow. Due to existence of separation bubble behind the first droplet (see the stream lines at t= 20 ms), pressure decreases between the droplets which makes the second droplet to get attracted to the first one (in the opposite direction of the air flow). Consequently, the two droplets touch each other for the first time at t= 55 ms, after merging a larger droplet forms at t= 62 ms. The coalesced droplet detaches from the surface due to oscillations arises from the conversion between surface energy

and kinetic energy at t= 70 ms. As the lift force created by 5 m/s of air speed is not high enough to overcome the weight of the droplet, the droplet comes back to the substrate.

To get a better understanding of the shear driven coalescence phenomenon, variations of the aerodynamic forces (i.e. drag and lift) are determined by integrating the pressure field over the droplet surface area (S_{drop}) as below;

$$\boldsymbol{F}_p = \int_{S_{drop}} p\boldsymbol{n}dS \qquad \textbf{Equation 4.18}$$

The projection of the pressure forces on the droplet with respect to the two axis leads to the drag (F_{drag}) and lift (F_{lift}) forces, respectively on the deposited droplet on the substrate. Noting that the drag and lift forces calculated on the first and the second droplets separately in addition to the forces computed on the merged droplet.

$$F_{drag} = \boldsymbol{F}_p.i, \quad F_{lift} = \boldsymbol{F}_p.j \qquad \textbf{Equation 4.19}$$

The drag force on the droplets for the air speed of 5 m/s is plotted in Figure 4.9 which is about zero at the beginning of the process as there is no air flow. However, after about 50 ms (when the droplets are about to touch each other) there is an increase of about 0.06 mN in the drag force acting on the first droplet. Due to the wake region between the two droplets, the upstream pressure of the second droplet is less than that of the downstream. Hence there will be a net drag force acting on the second droplet in the opposite direction of the air flow which makes it move towards the first droplet. Consequently, the values of the second droplet drag force is negative before merging to the first droplet. At about 55 ms the droplets merge together and after that the drag force on the coalesced droplet periodically changes with time due to its deformation (see the top view images in Figure 4.7) from a blunt body (e.g. t= 68 ms) to slender body (e.g. t= 83 ms).

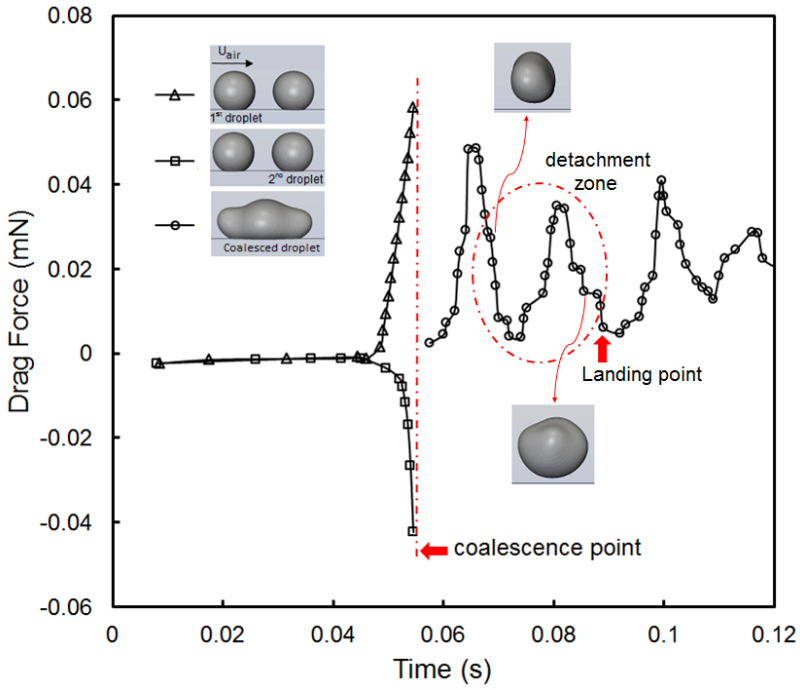

Figure 4.9 Drag force on the droplets at an air speed of 5 m/s

Variations of the lift force for the first and second droplets are shown in Figure 4.10. The lift force of the two droplets does not change significantly before the coalescence point as the droplets remain on the surface during this time. Although at the earlier stages of the process, the lift force has minor negative values due to the effect of air flow on the droplets which pushes down the top of the droplets. However, after the coalescence (t= 55 ms) there are significant changes in the amount of lift force. When the coalesced droplet lifts off from the surface the lift force increases (at t= 72 ms). Variations of the lift force at this stage is due to the droplet deformation from a blunt body to a slender body. When the droplet retouches the surface (at about t= 83 ms) the lift force becomes negative and varies with time due to the droplet shape change.

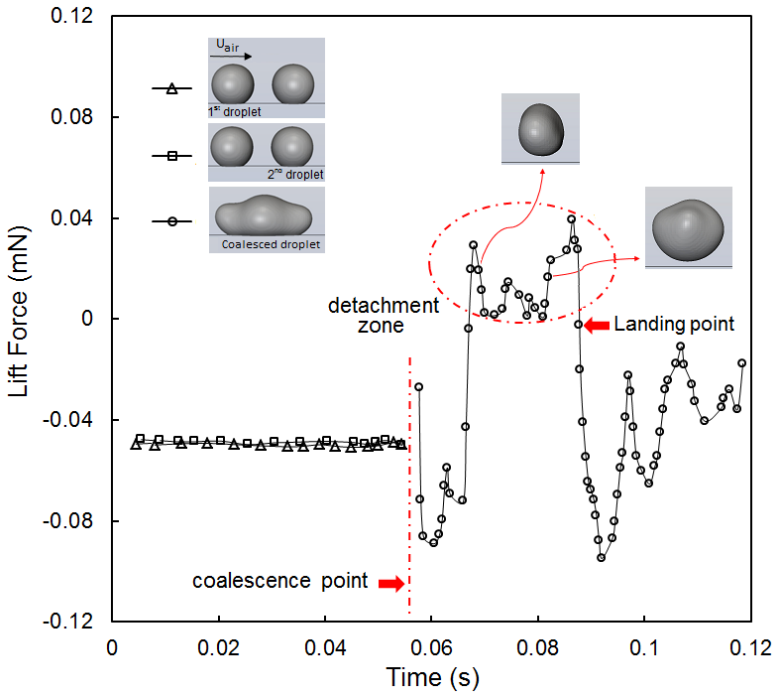

Figure 4.10 Lift force on the droplets at an air speed of 5 m/s

Droplet coalescence at high speed

Due to the importance of high speed shear flows under practical flight conditions, in this section the details of the coalescence phenomenon will be discussed when the driving force is an air speed of 90 m/s. Side and top view images of the concurrent shedding and coalescence phenomena are shown both experimentally and numerically in Figure 4.11. As it is demonstrated, the two droplets tend to move towards each other (the first droplet in the direction of the air flow and the second droplet in the opposite direction). After about 7 ms of imposing the shear flow, the two droplets touch each other, and consequently at t= 8 ms the two droplets merge completely and a larger droplet is formed. Due to the high drag force resulted from 90 m/s of air speed, the merged droplet detaches from the surface at about t=10 ms. Unlike the 5 m/s of air speed, the lift force is high enough to overcome the gravity effect, hence, the droplet easily flies away from the substrate.

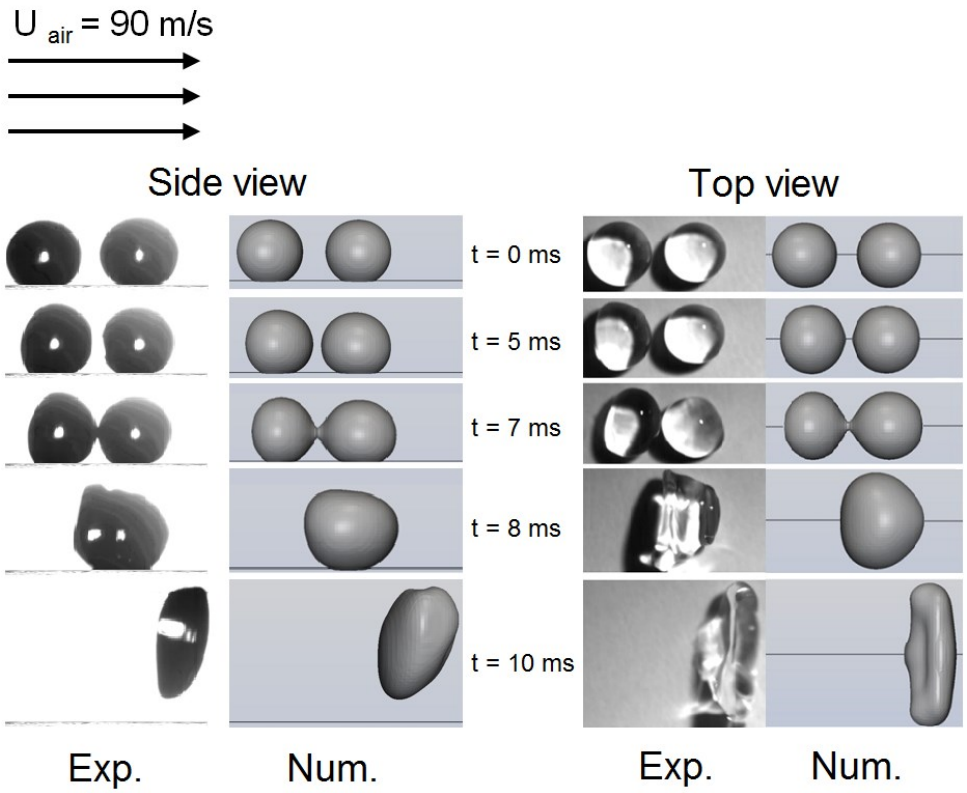

Figure 4.11 Sequences of the two droplets shedding and coalescence at an air speed of 90 m/s

The streamlines colored by the pressure over the droplets and the velocity vectors on the droplet surface during the coalescence phenomenon are shown in Figure 4.12. Similar to the low speed case, due to the presence of the separation bubble at the back of the first droplet, pressure decreases between the droplets and the second droplet moves in the opposite direction of the flow towards the first droplet (at t= 5 ms). Noting that due to higher air speed the separation zone and consequently the pressure drop is stronger in this case in comparison with the case of 5 m/s of air speed. Direction of the velocity vectors on the merged droplets (at t= 7.6 ms) proves this fact as both sides of the merged droplet move towards the merged droplet centroid. It is clearly shown in this figure that merging occurs much faster (at about 7.6 ms) comparted to the case of 5 m/s air speed (which occurs at about 55 ms). Due to the presence of high shear flow, the pressure

at the front of the merged droplet increases and leads to the droplet detachment from the substrate at about 9.5 ms.

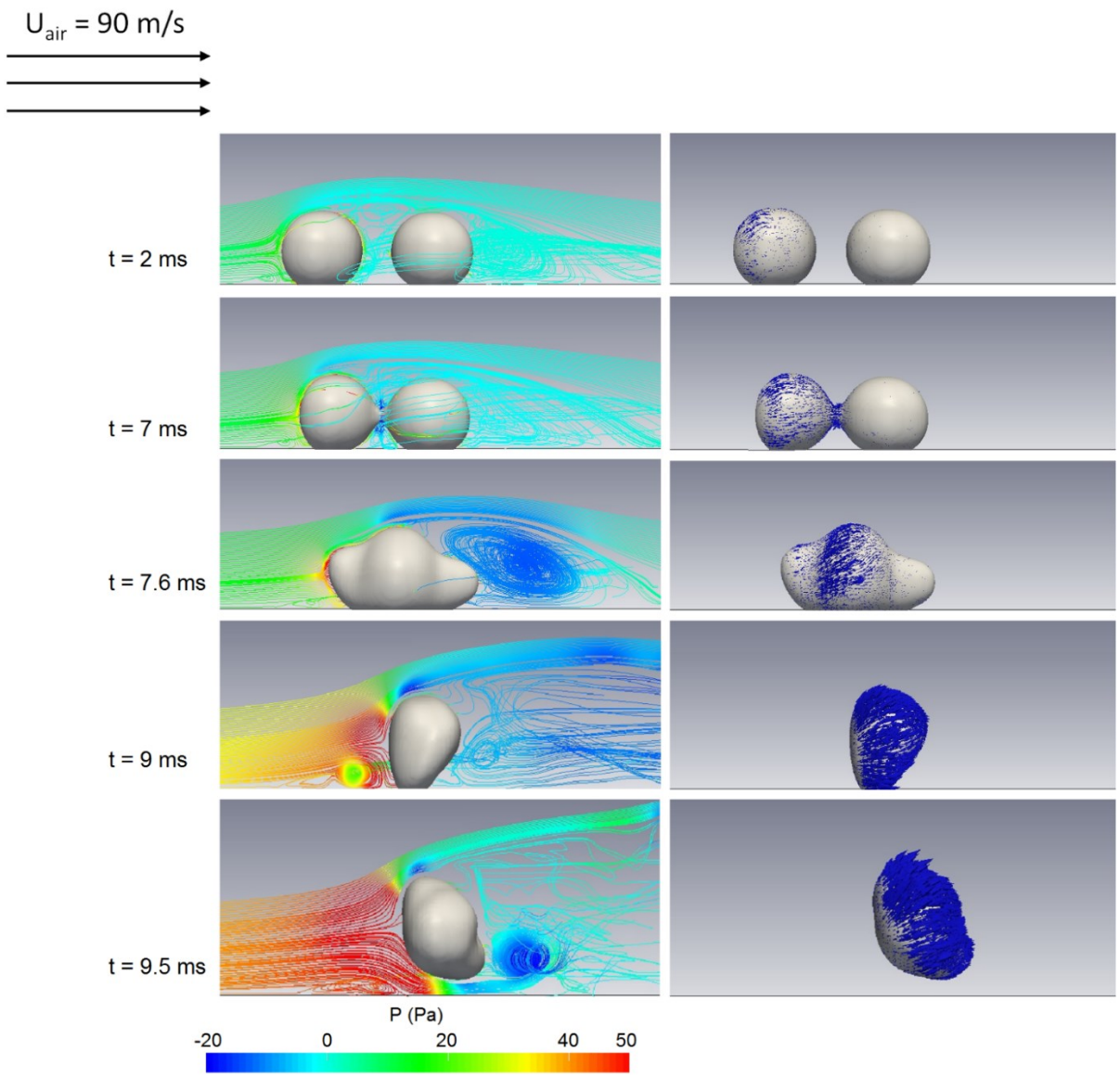

Figure 4.12 Simulation results for the coalescence of two droplets at an air speed of 90 m/s

Variations of the droplets drag force versus time for the 90 m/s is shown in Figure 4.13. As shown in Figure 4.13 the drag force on the first droplet increases slightly with time. In this stage, droplet deformation results in a higher projected surface area facing the shear flow (see top view

images at t= 5 and 7 ms in Figure 4.11). For the second droplet, the variation of drag force is not significant. As the second droplet tends to move towards the first one, the drag force gets small negative values up to the point that the two droplets merge together (t= 7.6 ms) which results in an increase of about 0.15 mN in the drag force. The increase of the drag force on the merged droplet can be explained with the same analysis used for the first droplet (i.e. deformation to an oval shape drop).

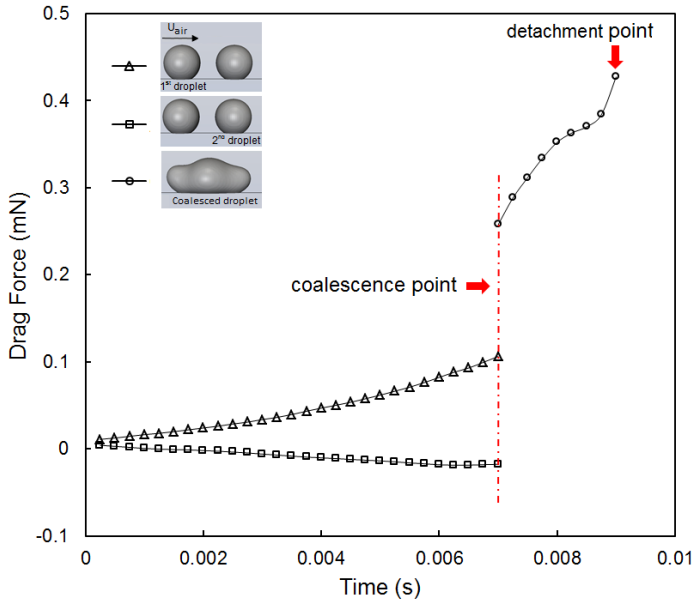

Figure 4.13 Drag force on the droplets at an air speed of 90 m/s

Similarly, variations of the lift force versus time are shown in Figure 4.14. At the earlier stages of the coalescence process the lift force has minor negative values due to the effect of high shear flow on the droplets which pushes down the top of the droplets and makes them to get an oval shape (see top view images in Figure 4.11 at t= 5 ms). For the first droplet, the lift force monotonically increases with time due to the presence of high air speed, which eventually leads to the droplet detachment from the surface. In contrary, the shear effect on the second droplet is suppressed due to the presence of the first droplet, hence there is no significant increase in the lift

force acting on the second droplet. At about 7.6 ms the droplets merge together and there will be an increase of 0.1 mN in the amount of the lift force. At t= 9.5 ms due to droplet detachment from the substrate, the lift force increases to about 0.33 mN.

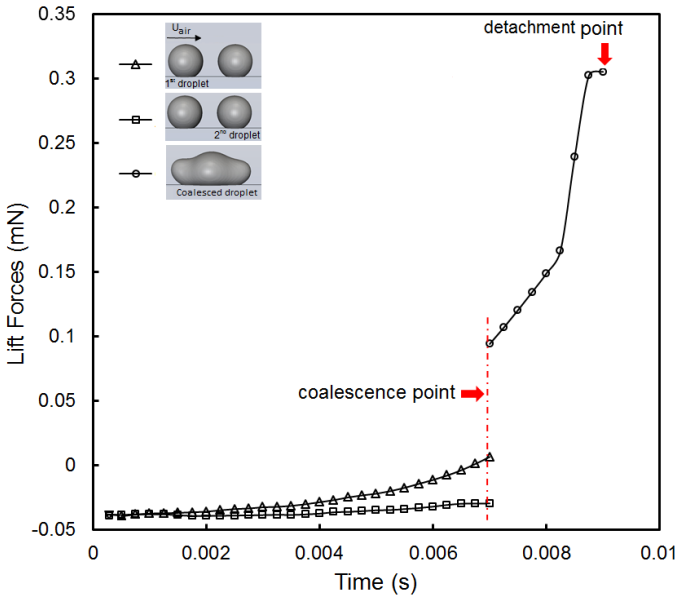

Figure 4.14 Lift force on the droplets at an air speed of 90 m/s

The same experiments were performed for the intermediate speeds of 18, 34, and 57 m/s. Since the droplet behavior for these speeds are phenomenologically the same as the case with 90 m/s, we avoid repeating the results detail here. Instead, variations of the first droplet wetting length, L_w (depicted schematically in Figure 4.5) are demonstrated for all the air speeds in Figure 4.15. It should be noted that the wetting lengths in this figure are plotted up to the point that the first droplet is merged to the second one. It is clear from the figure that for the air speed of 5 m/s the droplet does not deform and its wetting length does not change significantly with time. Increasing the air speed results in a pronounced droplet deformation to an oval shape and consequently decrease of its wetting length. As expected, the coalescence time decreases with

increasing the air speed. For example, for the air speeds of 18, 34, 57 and 90 m/s, the merging time is about 25, 13, 10 and 8 ms, respectively.

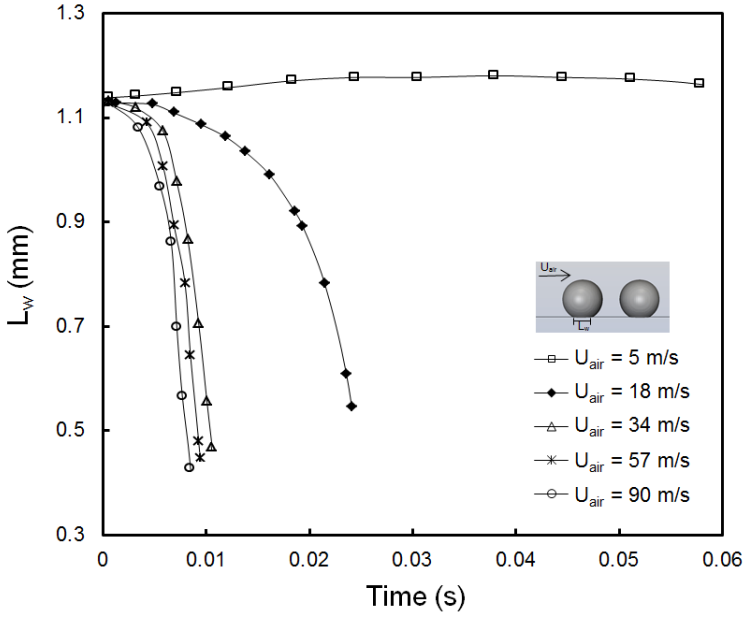

Figure 4.15 Variations of the first droplet wetting length before merging to the second droplet

As mentioned earlier, shear flow enhances the concurrent droplet shedding and coalescence on the superhydrophobic surface. It is shown in [74] that for a single droplet shedding, if the air speed is high enough (i.e. larger than 10 m/s), the droplet lifts off from the superhydrophobic surface. Analysis of the droplet detachment time from the superhydrophobic surface is an interesting phenomenon due to its significant impact on various industrial applications. For instance, decreasing the detachment time of rain droplets from an airfoil surface, decreases the amount of ice accretion. In contrast, increasing the detachment time of foliar fertilizers from superhydrophobic leafs, enhances the fertilizer's adsorption ratio. The same approach used in the work of Moghtadernejad *et al*. [74] is applied here to investigate the air speed effect on the coalesced droplet detachment time from the superhydrophobic surface. To make the analysis

easier, droplet detachment time and the air speed are nondimensionalized with t^* and the Reynolds number (Re_{air}), following the equations below.

$$t^* = \frac{t_d \mu_{air}}{\rho_{air} \pi D_{eff} Z} \quad \textbf{Equation 4.20}$$

$$Re = \frac{\rho_{air} u_{air} D_{eff}}{\mu_{air}} \quad \textbf{Equation 4.21}$$

where t_d is the detachment time of the droplet from the superhydrophobic substrate, μ_{air} and ρ_{air} are viscosity and density of air, respectively. The air velocity is denoted by u_{air}. The initial height of the droplet on the substrate is Z. The radius of the droplet after placing it on the substrate is called the effective radius, R_{eff} (see Figure 4.16) which is calculated from Equation 4.22.

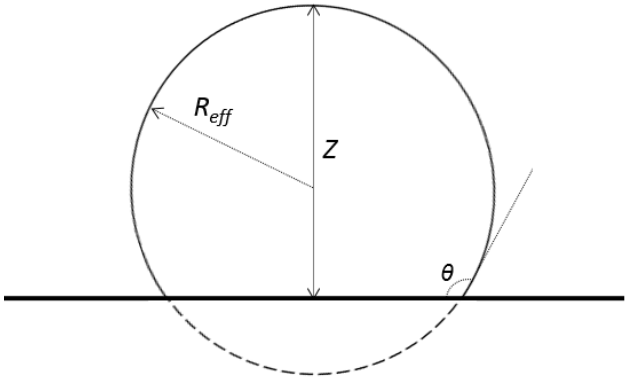

Figure 4.16 Schematic of R_{eff} and Z

$$R_{eff} = \frac{D_{eff}}{2} = R_o \left[\frac{4}{3} \times \frac{1}{\frac{2-\cos^3\theta}{3} + \cos\theta} \right]^{1/3} \quad \textbf{Equation 4.22}$$

where R_o is the initial radius of the droplet before depositing on the substrate and θ is the static contact angle of the droplet on the superhydrophobic surface.

Using the experimental data in Equations 4.20 and 4.21, variations of t^* versus Reynolds number can are plotted in Figure 4.17. In addition in this figure, dimensionless detachment time of the single droplet shedding mentioned in the authors previous work [74] versus Reynolds number is compared with the results of the case with two droplet presented in this paper.

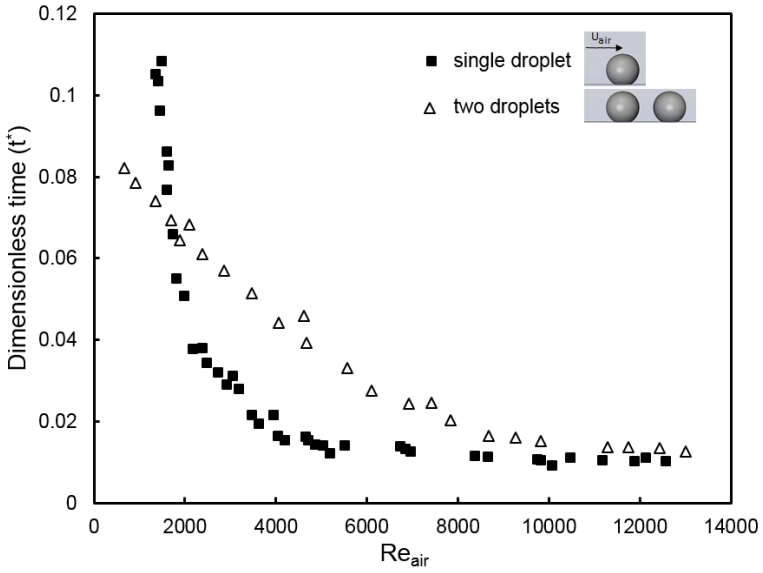

Figure 4.17 Dimensionless detachment time vs. Reynolds number

As shown in Figure 4.17 increasing the Reynolds number leads to a decrease in the detachment time of the droplet on superhydrophobic surface. Remarkably for low Reynolds numbers less than 2000, the detachment time of two merging droplets is shorter than that of a single droplet case. The reason is that due to the coalescence there is a net lift force generated which can facilitate the droplet bouncing at low Reynolds number. In contrast, for intermediate Reynolds numbers the two droplet case results in longer detachment time, because in this case the weight of the merged droplet is larger than that of the single droplet and it takes a longer time for the heavier droplet to be detached from the superhydrophobic substrate. For high Reynolds numbers (more than 10,000), the detachment time of a single and two droplet cases are nearly the same. The reason is that the effect of the additional weight is negligible in comparison with the lift force generated by the high air speed.

4.5 Summary and Conclusions

Experimental and numerical analyses were performed to investigate the effect of various air speeds ranging from 5 to 90 m/s on shedding and coalescence of two droplets on a superhydrophobic substrate. Using numerical simulations based on the VOF method coupled with LES turbulent model enables capturing the details of the streamlines, velocity vectors and aerodynamic forces during the coalescence process. It was shown that during the coalescence phenomenon the first droplet rolls on the surface towards the second one. In contrast, the second droplet moves in the opposite direction of the air flow towards the first droplet due to presence of a separation bubble at the front of the second droplet. Consequently, the two droplets merge together. For the low air speed of 5 m/s after merging the coalesced droplet detaches from the substrate however as the lift force is not high enough to overcome the gravity, it comes back to the surface. For the air speed of 90 m/s the merged droplet deforms significantly during the process and detaches from the substrate. The dimensionless detachment time of a single droplet and two droplet cases on superhydrophobic substrate was studied versus Reynolds number. It was shown that for low Reynolds numbers (i.e. less than 2000), the coalescence phenomenon assists the droplet detachment from the substrate. In contrast, for intermediate Reynolds numbers as the weight of the coalesced droplet is higher than the single droplet, the detachment time on the superhydrophobic surface is longer. Finally for higher Reynolds numbers (i.e. more than 10,000) typical of those in flight condition, the detachment time of a single and coalesced droplets are nearly the same. This work can be further extended by addressing the concurrent coalescence and freezing phenomena of the droplets with subzero temperatures.

Chapter 5

Concurrent Droplet Coalescence and Solidification on Surfaces with Various Wettabilities

"Reprinted with permission from ASME Journal of Fluids Engineering paper FE-14-1429 [92].

Abstract

Experimental study is performed to analyze the shear driven droplet shedding on cold substrates with different shear flow speeds typical of those in the flight conditions. Understanding the mechanism of simultaneous droplet shedding, coalescence and solidification is crucial to devise solutions for mitigating aircraft in-flight icing. To mimic this scenario experimental setup is designed to generate shear flow as high as 90 m/s. The droplet shedding at high speed is investigated on a cold surface (0 and -5 °C) of different wettabilities ranging from hydrophilic to superhydrophobic. Result analyses indicate that on a hydrophilic substrate, the droplets form a rivulet which then freezes on the cold plate. In contrast, on the superhydrophobic surface, there is no rivulet formation. Instead, droplets roll over the substrate and detach from it under the effect of high shear flow.

5.1 Introduction

Sessile droplet movement under the effect of shear flow is called shedding and only happens when the shear flow overcomes the droplet adhesion to the substrate. Following the incipient motion, which corresponds to the start of the droplet shedding, the droplet moves downstream along the surface [44]. On a cold surface, droplet shedding behavior is a complex problem coupling hydrodynamic, heat transfer and phase change which depends on different parameters such as the droplet size, contact angle, contact angle hysteresis, surface tension, as well as air shear speed.

There exists a variety of circumstances in which droplet shedding and coalescence plays crucial role such as in ink-jet printing, spray coatings, thermal spray deposition process, microfluidics devices and icing phenomenon that occurs on wind-turbine blades, power lines and airfoils during flight [31, 43, 93-97]. In the present study the air shear speed which is the driving force for the shedding varies from 5 to 90 m/s and the droplets are placed on a cold substrate, as a result the outcome of this work can be of practical interest for ice accumulations, *e.g.* on airfoils or wind-turbines, where droplets are under the effect of high speed air. In the mentioned applications due to wind shear effect, the rain droplets start to move along the surface after impact. Generally on surfaces with high wettability, narrow streams of liquid known as rivulets form due to the run back flow of the droplets. The spreading flow of rivulet highly depends on the surface wettability and the air shear speed. Rivulets and droplets will be frozen when the ambient temperature is below the water freezing point which results in significant negative impacts on the performance of various components. For example during in-flight condition, due to the ice accumulation on the airfoil, the aerodynamic efficiency of the airplane significantly reduces by increasing drag and decreasing lift forces [5, 6, 94, 98, 99]. Recently, few studies

have shown that ice formation can be considerably decreased if the surface of the airfoil is water repellent or of low surface energy. For instance, in the work of Antonini *et al*. [71], it was shown that using a superhydrophobic coating on airfoil can reduce the amount of accreted ice due to low water adhesion on these surfaces. Hence, the amount of power required to remove ice from a superhydrophobic surface is significantly reduced in comparison with an uncoated hydrophilic surface. Boinovich *et al.* [72] studied the nucleation kinetics of super-cooled water droplets on surfaces with various wettabilities. They showed that at subzero temperatures and saturated water vapor atmosphere, superhydrophobic surfaces show a significant delay in ice formation in comparison with the hydrophilic and hydrophobic surfaces [72].

Study of droplet behavior on superhydrophobic surfaces is an active research topic due to the high water repellency characteristics of these surfaces. However, there are limited insights into fundamentals of air shear driven drop shedding in literature especially on superhydrophobic substrates. Milne and Amirfazli [44] studied the droplet incipient motion due to shear flow at rather low speed flows (i.e. below 30 m/s) on surfaces with different wettabilities. Recently Moghtadernejad *et al*. [74] studied the shear driven behavior of droplets on various surface morphologies under the effect of high shear flow (up to 90 m/s) which is close to speeds of interest in aerospace applications. However, in both [44] and [74], the studies were performed on substrates at room temperature. In the present work the icing phenomenon on one and two droplets under the effect of different shear speeds is investigated experimentally. In the following experimental study, different range of air shear speeds from 5 to 90 m/s is used on both hydrophilic and superhydrophobic surfaces. To capture the icing phenomenon these substrates are cooled down to as low as -5 °C. Except the air shear speed and surface wettability, all other

parameters such as droplet position, size, temperature and humidity are kept constant in the experimental procedure.

5.2 Experimental Setup

The experimental setup is designed to capture the icing behavior of sessile droplets while facing air shear flow. As the shedding time is of the order of micro seconds, a Photron SA1.1 high speed camera (Photron, California USA) operating at 5400 frames/s with an UltraZoom 6000 lens (Navitar, New York USA) was used to capture the phenomena throughout the experiments. The backlight method of shadowgraphy was applied by using LED light (Schott, California USA) to capture the simultaneous shedding and icing progression within the droplet. Experiments were performed on two rectangular plates with a size of 150×75×2 mm^3. The first substrate is a polished aluminum with a contact angle of 75° which makes it hydrophilic. However, before performing the tests the surface was cleaned with acetone and distilled water several times and dried for 15 minutes.

The second surface that acts as a superhydrophobic with a contact angle of 155°± 1, is a polished aluminum plate coated with WX2100 spray (Cytonix, Maryland, USA). The SEM image of the WX2100 surface with the 2500X magnification is shown in Figure 5.1. To prepare this surface after cleaning the polished aluminum sample with the procedure described above, the surface was sprayed with WX2100 three times. However, before the second and the third coats the substrates were dried for 5 hours. The samples were then fixed on a cold plate (WATRONIX Inc., CA, USA) that decreases the substrates temperature to -5 °C. To measure the surface temperature a FLIR A320 infrared camera (ThermoVision$^{TM.}$, Sweden) along with a 30 mm IR lens was used. To make the surface temperature measurement more accurate, a thermocouple

was used to measure the surface temperature exactly at the point that droplet was placed. The infrared camera was calibrated based on the temperature measured by the thermocouple.

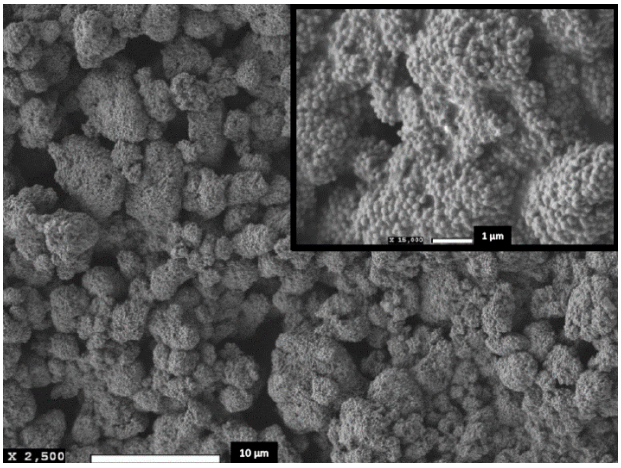

Figure 5.1 SEM image of the WX2100 substrate with 2500X magnification. The specified area at the top right corner has the magnification of 15000X

A high pressure tank was utilized to create the shear flow. Dry air was introduced on the substrate from the tank by using the tube with the length and inlet diameter of 800 and 10 mm, respectively. The tube was attached to the substrate leading edge. The air speed was controlled with a high pressure valve and can vary between 5 and 90 m/s. This is the air speed that was measured with a pitot tube at the droplet position. Distilled water droplets were deposited on the surface from a small container of ice and water (Temperature 0.5± 0.2 °C) with a sterilized micro pipette (Sartorius, IL, USA). The droplet was deposited at 10 mm away from the leading edge of the substrate as shown in Figure 5.2. The reason to choose 10 mm away from the substrate leading edge, was that air stream is smooth and without any significant vortices at and after this location.

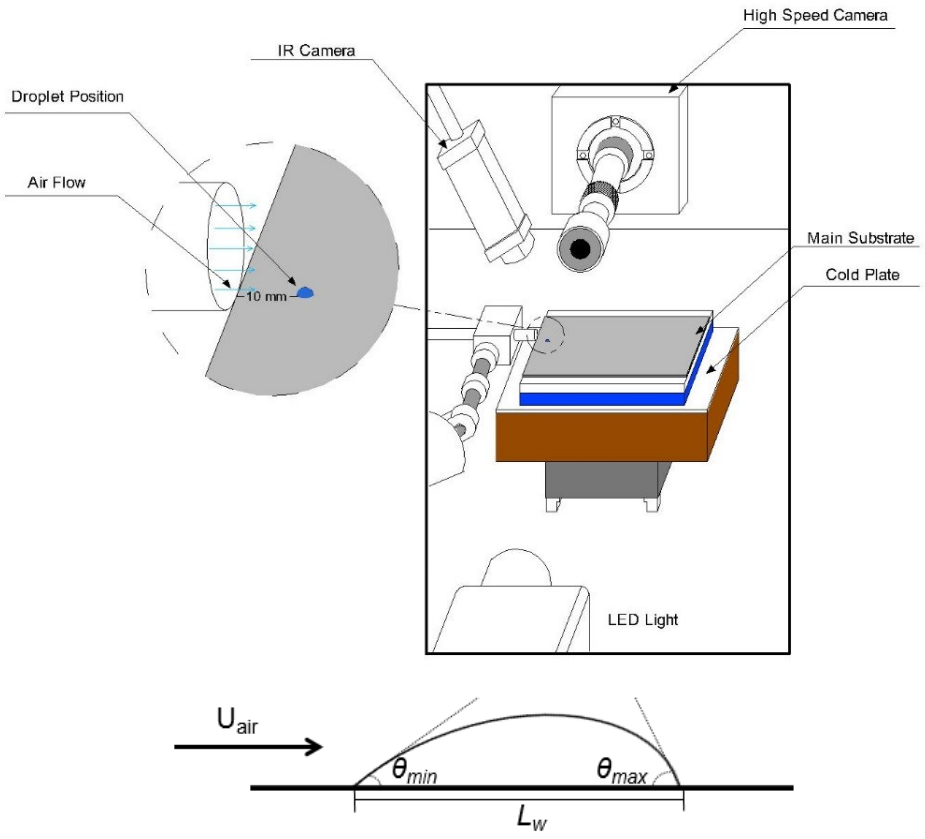

Figure 5.2 Experimental setup

It is worth noting that in practical in-flight icing, the numbers of the droplets is more than one, and due to the air shear effect droplets coalescence occurs. As a result, in this study in addition to a single droplet, two coalescing droplets behavior is investigated as well. To account for the effect of droplet coalescence, the same experiments were performed by adding a second droplet at about 1 mm distance from the first one (shown in Figure 5.3). The droplet volume for each test was 5 µl which corresponds to a spherical drop with about 2.1 mm diameter. The air was flowing on the substrate right after placing the droplets on the substrate. Each test was repeated at least fifteen times to reach an acceptable degree of accuracy. The reported results are the ensemble average of these fifteen experiments for each case. ImageJ software [78] was used for post-processing the results in this work. The test setup is schematically shown in Figure 5.2. To see the effect of surface temperature the tests were performed on the substrates at

temperatures of 0 and -5 °C. However, the surrounding temperature and relative humidity during the test were constant and about 22 °C and 40% respectively. The details of the test matrix and surface characteristics are given in Table 5.1. It should be mentioned that the contact angle hysteresis defined in Table 5.1 is calculated based on the method that Milne and Amirfazli [44] proposed in their study. They mentioned that while dealing with shedding of droplets, it is more meaningful to use the difference between the maximum contact angle (θ_{max}) and the minimum contact angle (θ_{min}) instead of the traditional method of hysteresis measurement which is based on the difference between the advancing and receding contact angles. θ_{max} and θ_{min} refer to the droplet angles downstream and upstream of the flow, respectively for the case of shear driven shedding.

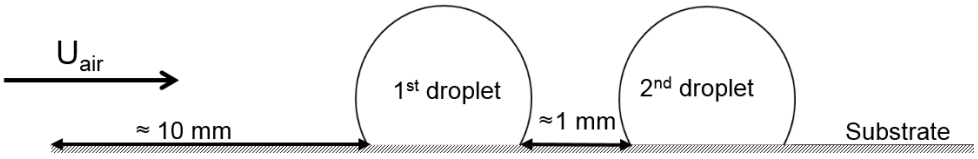

Figure 5.3 Schematic of the two droplets position on the substrate

Table 5.1 Test Matrix

Surface Material	Aluminum		WX2100
Contact Angle (°)	75±1		155±1
Contact Angle Hysteresis (°)	18±2		8±2
Shear Speed (m/s)	5±2	34±2	90±2

5.3 Results and Discussion

As mentioned above, the experiments in this paper were performed at surface temperatures of about 0 and -5 °C with one and two droplets to analysis the behavior of water droplets on aluminum and superhydrophobic substrates under the effect of air shear flow. The air flow speed which is the driving force of droplet movement varies from 5 to 90 m/s. To probe the droplet

behavior during shedding, the wetting length of the droplet on the substrate (L_w) is experimentally measured by image processing. Variation of the wetting length is dependent on contact angle, contact angle hysteresis, droplet size and the air shear speed. As the effect of surface wettability and the air shear speed together with the surface temperature are the main focus of this study, the size of the droplets were kept constant (5 µl) in all the tests. To observe the effect of surface wettability, shear speed and surface temperature separately, only one of the three mentioned parameters is changed during one set of the experiments. In Figure 5.3 the side view images of the droplet shedding on the aluminum substrate taken by the high speed camera are shown at different air speeds.

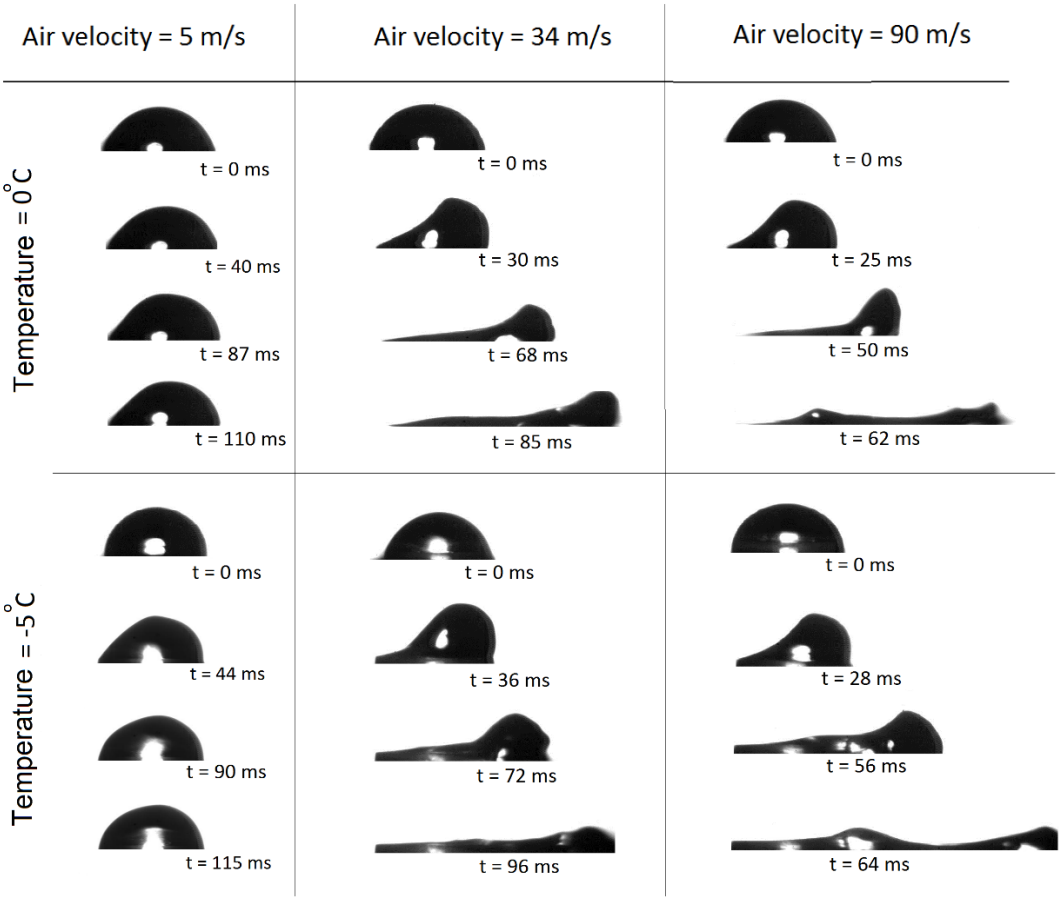

Figure 5.4 Single droplet shedding sequences on the aluminum substrate; Air flow direction is from left to right

As shown in Figure 5.3, for an air speed of 5 m/s at both temperatures (0 and -5 °C) the droplet only oscillates on the substrate. However, by increasing the air speed to 34 and 90 m/s, rivulets form on the substrate. Another interesting phenomenon that can be seen in Figure 5.3 is the formation of ice on the surface at -5 °C. Droplet starts to freeze from the bottom with a freezing front moving upwards. However, due to the presentence of the air flow, unlike the case of water droplet freezing in still air configuration [100, 101], no pointy tip is observed especially at high shear speeds. The top part of the droplet which is not frozen starts to shed and form a rivulet at higher air speeds (i.e. 34 and 90 m/s). It is worth mentioning that the trailing edge of the rivulet forms on the base of the droplet which is already frozen and continues its runback flow on the surface. Due to the low temperature of the surface some parts of the rivulet freeze while flowing on the substrate. It should be mentioned that the truncated area in last sequences of rivulet formation are due to rivulets flow out of the cameras field of vision.

To understand the droplet shedding behavior in detail the variations of the droplet wetting length, L_w, during time was analyzed based on the dimensionless analysis. To so, the wetting length of the droplet (shown in Figure 5.2) was normalized based on the effective diameter, D_{eff}, of the truncated sphere which represents this sessile droplet (see Figure 5.5) with the below ratio;

$$L^* = \frac{L_w}{D_{eff}} \qquad \textbf{Equation 5.1}$$

The value of D_{eff} on the hydrophilic substrate is calculated from the below equation;

$$D_{eff} = 2\,R_{eff} = 2R_o \left[\frac{4}{3} \times \frac{1}{\frac{2+cos^3\,\theta}{3} - cos\,\theta}\right]^{1/3} \qquad \textbf{Equation 5.2}$$

where R_o is the initial radius and θ is the static contact angle of the droplet on the hydrophilic surface. Time was also nondimensionalized by the following equation;

$$t^* = \frac{t\mu_{air}}{2\rho_{air}\pi R_{eff} Z} \qquad \textbf{Equation 5.3}$$

where t is the time, μair and ρair are viscosity and density of air respectively. Z is the height of the sessile droplet as is depicted in Figure 5.5.

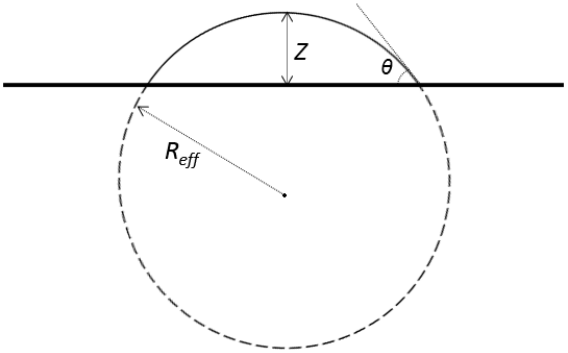

Figure 5.5 Schematic of R_{eff} and Z of a droplet placed on aluminum substrate

In Figure 5.6, the variation of the droplet normalized wetting length (L^*) versus dimensionless time, t^*, together with surface temperature and air shear speed is shown. The result of this work is compared with authors previous paper [74] that was performed at room temperature (22 °C). In Figure 5.4, it is shown that the wetting length of the droplet on the aluminum surface increases by the increase of shear flow speed. For air speeds of 34 and 90 m/s due to the high drag force and surface wettability a narrow stream of water (i.e. rivulet) forms on the plate which significantly increases the wetting length, L_w; unlike the case of low air speed (5 m/s) where the drag force on the droplet is not high enough for rivulet formation. With low air speed (5 m/s), the droplet only vibrates at its place, consequently the wetting length does not vary significantly with time.

In addition, the effect of surface temperature on the droplet wetting length is demonstrated in Figure 5.6. When the surface temperature is lower, due to frost layer formation on the cold substrate, the change in the droplets physical properties and the advancement of the ice front within the droplet, the adhesion of the droplet on the substrate increases. As a result at a fixed

time and with the same air speed, the length of the rivulet decreases with temperature. However, the decrease in rivulet length is more obvious for intermediate speed (34 m/s). The reason is that at low speed (5 m/s) there is no rivulet formation. In addition at the high speed case (90 m/s), the drag force is so high that it can overcome the small increase of droplet adhesion due to presence of the cold substrate; hence the difference between the wetting lengths under the effect of 90 m/s of air is less than 34 m/s.

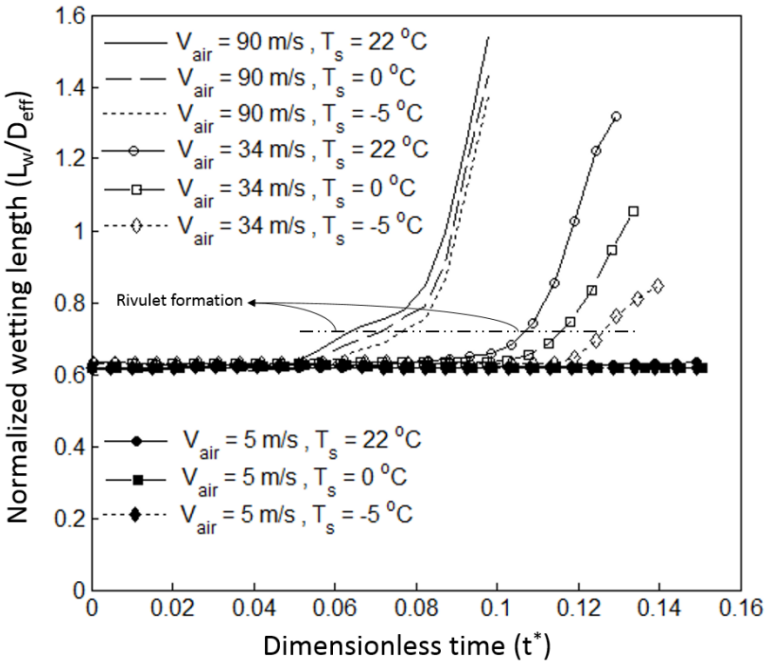

Figure 5.6 Normalized wetting length vs. dimensionless time on the aluminum substrate at different surface temperatures

The same phenomenon happens when there are two droplets on the surface, as shown in Figure 5.7. Due to the air shear flow the droplets coalesce first and after that the merged droplets start to propagate on the surface and form a rivulet. By decreasing the temperature of the substrate as in the single droplet case, ice starts to grow at the bottom of the droplets; and before reaching to the droplet top, due to the shear flow effect, the top parts of the droplets which are still liquid, merge together and then flow on the surface (i.e. rivulet formation).

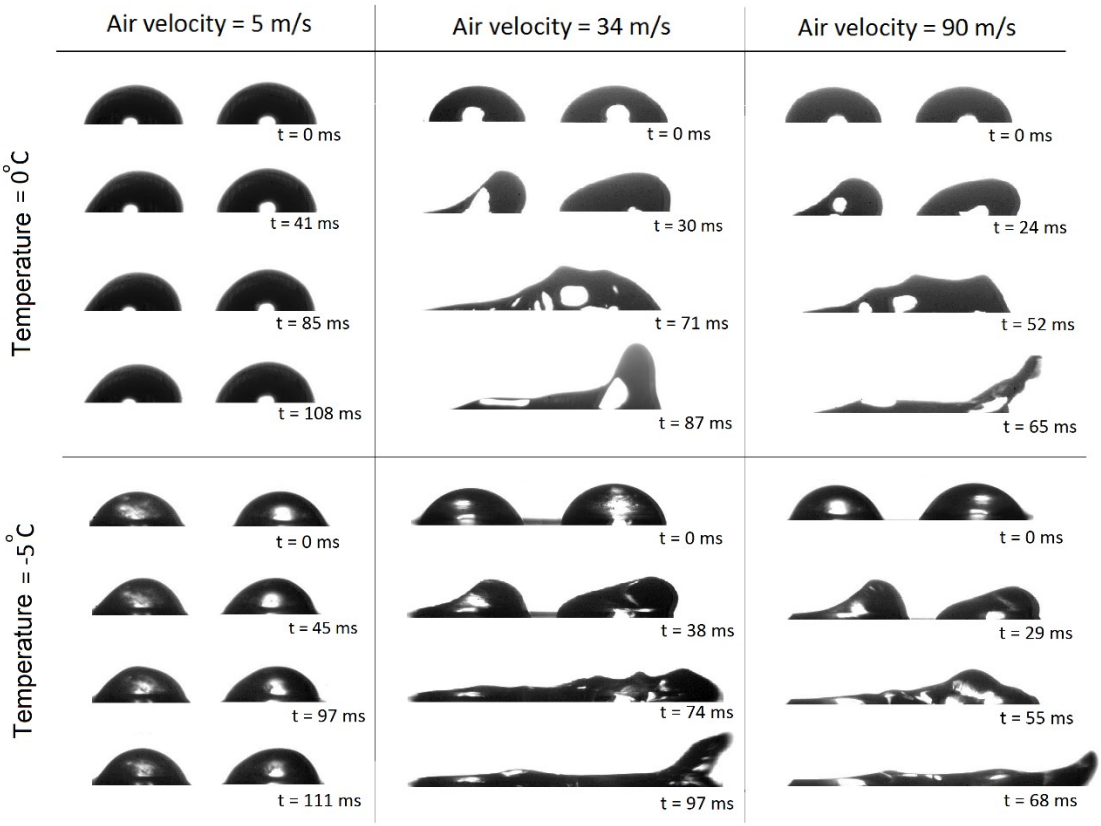

Figure 5.7 Two droplets shedding sequences on the aluminum substrate; Air flow direction is from left to right

To study the effect of surface wettability, the same experiments are performed on a superhydrophobic surface on which the water droplet static contact angle is about 155° at room temperature. As a result of low adhesion and water repellency characteristics, superhydrophobic surfaces are good alternative candidate as coatings for anti-icing and di-icing purposes. The reason is that using superhydrophobic coatings on aerodynamic and structural surfaces enhances the effect of the standard anti/di- icing systems and also reduces the amount of energy consumptions required for the current systems [71]. However, there are some limitations of using superhydrophobic surfaces in wet and cold environments. In 2012 Jung *et al.* [81] used both experiments and the nucleation theory to confirm that the flow of the surrounding gas and

humidity are important factors that can affect the icephobic characteristic of a surface. The authors also studied the effect of evaporation from a super-cooled water droplet on icephobic behavior of the surfaces [102]. Farhadi *et al.* [103] compared wet and dry superhydrophobic samples and found out that contact angle (CA) of a wet superhydrophobic surface decreases and its contact angle hysteresis (CAH) increases which makes the surface hydrophobic and therefore sticky for water droplet. Their finding was in good agreement with the work of other researchers who reported that wet surfaces cause significant deterioration on the properties of superhydrophobic surfaces [70, 81, 102-108]. In [109-111] it was also shown that if the samples are repeatedly iced/shed the superhydrophobic characteristics will deteriorate as a consequence of the damage on the substrate microstructure roughness. Hence the wetting regime will switch from pure Cassie (high CA and low CAH) to mixed Wenzel-Cassie (low CA and high CAH). Ensikat *et al.* [112] confirmed the above phenomena by showing that the rough surface asperities get indented to the liquid and will be damaged during solidification.

Our observation with WX2100 as a superhydrophobic coating on aluminum surface proves the same phenomenon about the effect of cold temperature on the superhydrophobic coatings. At room temperature of 22 °C, the static contact angle of a droplet on the superhydrophobic surface is 155°. However, by setting the surface temperature to 0 and -5 °C due to formation of frost layer on the substrate, the contact angle decreases to about 148° and 138°, respectively. As a result although the surface is still hydrophobic however the droplet stickiness to the surface increases. The sequences of the droplet shedding on superhydrophobic surface are shown in Figure 5.8. It can be seen that despite the existence of frost layer at subzero temperatures, the surface still has its water repellency characteristics. Comparing results of Figure 5.8 with the ones in Figure 5.4, indicates that due to the low adhesion of the droplets on superhydrophobic

surfaces no rivulet forms on the superhydrophobic substrate; instead, at a low speed of 5 m/s the droplets roll over the surface with no deformation. Consequently under the effect of high air shear flow (34 and 90 m/s) the droplet deforms and finally detaches from the substrate. Hence, unlike the aluminum case, even when the surface temperature is -5 °C no significant ice formation can be observed on the superhydrophobic surface during the droplet shedding.

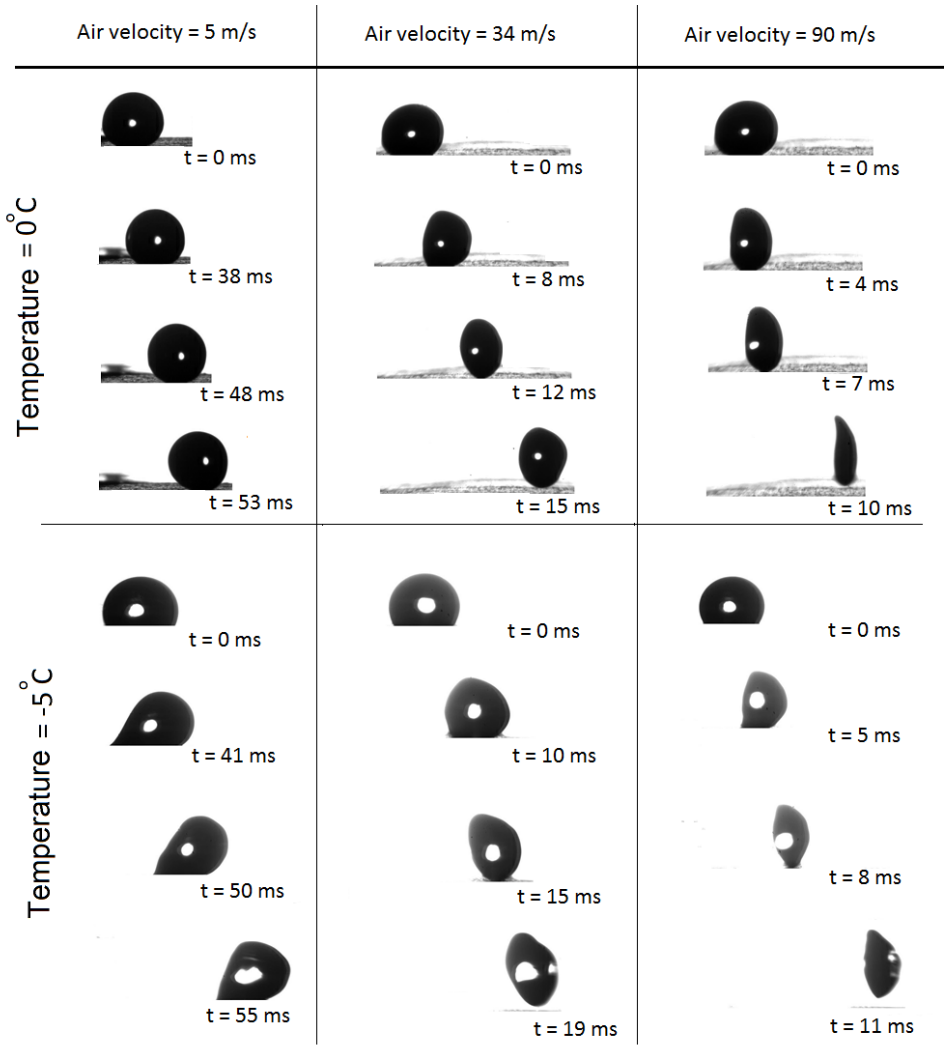

Figure 5.8 Single droplet shedding sequences on the superhydrophobic substrate; Air flow direction is from left to right

The mentioned phenomenon can be also observed in Figure 5.9 by comparing the normalized detachment time of the droplet at room temperature from the previous work of the

authors [74], with the cold substrates of the current study (0 and -5 °C). It should be noted that the air flow speed remains constant in all the experiments. Noting that to plot Figure 5.9 the same procedure mentioned for the aluminum substrate, was used for normalizing wetting length and time. Except that as the surface here is superhydrophobic (see Figure 10) its effective radius is derived from the following equation;

$$D_{eff} = 2\,R_{eff} = 2R_o \left[\frac{4}{3} \times \frac{1}{\frac{2-cos^3\,\theta}{3} + cos\,\theta}\right]^{1/3} \qquad \textbf{Equation 5.4}$$

It is clear from Figure 5.9 that for the low speed case of 5 m/s that the droplet only rolls on the superhydrophobic surface, due to the higher adhesion of the droplet when the surface temperature is 0 and -5 °C, the wetting length of the droplet on the surface is more than that at room temperature.

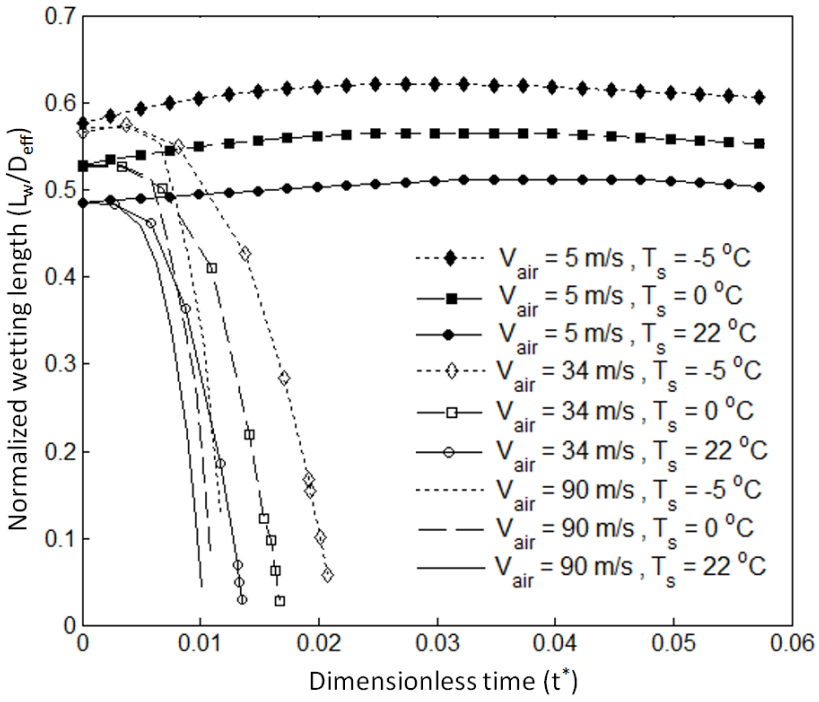

Figure 5.9 Normalized wetting length vs. dimensionless time on the superhydrophobic substrate at different surface temperatures

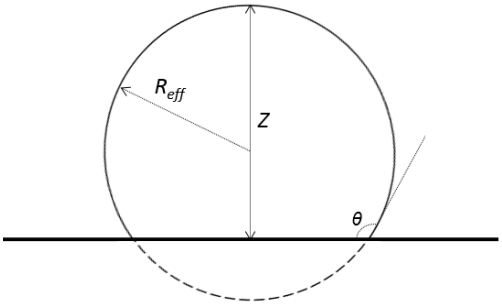

Figure 5.10 Schematic of R_{eff} and Z of a droplet placed on the superhydrophobic substrate

For higher shear speeds of 34 and 90 m/s it can be noted that the deformation and detachment of the droplets happen slower on surfaces with lower temperature in comparison with the case at room temperature. However, it is worth noting that in order to prevent the surface damage due to repeated iced/shed phenomena, in this work after each test on the superhydrophobic plate, the sample is replaced by a new one.

The droplet contact time and the air flow speed are nondimensionalized by introducing a dimensionless time and Reynolds number based on the effective droplet diameter as described in [74]. It should be noted that to make the time dimensionless, Equation 5.3 is used except that the time (t) here, is the droplet detachment time from the superhydrophobic plate which is taken from the experiments. The Reynolds number is as follows;

$$Re = \frac{2\rho_{air} u_{air} R_{eff}}{\mu_{air}} \qquad \textbf{Equation 5.5}$$

where u_{air} is the air speed.

Figure 5.11 is a good demonstration for the effect of surface temperature and air shear speed on droplet detachment time on superhydrophobic surface. As is shown in Figure 5.11, increasing the Reynolds number decreases the droplet detachment time. However, decreasing the surface temperature deteriorate the detachment phenomenon. In other words, with a constant air shear

speed, decreasing the surface temperature results in higher detachment time mainly due to ice formation.

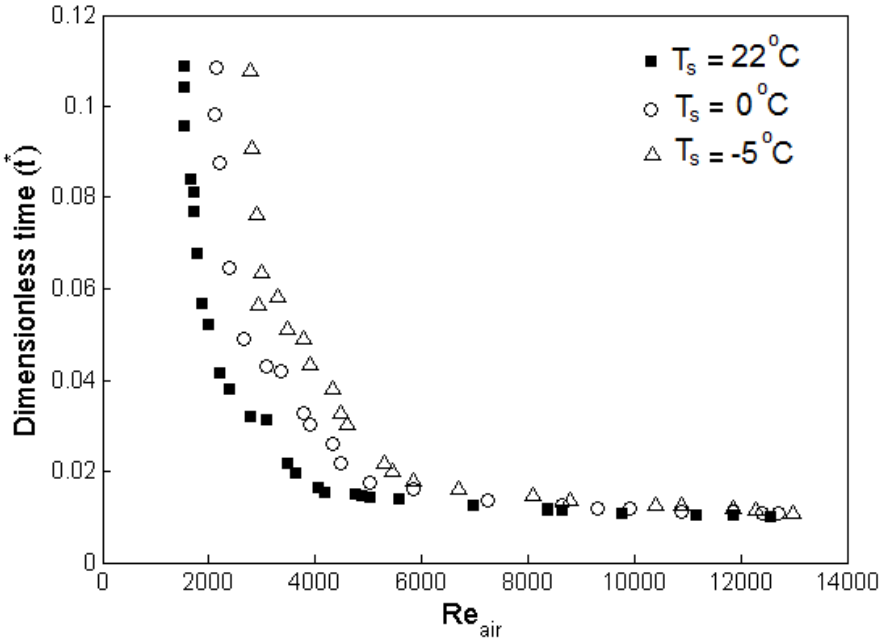

Figure 5.11 Dimensionless detachment time vs. Reynolds number on the superhydrophobic substrate

The same phenomenon is observed with two droplets on the superhydrophobic substrate as is shown in Figure 5.12. The droplets merged together due to the effect of air flow; the coalescing droplets then rolls on the surface when the air speed is 5 m/s. Increasing the shear flow results in deformation and detachment of the merged droplets from the substrate. Similar to the single droplet case, no significant ice is accumulated on the substrate even when the surface temperature is lowered to -5 °C.

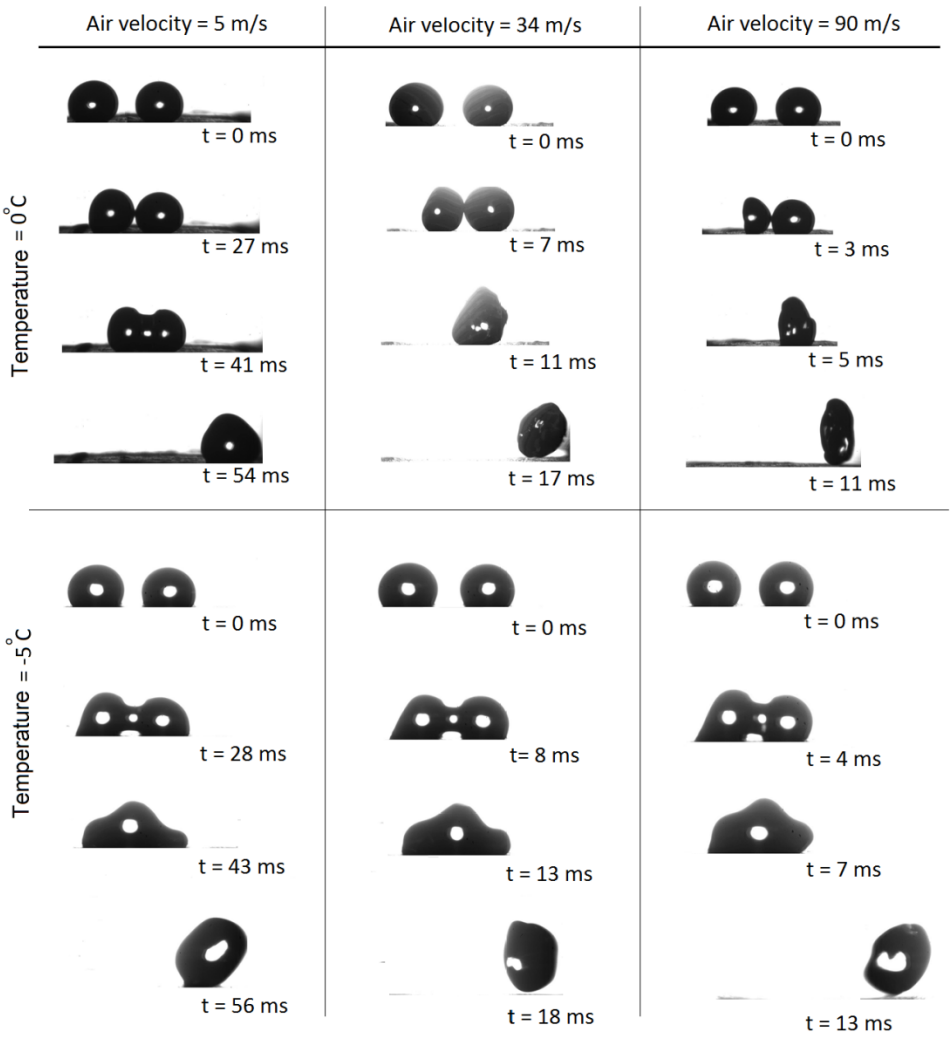

Figure 5.12 Two droplets shedding sequences on the superhydrophobic substrate; Air flow direction is from left to right

5.4 Summary and Conclusions

The shear driven shedding behavior of a single and two coalescing droplets are investigated on cold hydrophilic and superhydrophobic surfaces. It is known that when the shear flow is high enough the droplet forms a rivulet while moving on the hydrophilic surface. The rivulet then freezes on the cold plate. Increasing the air speed enhances the rivulet wetting length and consequently the ice accumulated area. In contrast, on superhydrophobic surfaces there is no

rivulet formation. Instead, with high shear speeds the droplets deform and subsequently detach from the surface. As a result, no ice accumulation is observed on the superhydrophobic surface in high speed camera's field of vision. The droplet detachment phenomenon on superhydrophobic substrate is analyzed based on the contact time of the droplet on the surface and the air shear speed. It is shown that the contact time of the droplet on the superhydrophobic substrate decreases by increasing the air shear speed. The effect of frost layer formation on diminishing superhydrophobicity of the surfaces has also been investigated in this study. It is shown that due to formation of frost layer at subzero temperatures (with constant air speed), the droplet detachment time from superhydrophobic surface increases in comparison with the results taken at room temperature. Although frost layer may deteriorate the superhydrophobicity of the coatings, these surfaces can still be an ideal candidate for anti-icing purposes as the amount of ice accretion is low in comparison with hydrophilic surfaces. Finally, the outcome of this work is of utmost importance in understanding the effect of surface properties and shear speed on droplets coalescence and freezing. This study can further be extended to lower temperatures, i.e. as low as -20 °C, for both the droplet (supercooled) and the substrate. The effect of the droplet size can be also added to the study to explore the concurrent shedding and freezing phenomena.

Chapter 6

Experimental and Numerical Analysis of Rivulet Dynamics on Surfaces with Various Wettabilities

Abstract

Ice formation leads to significant decrease of aircraft performance and possible disasters. When rain droplets accumulate on aircraft wings, they form narrow films of water known as rivulets. Due to air shear effects, rivulets generate runback flow on the airfoil, enhancing ice formation. Understanding the dynamics of rivulets is necessary in solving the ice formation problems on airfoils. In this paper we report the results of an experimental study together with numerical simulation of the dynamics of narrow water films i.e. rivulets under the effect of various air shear speeds and different surface morphologies ranging from hydrophilic to superhydrophobic.

6.1 Introduction

A narrow stream of liquid falling down a solid substrate is called a rivulet. A good example of a rivulet is the water stream on windowpanes during a rainy day. Rivulets can have different patterns based on their flow rate [58]. A rivulet starts with a sequence of droplets that merge into

a linear straight narrow film. At higher flow rates a rivulet starts meandering with instability at its interface with air [56]. Increase in flow rates leads to the formation of turbulent oscillating rivulets [56]. Rivulet flows depend on a number of parameters among them flow velocity, the temperature and the morphology of the surface on which the rivulet is moving.

Rivulet dynamics is involved in different scientific problems and industrial applications such as production of microchips, the flow of surface active materials in chemistry [57] and rain flow on structural systems in aerospace industry [6]. Rivulet dynamics is particularly important in aerospace industry. When rain droplets hit the airfoil surface during aircraft flight, wind shear effects turn them into rivulets. At temperatures lower than water freezing point, the generated rivulets turn into ice on the airfoil surface. Ice accretion on the wing increases with propagation and runback flow of rivulets on the surface and results in significant decrease in the performance of aircraft [6]. Preventing ice formation over the airfoil or removing it after its formation is crucial for flight safety. In other words, developing better de-icing or anti-icing systems for aircrafts is a critical task for aerospace industry [6].

One of the first steps in understanding in-flight icing problem is the study of rivulets dynamics. Mathematical description of rivulet dynamics is completed due to the existence of free boundary interfaces which must be determined as a part of the governing equation solution. The problem becomes even harder if the film unit depth goes to zero, because linearized equations will not be sufficient to study the phenomenon. Thus, nonlinear film disturbances must be taken into consideration. Lubrication theory or long-wave-theory is one of the methods to study thin film flow on a solid surface. In this method, the governing equations and boundary conditions are simplified to a system that usually contains a single nonlinear partial differential equation that is formulated in terms of the local film thickness [61] . Other unknowns such as fluid

temperature and velocity are determined by functional solution of the initial differential equation. In this case the free boundary complication can be eliminated from the system [62]. Marshall and Ettema [63] used lubrication approximation in their experiments with low Reynolds number to investigate the effect of gravity and shear flow on rivulets. The authors showed that for low speed shear flows (less than 5 m/s) shear driven flow and gravity effects have nearly the same influence on rivulets behavior. However, at high sheer speeds of 10 m/s there is a large difference between the flows driven by wind shear and the flow of rivulets under the effect of gravity. In addition in the latter case, they presented that the effect of microgravity and terrestrial gravity is also considerably different in rivulet flow.

As mentioned before, surface morphology is one of the factors that should be taken into consideration while studying rivulets behavior. Gajewski [64, 65] conducted experiments with rivulets on three different surfaces: aluminum, copper and Brass while heating [64] and cooling [65] these surfaces. It was shown that lowering the temperature improves the hydrophilic behavior of the metal surface, thus, the rivulet width increases. In addition when the number of electrons on the last metal shell is higher, the metal shows more hydrophilic properties [65]. This is the reason that the worst wetting property is for copper, the rivulet is the narrowest on this plate and the contact angle is the highest. In contrast, among these metals the best wetted surface is aluminum, it has the widest rivulet flow and the contact angle is the lowest on this plate [65] .

Simulation of thin film flow patterns, flowing down inclined and horizontal planes was performed by Diez *et al*. [57, 66]. Their model has the capability to show the effect of capillary force and fluid-solid interactions for analyzing the rivulets wave lengths. Daerr *et al*. [67] found that the fluid inertia is the main cause of meandering behavior while doing theoretical work on rivulets stability. Saber *et al*. [68] obtained analytical results for rivulet thickness, wetting rate at

break up by using the idea that total energy of the stable rivulet would be minimized after the break up process. Their analysis was performed by assuming the fluid flowing down or climbing on a vertical or inclined surface while the surface was subjected to the interfacial shear flow.

Up to now a complete understanding of rivulet dynamics especially under the effect of different surface wettabilities has not yet been achieved. Being able to predict the rivulet behavior under the effect of these two important parameters is of utmost importance for understanding the underlying physics of rivulet dynamics under practical conditions, i.e. in-flight icing. This paper consists of experimental and numerical analysis of the dynamics of thin film flow under the effect of different air shear speeds and various surface wettabilities.

6.2 Experimental Setup

The experimental setup is designed to capture the dynamics of a rivulet while facing air shear flow. To capture the flow patterns precisely, a Photron SA1.1 high speed camera (Photron, California USA) operating at 2000 frames/s with an UltraZoom 6000 lens (Navitar, New York USA) was used to capture the phenomena throughout the experiments. The backlight method of shadowgraphy was applied by using an LED light (Schott, California USA) to capture the movement of water streams. In order to create uniform shear flow, experiments were performed inside a closed-loop wind tunnel. The wind tunnel consists of a fan that turns with 1710 rpm and enables the generation of air shear flow. An Acs141 controller (ABB, Zurich, Switzerland) was used to change the shear speed which varies between 1 to 20 m/s. The test section of the wind tunnel is a rectangular cube of size $30\times10\times10$ cm^3 made of Plexiglas to allow observation and prevent breakage. A pitot tube was employed to measure the air shear speed inside the test section. Experiments were performed on an aluminum plate which is placed inside the test section (shown in Figure 6.1 and 6.2). The substrate shape is designed in a way to avoid flow

instability around it (shown in Figure 6.1). Distilled water was injected from a pressurized tank throughout a narrow plastic tube (with the inlet diameter of 4.2 mm). A 1 mm surface hole was drilled on the test plate so that distilled water can be injected from this hole to the substrate. The flow rate of the injected water was controlled with a flow meter (Aalborg, NY, USA) and was constant (about 2 ml/min) in all the experiments.

To address the effect of surface wettability three different plates were used. The first substrate is a polished aluminum on which the static contact angle of a water droplet is about 75°± 1. Such a contact angle indicates that the aluminum plate is acting as a hydrophilic substrate. However, before performing the tests the surface was cleaned with acetone and distilled water several times and dried for 15 minutes. The second surface that acts as a hydrophobic substrate with a static contact angle of about 105°± 1, is a polished aluminum plate coated with Teflon spray (DuPont, Virginia, USA). To prepare this surface after cleaning the polished aluminum plate with the procedure described above, the surface was sprayed three times with the Teflon spray. However, before the second and third coats the substrate was dried for 30 minutes. Finally, the third surface that acts as a superhydrophobic with a static contact angle of about 155°± 1, is a polished aluminum plate coated with WX2100 spray (Cytonix, Maryland, USA). To prepare this surface after performing the cleaning procedure on the polished aluminum plate, it was sprayed with WX2100 three times. It should be mentioned that, the substrate was dried for 5 hours before applying the second and the third coats. All tests were performed at room temperature (about 22 °C). It should be noted that the tests were performed on the substrates only when the static contact angle of the water droplet on them is within the mentioned ranges above. In this case we can be confident that the substrates are acting as hydrophilic, hydrophobic or superhydrophobic accordingly. To observe the effect of surface

wettability and shear flow only, other parameters such as the water flow rate and the room temperature were kept constant during the experiments. Three different air speeds of 5, 10 and 20 m/s were introduced to the water film for all three substrates individually. It should be noted that each test was repeated fifteen times to ensure reproducibility. The reported results are the ensemble average of these twenty experiments for each case. ImageJ software [78] was used for post-processing the results in this work.

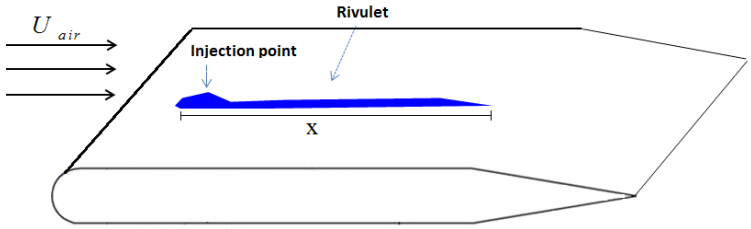

Figure 6.1 Test plate schematic [114]

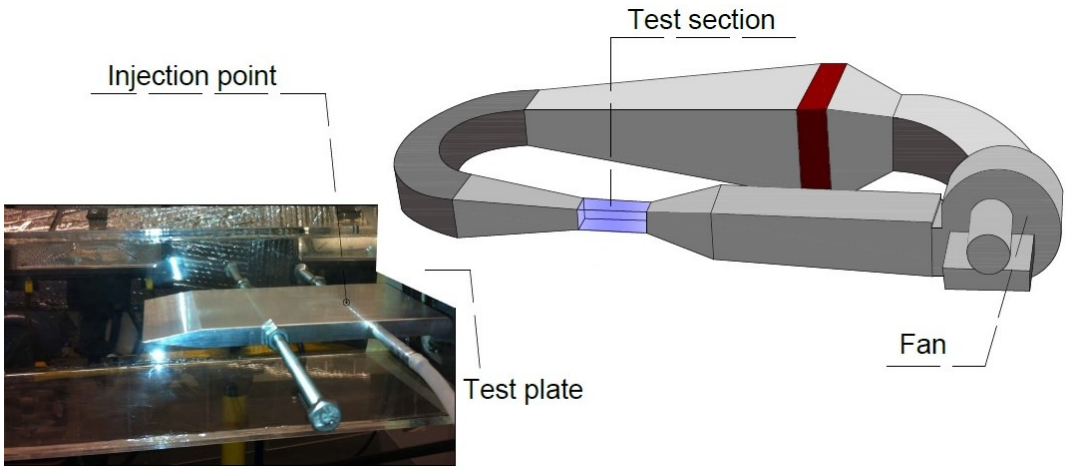

Figure 6.2 Experimental setup [114]

The details of the test matrix and surface characteristics are given in Table 6.1. It should be mentioned that the contact angle hysteresis defined in Table 6.1 is calculated based on the method that Milne and Amirfazli [44] proposed in their study. They measured the difference between the maximum contact angle (θ_{max}) and the minimum contact angle (θ_{min}) instead of the

traditional method of hysteresis measurement which is based on the difference between the advancing and the receding contact angles. It should be noted that when a sessile droplet is under the effect of shear flow, θ_{max} and θ_{min} refer to the droplet contact angles downstream and upstream of the flow, respectively as shown in Figure 6.3.

Table 6.1 Test Matrix

Surface material	Aluminum	Teflon	WX2100
Contact angle (°)	75± 1	105± 1	155± 1
Contact angle hysteresis (°)	18± 2	11± 2	8± 2
Shear speed (m/s)	5± 2	10± 2	20± 2

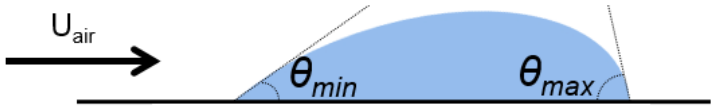

Figure 6.3 Schematic of hysteresis definition for surface characterization

6.3 Numerical Method

Smoothed Particle Hydrodynamics (SPH) used in this study is a numerical technique which discretizes the continuum through a set of nodes to approximate its dynamics by using interpolation points. The main idea of SPH like the other mesh-free methods is to treat nodes as material particles carrying physical properties. This method was originally developed to simulate astrophysical problems [115, 116]. Later on it was modified as a leading mesh-free method with wide variety of applications in fluid mechanics [117, 118].

In this method, the equations of motion can be easily derived for the nodes. Particle representation of SPH yields to a simultaneous conservation of mass, linear and angular momentum, energy and entropy (without applying artificial viscosity) [117] . Unlike the grid-based methods, the derivatives of quantities can be determined analytically in SPH. In addition, the absence of convective term in the governing equations makes the numerical computations

easier. Due to the Lagrangian nature of SPH, handling deformations and complex geometries, describing moving boundary conditions or irregular interfaces, and tracking the time-history of the variables will be comparatively simple.

In this study, the main reason for preferring SPH over grid-based models is the ability of this technique to easily track the moving boundaries which yields more accurate simulation of interfaces [119-121]. The principle features of SPH are described in details in [122-125]. The general procedure of SPH can be summarized in two steps; decomposing the continuum into a set of particles (without connectivity) and using finite summation instead of integral representation for approximating particle attributes.

SPH Theory and Implementation

The attributes of each particle in SPH depend on the objects being simulated. Some of the common characteristics for a particle are its position, mass, size, velocity, acceleration and etc.

For any field $A(r')$ in the fluid represented by a set of particles like $i \in [1, \dots, N]$, the smoothed interpolated version, $A_s(r)$ can be defined through a kernel $W(r - \acute{r}, h)$ [126];

$$A_s(r) = \int A(r')W(r - \acute{r}, h)\, d\acute{r} \qquad \textbf{Equation 6.1}$$

where $W(r - \acute{r}, h)$, is a smoothing kernel. This kind of kernel is nonparametric weight function which is used as an approximation for the Dirac delta function in the identity transform definition. It enables us to estimate the value of the quantity at each point based on the values at the neighboring points. The width of the kernel (h) approximates a Dirac delta function in the limit $h \to 0$. The main characteristics of an SPH kernel are as follows [117];

$$\lim_{h\to 0} W(r-\acute{r},h)\,d\acute{r} = \delta(r-\acute{r})$$ **Equation 6.2**

$$\int W(r-\acute{r},h)\,d\acute{r} = 1 \quad \textit{, (over the domain)}$$ **Equation 6.3**

$$W(r-\acute{r},h) \geq 0 \quad \textit{, (inside the domain)}$$ **Equation 6.4**

$$W(r-\acute{r},h) = 0 \quad \textit{, (outside of the domain)}$$ **Equation 6.5**

Based on [127-129], for an even and normalized kernel, SPH interpolation is of the second order. In order to improve stability, Müller *et al.* [128, 129] proposed to apply three kernels for the quantity interpolations that can be practically used for all of the simulation quantities. These easy and fast computable kernels are zero at the origin. To prevent clumping effect for pressure calculations W_{spiky} can be used [130]. Noting that clumping occurs when particles are so closed to each other that unrealistic clusters are produced due to numerical instability [130]. $W_{viscosity}$ is also recommended for viscosity, as it inhibits increase of particles relative velocity due to their positive Laplacian. These kernels are;

$$W_{poly6}(r,h) = \begin{cases} \frac{315}{64\pi h^9}\,(h^2-|r|^2)^3, & 0 \leq |r| \leq h \\ 0, & otherwise \end{cases}$$ **Equation 6.6**

$$W_{spiky}(r,h) = \begin{cases} \frac{15}{\pi h^6}\,(h-|r|)^3, & 0 \leq |r| \leq h \\ 0, & otherwise \end{cases}$$ **Equation 6.7**

$$W_{viscosity}(r,h) = \begin{cases} \frac{15}{2\pi h^3}\left(-\frac{|r|^3}{2h^3}+\frac{|r|^2}{h^2}+\frac{h}{2|r|}-1\right), & 0 \leq |r| \leq h \\ 0, & otherwise \end{cases}$$ **Equation 6.8**

By providing sufficient point and choosing smooth kernel, the integral in Equation 6.1 can be approximated by this summation;

$$A(r) = \sum_j m_j \frac{A_j}{\rho_j} W(r - r_j, h)$$ **Equation 6.9**

As the distribution of the points is more regular, the accuracy of this summation will be better than in Monte-Carlo method. In addition, it can be shown that in 3D modeling, the minimum number of neighbors are ~ 33 [131]. For example, by applying this definition, the smoothed estimate of the density at particle i can be found using;

$$\rho_i = \sum_j m_j W(r_i - r_j, h)$$ **Equation 6.10**

Also, the gradient and Laplacian of the smoothed function $A(r)$ are, respectively;

$$\nabla A(r) = \sum_j m_j \frac{A_j}{\rho_j} \nabla W(r - r_j, h)$$ **Equation 6.11**

$$\nabla^2 A(r) = \sum_j m_j \frac{A_j}{\rho_j} \nabla^2 W(r - r_j, h)$$ **Equation 6.12**

Each particle in SPH should have at least a position and velocity. These particles are moved by applying forces and calculating the acceleration. Other attributes can change over time as well, which represents the objects dynamic.

Fluid dynamics is about the study of fluid motion in response to the forces such as gravity, pressure and shear. In SPH, direct applying of force balance is necessary for finding velocities and positions of the particles in a transient process. It should be mentioned that the SPH method was first introduced as a new method for solving the equations of motion of a compressible fluid. The equations in this work are from the adaptation of the method for incompressible flow described by Monaghan [132]. In order to make a compressible fluid behave like an incompressible fluid, the pressure should increase in a way that the density does not change significantly. Thus, it will be difficult to compress the fluid any further. Equation 6.9 is the base to find the particle body forces and the acceleration a_i of the fluid particle *i* can be applied for each property in the following Lagrangian form of hydrodynamic equations [131];

$$\frac{d\rho}{dt} = -\rho\nabla . v$$ **Equation 6.13**

$$\frac{dv}{dt} = -\frac{1}{\rho}\nabla P$$ **Equation 6.14**

where ρ, P and v represent density, pressure and velocity, respectively.

For sufficiently small time steps, $d\rho_i/dt = \sum_j m_j v_{ij} \nabla_i W_{ij}$ which is the particle form of Equation 6.13 is recommended for density calculation, because Equation 6.10 may underestimate particles densities at fluid surfaces [125]. Also for Equation 6.14 by using Equations 6.9 and 6.11, we can have;

$$\frac{\nabla P_i}{\rho_i} = \sum_j m_j \left(\frac{P_i}{\rho_i^2} + \frac{P_j}{\rho_j^2}\right) \nabla_i W_{ij}$$ **Equation 6.15**

where $\nabla_i W_{ij}$ is the gradient of W with respect to particle i, considering particle j as its neighbor. The specific pressure format is applied for the summation in Equation 6.15, because using only $\sum_j m_j \left(\frac{P_i}{\rho_i}\right) W_{ij}$ for the pressure gradient does not result in force symmetry. Based on Monoghan [118], the proposed form of governing equations, can be written as;

$$\frac{d\rho_i}{dt} = \sum_j m_j v_{ij} \nabla_i W_{ij}$$ **Equation 6.16**

$$\frac{dv_i}{dt} = -\sum_j m_j \left(\frac{P_i}{\rho_i^2} + \frac{P_j}{\rho_j^2} + \Pi_{ij}\right) \nabla_i W_{ij} + F_i$$ **Equation 6.17**

The term Π_{ij} is an artificial viscosity which is usually added to control the shocks. The definition of this term based on [117, 133] is;

$$\Pi_{ij} = \begin{cases} \frac{-\psi \bar{c}_{ij}\mu_{ij}+\beta {\mu^2}_{ij}}{\bar{\rho}_{ij}} & if\ v_{ij}.r_{ij} < 0 \\ 0 & if\ v_{ij}.r_{ij} > 0 \end{cases}, \qquad \mu_{ij} = \frac{h v_{ij} r_{ij}}{{r^2}_{ij}+\eta^2} \qquad \textbf{Equation 6.18}$$

where ψ and β are viscous constants (usually set to 1 and 2, respectively), η is a constant used to avoid numerical divergences, and finally c identifies the mean speed of sound for particle i [134, 135];

$$c_i = \sqrt{\frac{\gamma P_i}{\rho_i}} \qquad \textbf{Equation 6.19}$$

γ is the ratio of specific heat and c_i represents the speed of sound through the fluid represented by particle i. Then, the acceleration a_i of the fluid particle i can be obtained by calculating the force density fields;

$$a_i = {}^1/_{\rho_i}\left(f_i^{pressure} + f_i^{viscosity} + f_i^{surface\ tension} + f_i^{gravity} + f_i^{external}\right) \qquad \textbf{Equation 6.20}$$

$$f_i^{pressure} = -\sum_j m_j \frac{P_j+P_i}{2\rho_j} \nabla W(r_{ij}, h) \qquad \textbf{Equation 6.21}$$

$$f_i^{viscosity} = \mu \sum_j m_j \frac{v_j - v_i}{\rho_j} \nabla^2 W(r_{ij}, h) \qquad \textbf{Equation 6.22}$$

$f_i^{external}$ are the external body forces for the system. $f_i^{surface\ tension}$ will be explained in the next sections.

For SPH, particle pressure has a significant effect in the calculations. The common constitutive equation for pressures P_i is computed by;

$$P_i = k(\rho_i - \rho_0) \qquad or \qquad P_i = B\left(\left(\frac{\rho_i}{\rho_0}\right)^\gamma - 1\right) \qquad \textbf{Equation 6.23}$$

where k is the stiffness of the fluid and ρ_0 is the rest density. For compressible fluid, by using derivative of equation of state with respect to density, relation between the fluid bulk modulus of elasticity in Equation 6.23 and the speed of sound (c) can be found as follows;

$$c^2(\rho) = \frac{\partial P}{\partial \rho} = \frac{B\gamma}{\rho_0^{\gamma}}\ \rho^{\gamma-1}$$ **Equation 6.24**

Applying Lagrangian projection method for enforcing incompressibility is shown to be very slow due to its implicit solution [85, 121, 128, 136, 137], therefore by assuming weak compressibility, Equation 6.23 can be used as a faster option even for incompressible fluids [138]. Monaghan however, used a different equation of state, for water [117];

$$P_i = B\left(\left(\frac{\rho_i}{\rho_0}\right)^{\gamma} - 1\right) \quad , \quad c_i = \sqrt{\frac{\gamma(P_i+B)}{\rho_i}} \quad , \quad B = \frac{200gH}{\rho\gamma}$$ **Equation 6.25**

where H is the maximum depth of water. This equation as we expect produces large changes in pressure for small changes in density.

There are some other attributes that play an important role for applying boundary conditions or stability of this numerical method. The color attribute in SPH is a quantity that is zero everywhere except at the liquid particle which is equal to one and it can be obtained as follows;

$$C_i = \sum_j \frac{m_j}{\rho_j}\ C_j\ W(r_{ij}, h)$$ **Equation 6.26**

This color attribute is set to zero for all air particles [129]. The gradient of the color field is;

$$\nabla C_i = \sum_j \frac{m_j}{\rho_j}\ C_j\ \nabla W(r_{ij}, h)$$ **Equation 6.27**

In general, large deviation in the magnitude of the color gradient shows that the particle is located at the fluid surface. This definition helps adding the surface tension force which tends to make the surface smooth. For surface tension, force is defined by [129, 139];

$$f_i^{surface\ tension} = -\sigma\ \nabla^2 C_i \frac{n_i}{|n_i|} \quad ,$$
$$n_i = \nabla C_i \quad ,$$
$$\nabla^2 C_i = \sum_j \frac{m_j}{\rho_j}\ C_j\ \nabla^2 W(r_{ij}, h)$$ **Equation 6.28**

This equation can cover the important effects of surface forces between the liquid and gas phases, however in case of forces on the liquid-solid interface, some additional procedures are

suggested in the literature [139-142]. Based on [140, 142] for the surface particles near the contact line of fluid and solid, it is recommended to use additional force term (parallel to the wall). The magnitude of this force per unit length is$(\sigma \cos \theta_D)$ where θ_D is the dynamic contact angle. For the particles located next to the contact line, instead of using $\frac{\nabla C_i}{|\nabla C_i|}$ for calculation of unit normal vector, it is proposed to use [140];

$$\hat{n} = \hat{n}_{wall} \cos \theta_D + \hat{n}_{contact\ line} \sin \theta_D \qquad \textbf{Equation 6.29}$$

where $\hat{n}_{contact\,line}$ is the unit vector parallel to the wall and $\hat{n}_{wall}$ is the unit normal vector directed into the wall.

Time Stepping

Another important issue in SPH technique is the collision between particles. The velocity of each particle should be adjusted to inhibit particle interpenetrations and mixing. To do so, the XSPH variant [117, 118] is useful especially for high speed flow. The variant is calculated by using;

$$\Delta v_i = \varepsilon \sum_j \frac{m_j v_{ij}}{\bar{\rho}_{ij}} W_{ij} \qquad \textbf{Equation 6.30}$$

where ε is a constant between 0 and 1. The variant should be added to the velocity when advancing the particle position in the time integration algorithm. However it does not affect the velocity used for other SPH computations.

To find the positions and velocities of the particles, using a standard and stable time integration method such as Verlet or leap-frog is inevitable. In this work, Verlet algorithm [143] is used. The main idea is to write one forward and one backward for the time variable in Taylor expansions. In this method, positions, velocities and accelerations at the next time are obtained from the same quantities at the current time.

$$r^{(n+1)}{}_i = r^{(n)}{}_i + v^{(n)}{}_i \Delta t + \frac{1}{2} a^{(n)}{}_i \Delta t^2$$ **Equation 6.31**

$$v^{(n+\frac{1}{2})}{}_i = v^{(n)}{}_i + \frac{1}{2} a^{(n)}{}_i \Delta t$$ **Equation 6.32**

$$v^{(n+1)}{}_i = v^{(n+\frac{1}{2})}{}_i + \frac{1}{2} a^{(n+1)}{}_i \Delta t$$ **Equation 6.33**

The time step size is determined by Courant condition which implies that the time step should be smaller than the amount of time it takes for sound to travel through that fluid over a specific distance. In SPH this specific distance is the smoothing length. For adjusting time steps, the Courant condition for our problem is [144-146];

$$\Delta t = min\left(\frac{Ch}{max(1, maximum\ of\ velocity)}, \sqrt{\frac{h}{maximum\ of\ acceleration}}, \frac{Ch}{maximum\ of\ sound\ speed}\right)$$

Equation 6.34

where *C* is the Courant safety factor.

By applying this condition and choosing the smallest time steps based on the flow velocity, the sound velocity and the velocity determined by the acceleration, the positions of particles in each time step can be controlled, so they do not travel too far in just one time step [121]. Therefore, for each time step, the procedure includes finding the neighbors of each particle, calculation of the density for each particle, calculation of pressure and other attributes for each particle, calculation and summation of all acceleration terms for each particle and applying Verlet method and then calculation of the new velocity and positions (to update position, XSPH variant should be calculated too).

In SPH algorithm, it is shown that computation time is significantly reduced by performing the summation only over the particles within the kernel width. This effective optimization method is widely used in literature [117, 118, 123, 132, 147]. The common algorithm for this

method includes creating cell grids in the domain (cells of width 2h), tracking particles location and their corresponding cells and summation only over the particles in the neighbor cells.

In this optimization for summation [148], each cell contains a reference to a list of all particles that map to the spatial location associated with the cell. In each time step, after searching for the particles in the adjacent cells, location and list of the particles in each grid should be updated. Obviously for a 3D grid cell, the maximum number of the neighboring cells is 26.

Boundary and Initial Conditions

Boundary conditions are not shown explicitly in SPH algorithm. Dynamic particles method [149] is used in this work in which particles have the same equations of continuity and state as the fluid particles, however their position remains unchanged. Because there are no extra considerations or special equations for these boundary particles, this method is computationally simple, with considerable less time for simulation. Validity of using dynamic boundary particles is extensively studied in literature [119, 130, 150, 151]. In this work, dynamic particles method is used for solid boundary condition and three layers of these fixed particles are placed outside the boundaries.

For all of the cases considered in this work, fluid particles are initially placed inside of the surface hole with the density equal to the rest density. Then for $t > 0$, all of the particles at the edge of the hole get a constant velocity (rate= 2 ml/min) and also air particles will have constant velocity at the edge of the sample depending on the simulations (for u_{air}= 5, 10 and 20 m/s).

For this isothermal SPH modeling, all the physical properties of air and water are selected for 22 °C. SPH particles are assumed to have constant mass equal to 10^{-9} kg and the number of water particles are set to 300,000. During the simulations as it will be explained in the next

section, maximum number of the necessary air particles is found to be ~150,000. The main tracking domain is assumed to be 0.09×0.05×0.05 m^3 and cell grids are created inside this domain to improve the search algorithm. The size of these grids is set to be 0.005 m. The values for time steps vary to satisfy Courant condition (values are found close to ~ 10^{-4} s).

Air-Water interface

In this work, two fluids (air and water) exist and interact with each other. Thus the standard SPH simulation which applies to a single fluid, cannot be used in these kinds of multiphase problems and applying boundary conditions will be difficult. Here, we have implemented a methodology based on the works done by Müller *et al*. [129]. This method treats water and air both as fluid particles. For a single fluid, usually most of the attributes can be stored globally like the particle mass m or the rest density ρ_i. In Müller *et al.* approach each particle carries all those attributes individually. For instance, as mentioned before, each particle carries its own viscosity force term, so for particles at the interface we can write;

$$f_i^{viscosity} = \sum_j m_j \frac{\mu_j+\mu_i}{2} \frac{v_j-v_i}{\rho_j} \nabla^2 W(r_{ij}, h) \qquad \textbf{Equation 6.35}$$

Nevertheless at this time, each one of i and j represents different fluids. The main difference between this method and the standard SPH can be seen in interface and surface tension simulation. Also, in this approach, interactions between air and water are applied by using color attribute and 'Air Particle Generation' method [127, 129]. The air generation method helps avoiding creation of large number surrounding air particles. The reason is that in this method air particles are generated only when they contribute to the simulation and when needed, they will be removed from tracking algorithm. In other words, for the flow direction, air particles need to be generated or tracked wherever water flows through the domain. Tracking color gradient will

help to locate the interface between water and air. This model is applied here for air particle generation and summation during transient behavior of the system.

6.4 Results and Discussions

As mentioned above, the aim of the present work is to investigate the behavior of narrow streams of liquid on surfaces with various wettabilities in response to different air shear speeds. To observe the narrow water film behavior preciously on each substrate, a side view image of the flow pattern is captured with the high speed camera for different air speeds. In addition to the experimental results, the numerical simulation based on the SPH method are also presented. The experimental and numerical image sequences on aluminum and Teflon plates are shown in Figure 6.4 and 6.5, respectively. As the initial stages of rivulet formation is not our concern in this study, the sequences taken by high speed camera are recorded after about 20 s of water injection on the plate for all the cases. The delay of 20 s is chosen for the starting time of image capturing because throughout experiments, we figured out that during this time the injected water can reach the end of the test plate and the rivulet is approximately at its stable form. Accordingly numerical simulations start after the rivulet reaches the end of the plate.

It is clear from Figure 6.4, that the injected water from the 1 mm surface hole creates the required rivulet on the aluminum plate. Increasing the air speed from 5 to 10 and 20 m/s results in the formation of wavy patterns on the rivulet surface. The same phenomena of rivulet formation can be observed in Figure 6.5 for the Teflon plate. Like the aluminum case, increasing the air speed results in the formation of waves on the surface of the rivulet. It should be noted that there is good agreement between the experimental and numerical results shown in Figure 6.4 and 6.5.

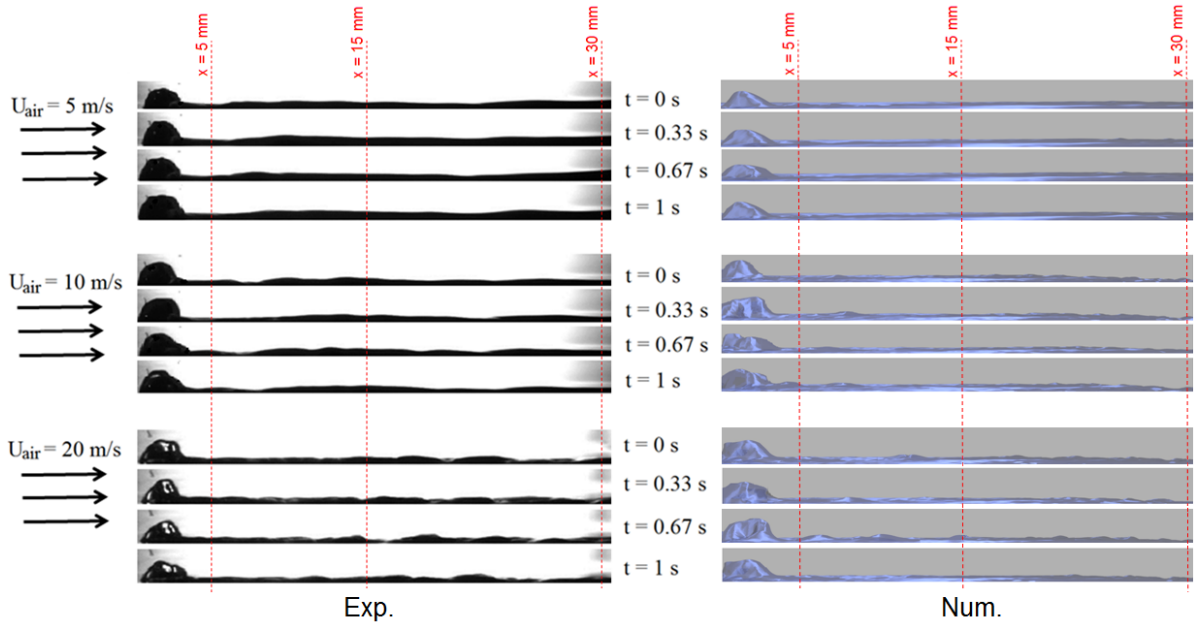

Figure 6.4 Experimental and numerical results of rivulet pattern sequences for different air speeds on the aluminum plate

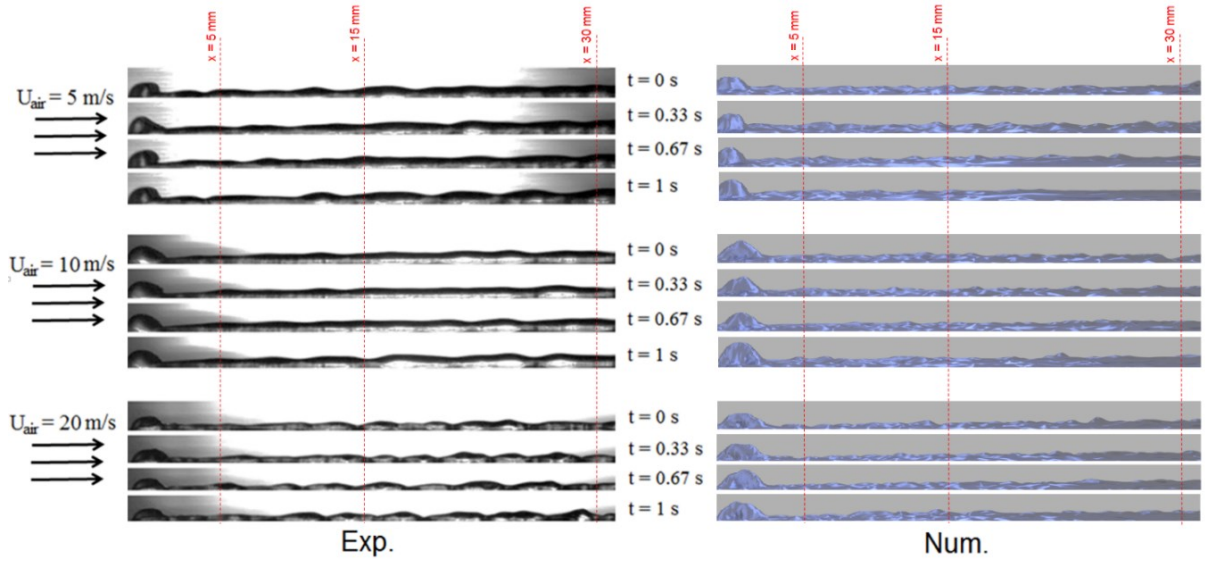

Figure 6.5 Experimental and numerical results of rivulet pattern sequences for different air speeds on the Teflon plate

More details of these wavy patterns on aluminum and Teflon substrates are shown in Figure 6.6, 6.7 and 6.8 for the air speed of 5, 10 and 20 m/s, respectively. For each air speed the variations of the rivulet thickness is plotted versus time at three different distances (x= 5, 15 and

30 mm) from the injection point of the water on the substrate. In these figures the experimental and the numerical results seem to be in a good agreement.

As shown in Figure 6.6, for the air speed of 5 m/s at 5 mm distance from the injection point (x= 5 mm), there is no significant change in rivulet thickness. However, at further distances of 15 and 30 mm, low frequency waves start to appear on the rivulet surface. It is worth mentioning that as the distance from the injection point increases, the average height of the rivulet also increases. For example for the aluminum case, the average height of the rivulet increases from approximately 0.36 mm to 0.62 mm as the distance from the injection point increases from x= 5 mm to x= 30 mm. The same phenomenon can be observed on the Teflon substrate. However, due to the lower adhesion between water and the Teflon substrates, the average height of the created rivulet on Teflon plate is higher than the rivulet average height on the aluminum substrate.

Variation of the rivulet thickness with the air speed of 10 m/s is shown in Figure 6.7 on aluminum and Teflon substrate. It can be observed that at x= 5 mm, there is almost no wavy patterns on the rivulet surface for both aluminum and Teflon substrates. However, at further distances from the injection point (here x= 15 and 30 mm), waves start to appear on the rivulet surface. Like the pervious case for 5 m/s of air speed, the frequency of the waves and the average rivulet thickness start to grow as the distance from the injection point increases.

Experimental and numerical results of the rivulet thickness variation versus time with the air speed of 20 m/s are plotted in Figure 6.8. In contrast to the lower air speed cases even at x= 5 mm, waves start to appear on the rivulet surface. The wave's frequency then starts to increase along the rivulet (at x= 15 and 30 mm). However, the increase in the average height of the rivulet for 20 m/s of air speed is not as noticeable as the increase for the lower speeds of 5 and 10 m/s.

Similar to the low air speed cases, the height of the rivulet is higher on Teflon substrate in comparison with the rivulet height on the aluminum plate.

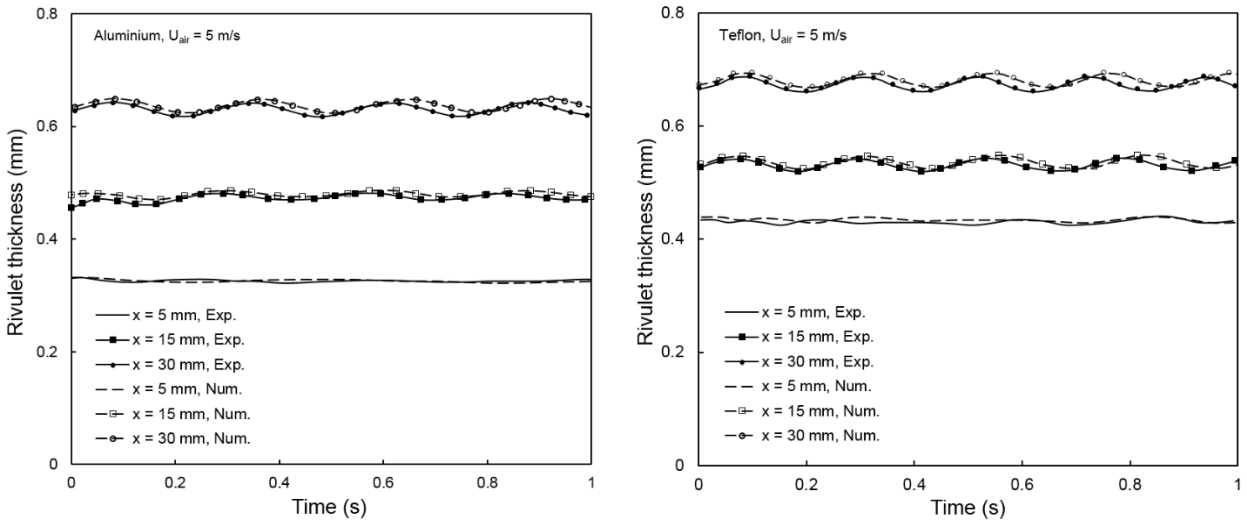

Figure 6.6 Experimental and numerical results of rivulet thickness variation on the aluminum and Teflon plates at different distances from the injection point for air speed of 5 m/s

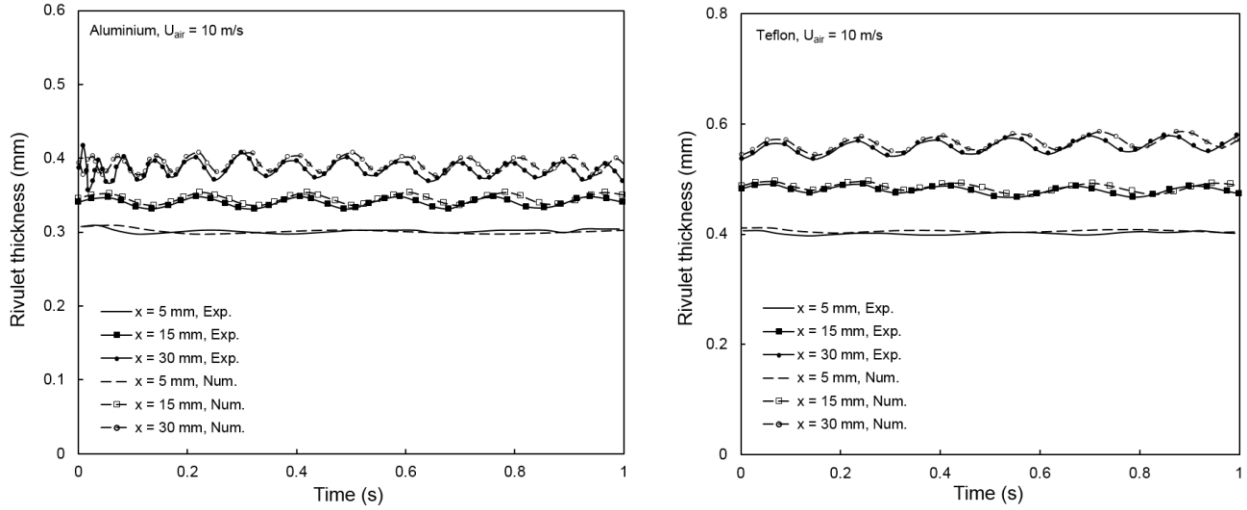

Figure 6.7 Experimental and numerical results of rivulet thickness variation on the aluminum and Teflon plates at different distances from the injection point for air speed of 10 m/s

As it is clear from Figures 6.6, 6.7 and 6.8 numerical simulations are in a good agreement with the experimental results.

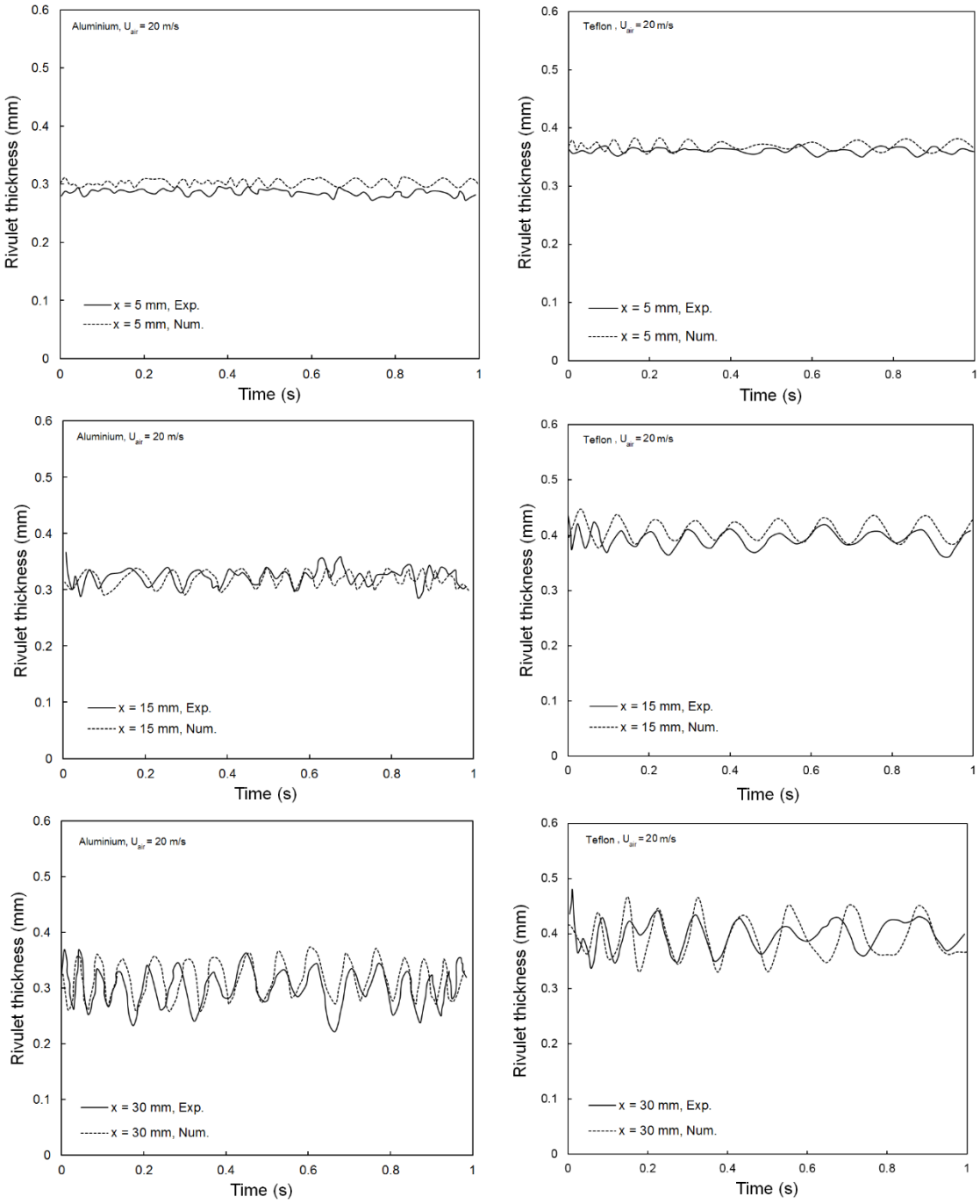

Figure 6.8 Experimental and numerical results of rivulet thickness variation on the aluminum and Teflon plates at different distances from the injection point for air speed of 20 m/s

The average height of the rivulet that is calculated based on the results given in Figures 6.6, 6.7 and 6.8, is shown in Tables 6.2 and 6.3 for the aluminum and Teflon substrates, respectively. These tables clearly show that the difference between the experimental and numerical results is

less than 3%. Furthermore for both substrates the maximum difference between the experimental and numerical results is observed when the air speed is 20 m/s which is due to the increase in the system turbulence.

Table 6.2 Experimental and numerical results for rivulet average height on the aluminum substrate

Aluminum	X = 5 mm			X = 15 mm			X = 30 mm		
	Exp.	*Num.*	*Deviation (%)*	*Exp.*	*Num.*	*Deviation (%)*	*Exp.*	*Num.*	*Deviation (%)*
U_{air} = 5 m/s	0.326	0.325	0.3	0.473	0.480	1.5	0.630	0.640	1.6
U_{air} = 10 m/s	0.301	0.306	1.7	0.340	0.345	1.5	0.384	0.391	1.8
U_{air} = 20 m/s	0.294	0.302	2.7	0.301	0.308	2.3	0.304	0.312	2.6

Table 6.3 Experimental and numerical results for rivulet average height on the Teflon substrate

Teflon	X = 5 mm			X = 15 mm			X = 30 mm		
	Exp.	*Num.*	*Deviation (%)*	*Exp.*	*Num.*	*Deviation (%)*	*Exp.*	*Num.*	*Deviation (%)*
U_{air} = 5 m/s	0.431	0.436	1.2	0.531	0.536	0.9	0.674	0.681	1.0
U_{air} = 10 m/s	0.402	0.407	1.2	0.480	0.485	1.0	0.559	0.566	1.3
U_{air} = 20 m/s	0.361	0.370	2.5	0.394	0.401	1.8	0.398	0.409	2.8

To make the analysis of the wavy patterns easier, Fast Fourier Transform (FFT) analysis is performed on both experimental and numerical results of Figures 6.6, 6.7 and 6.8. Based on the FFT analysis the average magnitude and frequency of the generated waves on the rivulet surface for air speeds of 5, 10 and 20 m/s are plotted for aluminum and Teflon substrates at different locations of x= 15 and 30 mm. The FFT analyses, shown in Figure 6.9, are not performed for x= 5 mm, as there is almost no wavy patterns at this location for the air speed of 5 and 10 m/s.

It is shown in Figure 6.9 that for both aluminum and Teflon substrates, with the constant air speed, increasing the distance from the injection point results in an increase in wave magnitudes. In other words as shown in Figure 6.9, the black lines that are related to the wavy patterns at x= 15 mm, always have lower magnitude than the blue lines that are related to the waves created at

x= 30 mm. As mentioned earlier, increasing the air speed results in an increase in the wave's frequency. In other words the number of the peaks increases in the graphs when the air speed is increasing from 5 to 20 m/s.

To compare the waves generated on aluminum and Teflon substrates it can be mentioned that that with the same air speed, the magnitude of the waves on the aluminum plate is lower than the ones on the Teflon plate. However, the frequency of the waves generated on the aluminum plate is higher than the ones on the Teflon substrate. As a result the graphs for the aluminum plate have more peaks with lower magnitudes in comparison with the graphs related to the same velocity but on the Teflon plate. The reason can be related to the lower adhesion between the Teflon substrate and water.

It is known that FFT analysis can provide detailed information about the experimental and numerical analysis that cannot be captured through the rivulet thickness graphs shown in Figures 6.6, 6.7 and 6.8. Based on the FFT analysis, it can be mentioned that the numerical and experimental results are in good agreement for low air speed of 5 m/s. For the higher air speeds of 15 and 20 m/s, the frequencies with the highest magnitude are also well-matched. However there is a small difference between the experimental and numerical results for the frequencies with low magnitude which can be due to both experimental and numerical errors. In this study the results of the average rivulet height is the most important parameter. These results show less than 3% difference throughout experimental and numerical analyses (see Tables 6.2 and 6.3).

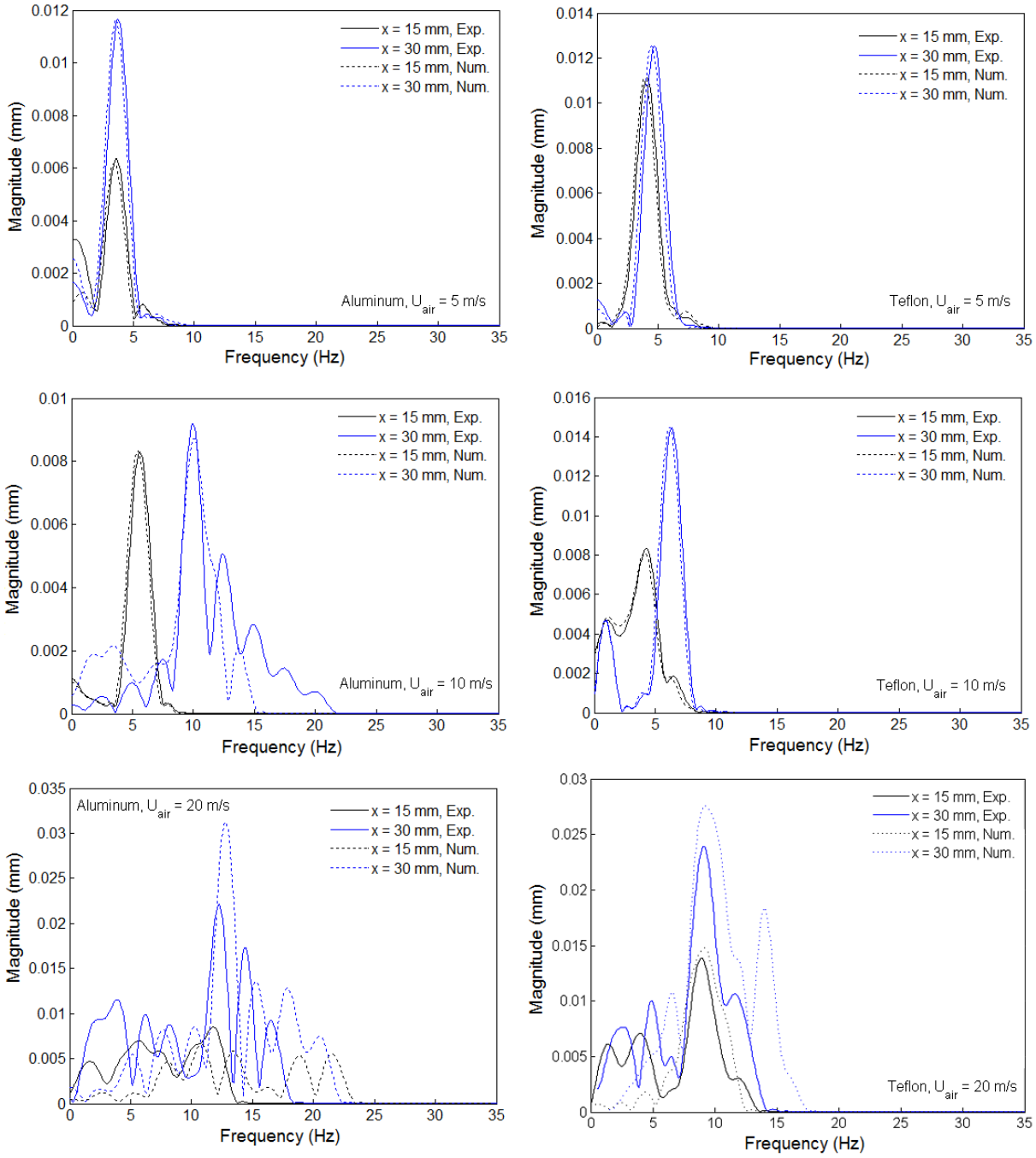

Figure 6.9 FFT analysis of the generated waves on rivulet surface for the aluminum and Teflon substrates

The result of water injection on the superhydrophobic plate is shown in Figure 6.10. In contrast with the aluminum and Teflon cases, there is no rivulet formation on the superhydrophobic substrate. Instead, separated droplets roll and shed on the plate. In other

words, on the superhydrophobic surface, the amount of the adhesion force is much less than on the other two substrates, which prohibits the liquid to form a rivulet and flow on the surface. Instead, to reach the minimum surface energy a semi oval shape droplet is formed on the surface (at the point of water injection to the plate) which is connected to the fluid bulk below it. However, after reaching a critical size due to the air shear effect the droplet detaches from the fluid bulk and starts to roll on the surface. It is worth mentioning that the droplet detachment from the liquid bulk happens at the time that the air shear force overcomes the adhesion of the droplet to the fluid bulk. As a result, the size of the droplet which is detached from the fluid bulk is smaller for the higher air speeds.

As the water flow rate is constant, increasing the air speed results in more frequent droplet detachments on the superhydrophobic plate. Apparently, the detachment time of the droplets from the substrates decreases with increasing the air speed which is shown in Figure 6.10. For the low speed of 5 m/s the created droplets only roll on the substrate. Nevertheless, the detachment of the first generated droplet from the fluid bulk, occurs at about 90 and 24 ms (after the start of image recording) for air speeds of 10 and 20 m/s, respectively.

As mentioned above the droplet gets detached from the fluid bulk as soon as the air shear force overcomes the adhesion of the droplet to the fluid bulk. To analyze this phenomenon the air speed, the droplet surface tension and the detached-droplet diameter are normalized based on [114] as below;

$$We = \frac{\rho_{air} u^2_{air} D_{inj.}}{\sigma_w} \qquad \textbf{Equation 6.36}$$

$$D^* = \frac{D_{drop}}{D_{inj.}} \qquad \textbf{Equation 6.37}$$

where We and D^* are the droplet Weber number and normalized diameter, respectively. σ is water surface tension at 22 ^{o}C, respectively. ρ_{air} and u_{air} are the air density and shear speed,

respectively. D_{drop} is the diameter of the detached droplet from the fluid bulk and $D_{inj.}$ is the diameter of the surface hole from which water is injected to the surface (in this work $D_{inj.}$= 1 mm).

Variations of D^* versus Weber number based on the numerical simulations are plotted in Figure 6.11. In addition, the numerical results are compared with the experimental results taken from [114]. As it is clear from Figure 6.11 there is a good agreement between the experimental and numerical results. It is demonstrated in Figure 6.11 that increasing the Weber number results in detachment of droplets with smaller size from the fluid bulk (also depicted in Figure 6.10). Finally, the results of the present work confirm that low adhesion of water on superhydrophobic substrates makes them an ideal candidate for anti/di-icing purposes [14-16].

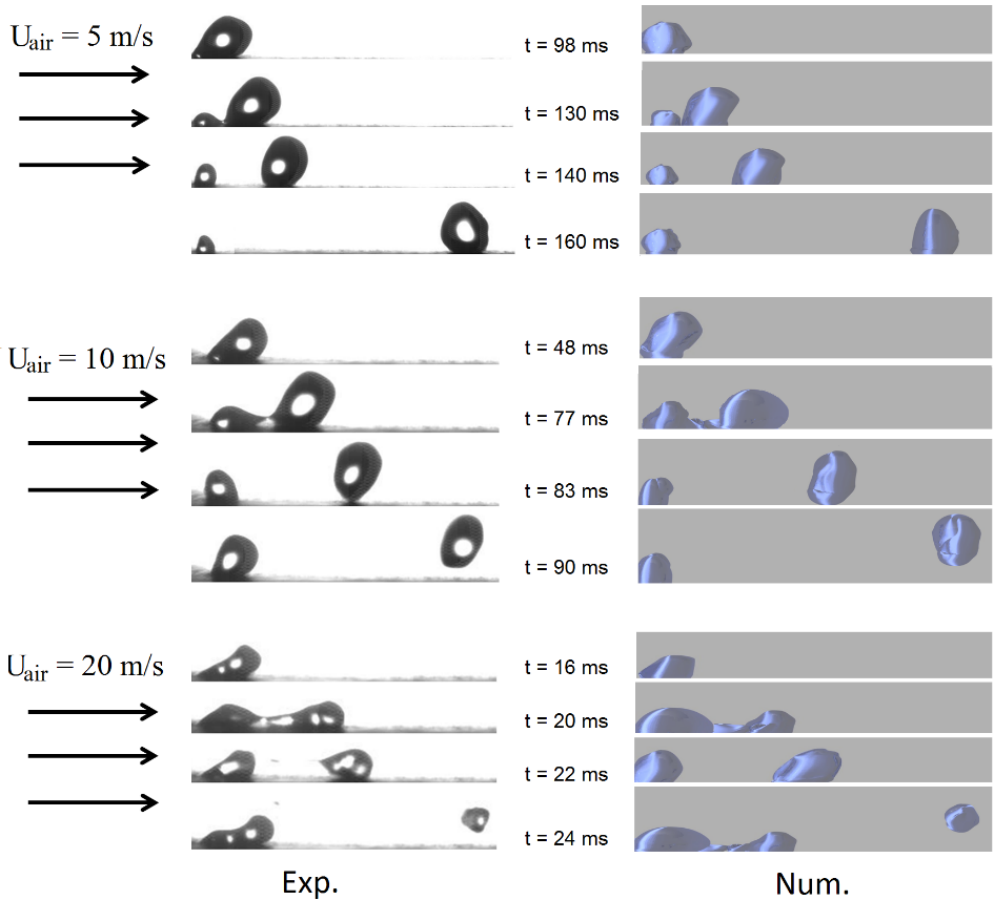

Figure 6.10 Sequences of the droplet formation for different air speeds on the superhydrophobic substrate

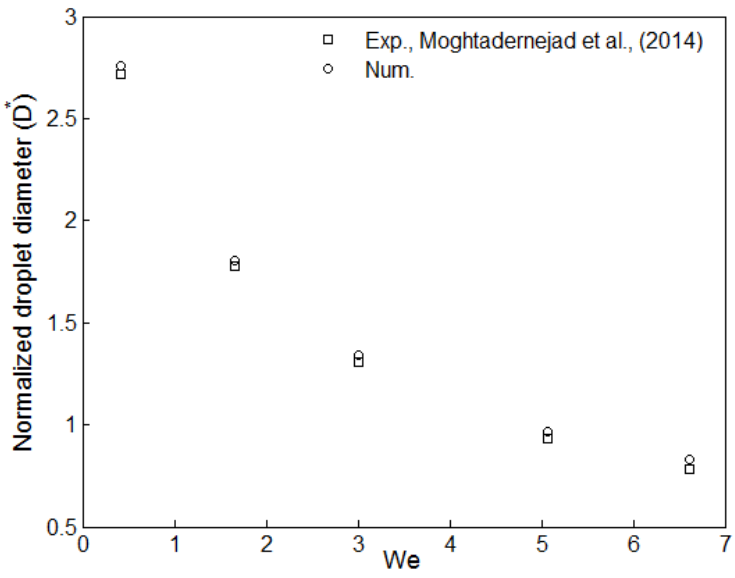

Figure 6.11 Normalized droplet diameter vs. Weber number on the superhydrophobic substrate

6.5 Summary and Conclusions

The effect of air shear flow on rivulet dynamics was investigated on surfaces with various wettabilities ranging from hydrophilic to superhydrophobic. It was shown that on hydrophilic and hydrophobic surfaces, increasing the air speed results in the formation of waves on the rivulet surface with higher frequency in comparison with the lower air speeds. On these surfaces the rivulet height increases as it flows along the plate. However, the average height of the generated rivulet is higher on the hydrophobic surface in comparison to the hydrophilic substrate due to the lower adhesion of water to the hydrophobic plate. In contrast, on the superhydrophobic plate due to the very low adhesion of water to the surface, a series of water droplets are created on the surface instead of a rivulet. In other words, decreasing the wettability of the surface changes the rivulet shape from nearly flat (on aluminum and Teflon plate) to a semi oval droplets on the superhydrophobic plate. Moreover, the air shear flow results in the deformation and detachment of the droplets from the superhydrophobic substrate. Consequently,

superhydrophobic surfaces can be ideal candidates for anti-icing purposes as the amount of water accumulation on them is considerably less than the hydrophilic and hydrophobic substrates. Numerical analyses with SPH technique was also performed to simulate the same flows which were in agreement with the experimental results. This study can be further implemented on surfaces with subzero temperatures to analyze the icing condition on rivulet dynamics.

Chapter 7

Conclusions and Suggestions for Future Work

7.1 Summary and Conclusions

The aim of this work was to analyze the behavior of water droplets and rivulets under the effect of air shear flow and different surface morphologies. This work was mainly experimental and consisted of two main setups. The first setup was developed for investigating the effect of various air flows as high as 90 m/s on the shedding and coalescence behavior of one and two sessile droplets placed on aluminum (hydrophilic) and WX2100 (superhydrophobic) substrates. The results on the superhydrophobic substrate were compared with the results of numerical simulations based on VOF method coupled with the LES turbulent model to shed more light on the mechanism of droplet shedding and coalescence through a detailed analysis of the aerodynamics forces, velocity vectors and streamlines surrounding the droplets. To account for the concurrent shedding and solidification of water droplets, a cold plate was used for decreasing the substrate temperature as low as -5 ^{o}C. The shedding and coalescence evolvement were analyzed based on the side and top view images taken by a high speed camera in addition to the graphs plotted based on the variation of droplets wetting length and contact angles during the process. Droplet detachment time on the superhydrophobic plate and its residence time before transforming to a rivulet on the hydrophilic plate were two parameters introduced in this work and the effect of Reynolds number was investigated on these parameters.

The second setup was designed to perform a steady state flow arrangement to study the formation and evolution of rivulets on hydrophilic, hydrophobic and superhydrophobic surfaces. The experiments were performed inside a wind tunnel with a maximum air speed of 20 m/s. Variations of rivulet thickness were analyzed in detail by using high speed shadowgraphy and image processing techniques. Additionally, FFT analysis was performed on the results of rivulet thickness variations to give a better understanding of the frequency and amplitude of the generated waves on the rivulet surface. The experimental results were also compared with the numerical results based on SPH method using the same boundary conditions. The experiments in this work were conducted several times (minimum fifteen times for each case) to reach an acceptable degree of repeatability and accuracy. The highlights of the findings in this work can be summarized as below.

- The results of the shedding phenomenon of a single droplet were compared on hydrophilic and superhydrophobic substrates. It was shown that on the hydrophilic substrate, when the air speed is high enough, droplet deformation occurs which leads to the formation of rivulets. In contrast on superhydrophobic substrate, with low air speed the droplet rolls on the substrate and when the shear speed is high enough droplet detaches from the surface. In addition, increasing the Reynolds number results in faster detachment of the droplet from the superhydrophobic plate.
- The shedding phenomenon of a single droplet was compared with the coalescence of two droplets on hydrophilic and superhydrophobic substrates. It was displayed that in the two droplet case on hydrophilic substrate after merging, high adhesion of the droplets to the surface resulted in the formation of rivulet. On the other hand, on the superhydrophobic substrate in the two droplet case, after merging, the droplet

bounces on the substrate due to the oscillations resulted from the conversion between surface energy and kinetic energy. Increasing the air speed (as high as 90 m/s) results in the detachment of the coalesced droplet from the superhydrophobic surface. Noting that in the two droplet case on both substrates (hydrophilic and superhydrophobic) due to the existence of separation bubbles behind the first droplet the second drop was attracted to the first one and coalescence was assisted.

- It was shown through the concurrent shedding and solidification experiments that decreasing the temperate resulted in rivulet solidification on hydrophilic substrate. Moreover on the superhydrophobic substrates with temperatures as low as -5 ^{o}C, icing did not occur on the surface. Noting that due to the formation of frost layer on the surface the hydrophobicity was partially diminished which lead to some droplets pinned to the plate. This phenomenon indicates that for temperatures as low as -5 ^{o}C superhydrophobic substrates can be good candidates for anti-icing purposes.
- Steady state experiments of rivulet evolution in wind tunnel together with SPH simulation revealed that the frequency of the generated waves on rivulet surface on hydrophilic and hydrophobic substrates was increased by increasing the shear speed. Furthermore, due to the lower adhesion of water to the hydrophobic substrate the average rivulet height was higher in comparison with the one on the hydrophilic plate. Interestingly, no rivulet is formed on the superhydrophobic substrate, instead series of separated droplets are generated that were deformed and detached from the plate.

7.2 Scope for Research and Future Work

The present thesis serves as a fundamental study on the effect of shear speed and surface wettability on dynamics of droplet shedding, coalescence and rivulet formation. Various improvements can be suggested in addition to profound and targeted studies. Should the reader be interested, a list of proposed future research work can be suggested as below;

- *Adding the effect of droplet impact to the shedding phenomenon*; in this study the effect of a sessile droplet shedding was investigated under the effect of air shear flow. However, there are circumstances when the droplets impact on the surface in addition to being under the effect of shear flow. Examples include rain droplets impact on airfoil or power line surfaces while they are subjected to wind shear flow. To do this study experimentally, the droplet impact system should be synchronized with the air flow system so that at the time the droplet hits the surface the air flow is introduced to it. Otherwise it may be challenging to capture the phenomenon accurately.
- *Investigating the effect of supercooled droplet shedding and coalescence*; in this work the study was done on water droplets; however, it is known than supercooled droplets that exist in clouds, can be one of the important factors resulting in ice formation on aircraft wings. One interesting approach can be studying the effects of shear flow and surface wettability on dynamics of supercooled droplets; noting that generating these droplets is challenging and their viscosity and surface tension are different from those of water droplets.
- *Adding the effect of micro droplet size to the shedding and coalescence analysis;* the analyses of this work were performed on 2 mm droplet sizes. However as most of the supercooled droplets that exist in clouds are of the range of a micrometer,

investigating the micro droplet size effect will be beneficial for industries. Dealing with micro droplets, the size of the pillars that exist on superhydrophobic surfaces becomes crucial. When the droplets size is smaller than the pillar size, the droplets can rest in between the pillars. Consequently, there will be a change in the wetting regime (i.e. from Cassie-Baxter to Wenzel). One of the challenges in this study is to minimize the disturbances around the system which can affect the dynamics of micro droplets. To do so, the micro droplet generator system should be kept isolated from the surrounding environment by placing it inside a closed chamber for example.

- *Investigating the delay effect between droplet deposition on the cold plate and the introduction of the shear flow*; it was mentioned in this thesis that the air flow was introduced to the droplets immediately after depositing them on the substrate. It is important to note that for the solidification test, the delay between droplet deposition and introducing air flow to the substrate is playing a crucial role in the icing behavior of the droplets. The more this delay is, the more conduction rate between the droplet and the surface happens which enhances the solidification.
- *Adding the effect of subzero ambient temperature to the solidification experiments*; the solidification experiments present in this work were performed on a cold plate with temperature of -5 ^{o}C. It should be noted that the air flow was 22 ^{o}C in all the experiments. To simulate the real icing condition, in addition to the substrate, the air flow should be at subzero temperatures as well. To do so the solidification test should be performed in a closed icing chamber.
- *Adding the effect of controlled humidity to the solidification experiments*; the solidification experiment in this work was performed in the presence of humidity

which resulted in formation of a frost layer on the substrates which resulted in diminishing the hydrophobicity of the superhydrophobic plate. To increase the performance of superhydrophobic surfaces the experiments can be performed in controlled environment (i.e. closed chamber with zero humidity) to address the relative humidity effect on the solidification process.

- *Analysis of the rivulet breakup*; in this thesis rivulet thickness variation together with analysis of the wavy patterns on rivulet surface was investigated. The rivulet breakup analysis is also an interesting phenomena that can be added to this study. In the case presented in this work the breakup does not happen as the maximum velocity inside the wind tunnel is 20 m/s and the maximum substrate length that rivulet analysis can be performed on is 9 mm. There are two possibilities to be able to capture the break up phenomenon. The first solution is to perform the experiments on a larger test plate which needs a wind tunnel with a bigger test section. The second alternative is to use a fan that generates higher air flow inside the wind tunnel.

Bibliography

1. R. Li, N., Ashgriz, S., Chandra, J.R., Andrews, and S., Drappel, *Coalescing of two droplets impacting a solid surface.* Exp. Fluids, 2010. **48**: p. 1025-1035.
2. R. Li, N., Ashgriz, S., Chandra, J.R., Andrews, and J., Williams, *Drawback during deposition of overlapping molten wax droplets.* J. Manuf. Sci. Eng., 2008. **130**(4).
3. R. Dhiman, S., Chandra, *Freezing-induced splashing during impact of molten metal droplets with high Weber numbers.* Int. J. Heat and Mass Transfer, 2005. **48**(25-26): p. 5625–5638.
4. D. Soltman, V., Subramanian, *Ink-jet printed line morphologies and temperature control of the coffee ring effect.* Langmuir, 2008. **24**(5): p. 2224–2231.
5. A. Alizadeh, M., Yamada, R., Li, W., Shang, S., Otta, S., Zhong, L., Ge, A., Dhinojwala, K.R., Conway, V., Bahadur, A.J., Vinciquerra, B., Stephens, and M.L., Blohm, *Dynamics of ice nucleation on water repellent surfaces.* Langmuir, 2012. **28**(6): p. 3180-3186.
6. M. Holl, Z., Patek, and L., Smrcek, *Wind tunnel testing of performance degradation of ice contaminated airfoils.* ICAS Technical Paper 3.1.1, 2000.
7. Young, T., *An essay on the cohesion of fluids.* Phil. Trans. R. Soc. London 1805. **95**: p. 65-87
8. G. Wolansky, A., Marmur, *The actual contact angle on a hetrogeneous rough surface in three dimensions* Langmuir, 1998. **14**(18): p. 5292-5297.
9. B. Bhushan, Y.C., Jung and K., Koch, *Micro-nano and hierarchical structures for superhydrophobicity, self-cleaning and low adhesion.* Philos. Trans. A. Math. Phys. Eng. Sci., 2009. **367**: p. 1631-1672.
10. Wenzel, R.N., *Resistance of solid surfaces to wetting by water.* Indust. Eng. Chem., 1936. **28**: p. 988-994.
11. Marmur, A., *Wetting of hydrophobic rough surfaces: To be heterogeneous or not to be* Langmuir, 2003. **19**(20): p. 8343–8348.
12. E. Bormashenko, T., Stein, R., Pogreb, and D., Aurbach, *"Petal effect"on surfaces based on lycopodium: High-stick surfaces demonstrating high apparent contact angles.* J. Physical Chem. C, 2009. **113**(14): p. 5568-5572.
13. B. Bhushan, Y.C., Jung, *Micro and nanoscale characterization of hydrophobic and hydrophilic leaf surfaces* Nanotechnology, 2006. **17**(11): p. 2758-2772
14. A.B.D. Cassie, C., Baxter, *Wettability of porous surfaces.* Trans. Faraday Soc., 1944. **40**(546-551).
15. M. Nosonovsky, B., Bhushan, *Patterned nonadhesive surfaces: Superhydrophobicity and wetting regime transitions.* Langmuir, 2008. **24**: p. 1525-1533.
16. A.J. Meuler, J.D., Smith, K.K., Varanasi, J.M., Mabry, G.H., McKinley and R.E., Cohen, *Relationships between water wettability and ice adhesion.* ACS Appl. Materials and Interfaces, 2010. **2**: p. 3100-3110.
17. S. Kulinich, M., Farzaneh, *Ice adhesion on superhydrophobic surfaces.* Appl. Surf. Sci., 2009. **225**(18): p. 8153-8157.
18. X. Li, D., Reinhoudt and M., Crego-Calama, *What do we need for a superhydrophobic surface? A review on the recent progress in the preparation of superhydrophobic surfaces.* Chem. Soc. Rev., 2007. **36**: p. 1350-1368.
19. J. Genzer, K., Efimenko, *Recent developments in superhydrophobic surfaces and their relevance to marine fouling: A review.* Biofouling, 2006. **22**: p. 339-360.
20. W. Barthlott, C., Neinhuis, *Purity of the sacred lotus, or escape from contamination in biological surfaces.* Planta, 1997. **202**(1): p. 1-8.

21. J.A. Nychka, M.M., Gentleman, *Implications of wettability in biological materials science.* JOM, 2010. **62**: p. 39-48.
22. X. Zhang, F., Shi, J., Niu, Y., Jiang, and Z., Wang, *Superhydrophobic surfaces: From structural control to functional application.* J. Mater. Chem., 2008. **18**: p. 621-633.
23. M. Farhangi, P.J., Graham, N.R., Choudhury, and A., Dolatabadi, *Induced detachment of coalescing droplets on superhydrophobic surfaces* Langmuir, 2012. **28**(2): p. 1290–1303.
24. M. Callies, D., Quéré, *On water repellency.* Soft Matter, 2005. **1**: p. 55-61.
25. A. Lafuma, D., Quéré, *Superhydrophobic states.* Nature Materials, 2003. **2**: p. 457-460.
26. D.Oner, T.J., McCarthy, *Ultrahydrophobic surfaces; Effects of topography length scales on wettability* Langmuir, 2000. **16**(20): p. 7777-7782.
27. J. Drelich, J.L., Wilbur, J.D., Miller, and G.M., Whitesides, *Contact angles for liquid drops at a model heterogeneous surface consisting of alternating and parallel hydrophobic/hydrophilic strips.* Langmuir, 1996. **12**(7): p. 1913-1922.
28. A. Frohn, N., Roth, *Dynamics of droplets*. 2000, Berlin: Springer
29. Ashgriz, N., *Handbook of atomization and sprays*. 2011, Heidelberg, NY Springer.
30. L. Duchemin, J., Eggers, and C., Josserand, *Inviscid coalescence of drops.* J. Fluid Mech., 2003. **487**: p. 167–178.
31. Yarin, A.L., *Drop impact dynamics: Splashing, spreading, receding, bouncing.* Annu. Rev. Fluid Mech., 2006. **38**: p. 159-192.
32. Worthington, A.M., *The splash of a drop*. 1895, London: Society for promoting christian knowledge.
33. Worthington, A.M., *A study of splashes* 1908, Davenport: The Royal Naval Engineering College.
34. S. Chandra, C.T., Avedisian, *On the collision of a droplet with a solid surface.* Math. Phys. Sci., 1991. **432**: p. 13-41.
35. M. Pasandideh-Fard, Y.M., Qiao, S., Chandra, and J., Mostaghimi, *Capillary effects during droplet impact on a solid surface.* Phys. Fluids, 1996. **8**(3): p. 650-659.
36. D.C. Vadillo, A., Soucemarianadin, C., Delattre, and D.C.D, Roux, *Dynamic contact angle effects onto the maximum drop impact spreading on solid surfaces.* Phys. Fluids, 2009. **21**: p. 1-8.
37. C. Ukiwe, D., Kwok, *On the maximum spreading diameter of impacting droplets on well-prepared solid surfaces.* Langmuir, 2005. **21**(2): p. 666-673.
38. L. Chen, Z., Xiao, P.C.H., Chan, Y.K., Lee, and Z., Li, *A comparative study of droplet impact dynamics on a dual-scaled superhydrophobic surface and lotus leaf.* Appl. Surf. Sci., 2011. **257**(21): p. 8857-8863.
39. J.B. Lee, S.H., Lee, *Dynamic of wetting and spreading characteristics of a liquid droplet impinging on hydrophobic textured surfaces.* Langmuir, 2011. **27**(11): p. 6565-6573.
40. A. Menchaca-Rocha, A., Martinez-Davalos, and R., Nunez, *Coalescence of liquid drops by surface tension.* Phys. Rev. E 2001. **63**: p. 046309
41. S.G. Bradley, C.D., Stow, *Collisions between liquid drops*, in *Philos. Trans. R. Soc.* . 1978: London. p. 635−675
42. A. Brandes, G., Zhang, and J., Vivekanadan, *Drop size distribution retrieval with polarimetric radar model and application.* J. Appl. Meteorol., 2004. **43**(461).
43. E.B. White, J.A.J., Schmucker, *A runback criterion for water drops in a turbulent accelerated boundary layer.* J. Fluids Eng., 2008. **130**: p. 061302–6.
44. A.J.B. Milne, A., Amirfazli, *Drop shedding by shear flow for hydrophilic to superhydrophobic surfaces.* Langmuir, 2009. **25**(24): p. 14155–14164.
45. M.W. Lee, D.K., Kang, S.S., Yoon, and A.L., Yarin, *Coalescence of two drops on partially wettable substrates.* Langmuir, 2012. **28**: p. 3791–3798.

46. Frenkel, J., *Viscous flow of crystalline bodies under the action of surface tension.* J. Phys. Moscow, 1945. **9**: p. 385−391.
47. J. Eggers, J.R., Lister, and H.A., Stone, *Coalescence of liquid drops.* J. Fluid Mech., 1999. **401**: p. 293–310.
48. Eggers, J., *Coalescence of spheres by surface diffusion.* Phys. Rev. Lett., 1998. **80**: p. 2634−2637.
49. Vorst, G.A.L., *Integral method for a two-dimensional Stokes flow with shrinking holes applied to viscous sintering.* J. Fluid Mech., 1993. **257**: p. 667−689
50. Vorst, G.A.L., *Modeling and numerical simulation of viscous sintering*. 1994, TU Eidhoven.
51. W.D. Ristenpart, P.D., McCalla, R.V., Roy, and H.A., Stone, *Coalescence of spreading drops on a wettable substrate.* Phys. Rev. Lett., 2006. **97**: p. 064501.
52. S.T. Thoroddsen, K., Takehara, and T.G., Etoh, *The coalescence speed of a pendant and a sessile drop.* J. Fluid Mech., 2005. **527**: p. 85**–**114
53. M. Wu, T., Cubad, and C.M., Ho, *Scaling law in liquid drop coalescence driven by surface tension.* Phys. Fluids, 2004. **16**: p. 51-54.
54. R.D. Narhe, D.A., Beysens, and Y.D., Pomeau, *Dynamic drying in the early-stage coalescence of drops sitting on a plate.* Europhys. Lett., 2008(81): p. 46002
55. P.J. Graham, M., Farhangi, and A., Dolatabadi, *Dynamics of droplet coalescence in response to increasing hydrophobicity.* Phys. Fluids, 2012. **24**: p. 112105.
56. H.Y. Kim, J.H., Kim, and B.H., Kang, *Meandering instability of a rivulet.* J. Fluid Mech., 2004. **498**: p. 245-256.
57. Diez, J.A., *Contact line instabilities of thin liquid films.* Phys. Rev. Lett., 2001. **86**(4): p. 632-635.
58. P. Schmuki, M., Laso, *On the stability of rivulet flow.* J. Fluid Mech., 1990. **215**: p. 125-143.
59. S. Schiaffino, A.A.S., *Formation and stability of liquid and molten beads on a solid surface.* J. Fluid Mech, 1997. **343**: p. 95-11-.
60. G.W. Young, S.H., Davis, *Rivulet instabilities.* J. Fluid Mech, 1987. **176**: p. 1-31.
61. E. Momoniat, T.G., Myers, and S., Abelman, *New solutions for surface driven spreading of thin film* Int. J. Non-Linear Mech., 2005. **40**(4): p. 523-529.
62. A. Oron, S.H., Davis, and S.G., Banko, *Long-scale evolution of thin liquid films.* Rev. Modern Phys., 1997. **69**(3): p. 931-980.
63. J.S. Marshall, R., Ettema *Rivulet dynamics with variable gravity and wind shear*. 2004.
64. Gajewski, A., *Contact angle and rivulet width hysteresis on metallic surfaces. Part I : With heated surface.* Int. J. Heat and Mass Transfer, 2008. **51**(25-26): p. 5762-5771.
65. Gajewski, A., *Contact angle and rivulet width hysteresis on metallic surfaces. Part II : With cooled surface.* Int. J. Heat and Mass Transfer 2009. **52**(13-14): p. 3197-3204.
66. J.A. Diez, A.G., Gonzalez, and L., Kondic, *On the breakup of fluid rivulets.* Phys. Fluids, 2009. **21**(8): p. 082105.
67. A. Daerr, J., Eggers, L., Limat, and N., Valade, *General mechanism for the meandering instability of rivulets of newtonian fluids.* Phys. Rev. Lett., 2011. **106**(18): p. 184501.
68. H.H. Saber, M.S., El-Genk *On the breakup of a thin liquid film subject to interfacial shear.* J. Fluid Mech., 2004. **500**: p. 113-133.
69. Politovich, M.K., *Aircarft icing* 2003, National Center for Atomospheric Reasrch: Boulder, CO, USA. p. 68-75.
70. S.A. Kulinich, S., Farhadi, K., Nose, K., and X.W., Du, *Superhydrophobic surfaces: Are they really ice-repellent?* Langmuir, 2010. **27**(1): p. 25-29.
71. C. Antonini, M., Innocenti, T., Horn, M., Marengo, and A., Amirfazli, *Understanding the effect of superhydrophobic coatings on energy reduction in anti-icing system.* Cold Reg. Sci. Technol., 2011. **67**(1-2): p. 58-67.

72. L. Boinovich, A.M., Emelyanenko, V.V., Korolev, and S.A., Pashinin, *Effect of wettability on sessile drop freezing: When superhydrophobicity stimulates an extreme freezing delay.* Langmuir 2014. **30**(6): p. 1659–1668.
73. L. Cao, A.K., Jones, V.K., Sikka, J., Wu, and D., Gao, *Anti-icing superhydrophobic coatings.* Langmuir, 2009. **25**(21): p. 12444-12448.
74. S. Moghtadernejad, M., Mohammadi, M., Jadidi, M., Tembely, and A., Dolatabadi *Shear driven droplet shedding on surfaces with various wettabilities.* SAE Int. J. Aerosp., 2013. **6**(2): p. 459-464.
75. A.D. Schleizer, R.T.J., Bonnecaze, *Displacement of a two-dimensional immiscible droplet adhering to a wall in shear and pressure-driven flows.* J. Fluid Mech., 1999. **383**(1): p. 29-54.
76. T.G. Myersa, H.X., Liang, and B., Wetton, *The stability and flow of a rivulet driven by interfacial shear and gravity.* Int. J. Non-Linear Mech., 2004. **39**(8): p. 1239-1249.
77. C. Antonini, F.J., Carmona, E.M., Pierce, M., Marengo, and A., Amirfazli *General methodology for evaluating the adhesion force of drops and bubbles on solid surfaces.* Langmuir, 2009. **25**(11): p. 6143–6154.
78. M.D. Abramo, P.J., Magelhaes, and J.S., Ram, *Image processing with ImageJ.* Biophotonics Int., 2004. **11**(7): p. 36-42.
79. S. Moghtadernejad, M., Jadidi, N., Esmail, and A., Dolatabadi, *Shear driven droplet coalescence and rivulet formation.* J. Mech. Eng. Sci., 2015.
80. S. Moghtadernejad, M., Jadidi, M., Tembely, N., Esmail, and A., Dolatabadi, *Concurrent droplet coalescence and solidification on surfaces with various wettabilities* in *4th Joint US-European Fluids Engineering Summer Meeting*. 2014: Chicago, IL, USA
81. S. Jung, K.M., Tiwari, V.N., Doan, and D., Poulikakos *Mechanism of supercooled droplet freezing on surfaces.* Nature Commun., 2012. **3**(615).
82. D. Aarts, H., Lekkerkerker, H., Guo, G., Wegdam, and D., Bonn, *Hydrodynamics of droplet coalescence.* Phys. Rev. Lett., 2005. **95**: p. 164503.
83. S. Moghtadernejad, M., Tembely, M., Jadidi, N., Esmail, and A., Dolatabadi, *Shear driven droplet shedding and coalescence on a superhydrophobic surface.* Phys. Fluids, 2015. **27**(3).
84. ESI-OpenCFD. *Home OpenFOAM*. 2014; Available from: http://www.openfoam.com.
85. R. Scardovelli, S., Zaleski, *Direct numerical simulation of free-surface and interfacial flow.* Annu. Rev. Fluid Mech., 1999. **31**(1): p. 567-603.
86. J.U. Brackbill, D.B., Kothe, and C., Zemach, *A continuum method for modeling surface tension.* J. Comput. Phys., 1992. **100**(2): p. 335-354
87. Rusche, H., *Computational fluid dynamics of dispersed two phase flows at high phase fractions* 2002, Imperial College University of London.
88. Kistler, S.F., *Hydrodynamics of wetting* 1993, Marcel Dekker Inc.: New York. p. 311–429.
89. Vreman, A.W., *An eddy-viscosity subgrid-scale model for turbulent shear flow: Algebraic theory and applications.* Phys. Fluids 2004. **16**(10): p. 3670.
90. C. Fureby, G., Tabor, H.G., Weller, and A.D., Gosman, *A comparative study of subgrid scale models in homogeneous isotropic turbulence.* Phys. Fluids, 1997. **9**: p. 1416.
91. Yoshizawa, K., Horiuti, *A statistically-derived subgrid-scale kinetic energy model for the large-eddy simulation of turbulent flows* J. Phys. Soci. Japan, 1985. **54**: p. 2834-2839
92. S. Moghtadernejad, M., Jadidi, M., Tembely, N., Esmail, and A., Dolatabadi, *Concurrent droplet coalescence and solidification on surfaces with various wettabilities.* ASME J. Fluids. Eng, 2015. **137**(7).
93. B. Carroll, C., Hidrovo, *Droplet detachment mechanism in a high-speed gaseous micro flow.* J. Fluids Eng, 2013. **135**(7): p. 071206-8.

94. F. Capizzano, E., Luliano, *A Eulerian method for water droplet impingement by means of an immersed boundary technique.* J. Fluids Eng., 2014. **136**(4): p. 040906-8.
95. R. Li, N., Ashgriz, and S., Chandra, *Maximum spread of droplet on solid surface: Low Reynolds and Weber numbers.* J. Fluids Eng., 2010. **132**(6): p. 061302-5.
96. Rein, M., *Phenomena of liquid drop impact on solid and liquid surfaces.* Fluid Dyn. Res., 1993. **12**: p. 61-93.
97. Y.P. Wan, H., Zhang, X.Y., Jiang, S., Sampath, and V., Prasad, *Role of solidification, substrate temperature and Reynolds number on droplet spreading in thermal spray deposition: Measurements and modeling.* J. Heat Transfer, 2000. **123**(2): p. 382-389.
98. D. Li, Z., Chen *Experimental study on instantaneously shedding frozen water droplets from cold vertical surface by ultrasonic vibration.* Exp. Therm. Fluid Sci., 2014. **53**: p. 17-25.
99. G. McAlister, R., Ettema, and J.S., Marshall, *Wind-driven rivulet breakoff and droplet flows in microgravity and terrestrial gravity conditions.* J. Fluids Eng., 2004. **127**(2): p. 257-266.
100. D.M. Anderson, M.G., Worster, and S.H., Davis, *The case for a dynamic contact angle in containerless solidification.* J. Cryst. Growth, 1996. **163**(3): p. 329-338.
101. O.R. Enríquez, A.G., Marín, K.G., Winkels, H., Jacco, and J.H., Snoeijer *Freezing singularities in water drops.* Phys. Fluids, 2012. **24**(9): p. 091102.
102. S. Jung, K.M., Tiwari, and D., Poulikakos, *Frost halos from supercooled water droplets.* PNAS, 2012. **109**(40): p. 16073-16078.
103. S. Farhadi, M., Farzaneh, and S.A., Kulinich, *Anti-icing performance of superhydrophobic surfaces.* Appl. Surf. Sci., 2011. **257**(14): p. 6264-6269.
104. K.A. Wier, T.J., McCarthy, *Condensation on ultrahydrophobic surfaces and its effect on droplet mobility: Ultrahydrophobic surfaces are not always water repellant.* Langmuir, 2006. **22**(6): p. 2433-2436.
105. X. Xio, Y.T., Cheng, B.W., Sheldon, and J., Rankin, *Condensed water on superhydrophobic carbon films.* J. Mater. Res., 2008. **23**(8): p. 2174-2178.
106. R. Karmouch, G.G., Ross, *Experimental study on the evolution of contact angles with temperature near the freezing point.* J. Phys. Chem. C., 2010. **114**(9): p. 4063-4066.
107. R.D. Nareh, D.A., Beysens, *Growth dynamics of water drops on a square-pattern rough hydrophobic surface.* Langmuir, 2007. **23**(12): p. 6486-6489.
108. B. Mockenhaupt, H., Ensikat, M., Spaeth, and W., Barthlott, *Superhydrophobicity of biological and technical surfaces under moisture condensation: stability in relation to surface structure.* Langmuir, 2008. **24**(23): p. 13591-13597.
109. K. Varanasi, T., Deng, J.D., Smith, M., Hsu, and N., Bhate, *Frost formation and ice adhesion on superhydrophobic surfaces.* Appl. Phys. Lett., 2010. **97**(23): p. 234102-234102-3.
110. R. Menini, Z., Ghalmi, and M., Farzaneh, *Highly resistant icephobic coatings on aluminum alloys.* Cold Reg. Sci. Technol., 2011. **65**(1): p. 65-69.
111. S.A. Kulinich, M., Farzaneh, *On ice-releasing properties of rough hydrophobic coatings.* Cold Reg. Sci. Technol., 2011. **65**(1): p. 60-64.
112. H.J. Ensikat, A.J., Schulte, K., Koch, and W., Barthlott, *Droplets on superhydrophobic surfaces: Visualization of the contact area by cryo-scanning electron microscopy.* Langmuir, 2009. **25**(22): p. 13077-13083.
113. S. Moghtadernejad, M.J., N., Esmail, and A. Dolatabadi, *SPH simulation of rivulet dynamics on surfaces with various wettabilities.* SAE Int. J. Aerosp, 2015.
114. S. Moghtadernejad, M., Jadidi, N., Esmail, and A., Dolatabadi. *Shear driven rivulet dynamics on surfaces with various wettabilities*. in *ASME 2014 International Mechanical Engineering Congress & Exhibition*. 2014. Montreal.

115. Lucy, L.B., *A numerical approach to the testing of the fission hypothesis.* The Astronomical J., 1977. **82**: p. 1013-1024.
116. R.A. Gingold, J.J., Monaghan, *Smoothed particle hydrodynamics-theory and application to non-spherical stars.* Monthly Notices of the R. Astronomical Soci., 1977. **181**: p. 375-389.
117. Monaghan, J.J., *Smoothed particle hydrodynamics.* Annu. Rev. of Astronomy and Astrophysics, 1992. **30**: p. 543-574.
118. Monaghan, J.J., *Simulating free surface flows with SPH.* J. Comput. Phys., 1994. **110**(2): p. 399-406.
119. A. Crespo, M., Gómez-Gesteira, and R., Dalrymple, *Boundary conditions generated by dynamic particles in SPH methods.* CMC Tech. Sci. Press, 2007. **5**(3): p. 173.
120. Monaghan, J.J., *Smoothed particle hydrodynamics and its diverse applications.* Annu. Rev. Fluid Mech., 2012. **44**: p. 323-346.
121. J.J. Monaghan, A., Kocharyan, *SPH simulation of multi-phase flow.* Computer Phys. Commun., 1995. **87**(1): p. 225-235.
122. Monaghan, J.J., *Why particle methods work.* SIAM J. on Scientific and Statistical Computing, 1982. **3**(4): p. 422-433.
123. G. Liu, M.B., Liu, *Smoothed particle hydrodynamics: A meshfree particle method*. 2003: World Scientific.
124. Monaghan, J.J., *Smoothed particle hydrodynamics.* Reports on progress in physics, 2005. **68**(8): p. 1703.
125. M.B. Liu, G.R., Liu, *Smoothed particle hydrodynamics (SPH): An overview and recent developments.* Archives of Comput. methods in Eng., 2010. **17**(1): p. 25-76.
126. Benz, W., *Applications of Smoothed Particle Hydrodynamics (SPH) to astrophysical problems.* Computer Phys. Commun., 1988. **48**(1): p. 97-105.
127. F. Sun, M., Tan, and J.T., Xing. *Air-water two phase flow simulation using smoothed particle hydrodynamics*. in *2nd International Conference on Violent Flows*. 2012.
128. M. Müller, D., Charypar, and M., Gross. *Particle-based fluid simulation for interactive applications*. in *Proceedings of the 2003 ACM SIGGRAPH/Eurographics symposium on Computer animation*. 2003. Eurographics Association.
129. M. Müller, B., Solenthaler, R., Keiser, and M., Gross. *Particle-based fluid-fluid interaction*. in *Proceedings of the 2005 ACM SIGGRAPH/Eurographics symposium on Computer animation*. 2005. ACM.
130. Crespo, A., *Application of the Smoothed Particle Hydrodynamics model SPHysics to free-surface hydrodynamics*. 2008, PhD thesis.
131. P.W. Randles, L.D., Libersky, *Smoothed particle hydrodynamics: Some recent improvements and applications.* Computer methods in Appl. Mech. and Eng., 1996. **139**(1): p. 375-408.
132. J.J. Monaghan, a.J.C., Lattanzio, *A refined particle method for astrophysical problems.* Astronomy and Astrophysics, 1985. **149**: p. 135-143.
133. H. Xiong, J., Zhu, *Study of droplet deformation, heat-conduction and solidification using incompressible smoothed particle hydrodynamics method.* J. Hydrodynamics, Ser. B, 2010. **22**(5): p. 150-153.
134. M. Ellero, M., Serrano, and P., Espanol, *Incompressible smoothed particle hydrodynamics.* J. Comput. Phys., 2007. **226**(2): p. 1731-1752.
135. S. Lind, R., Xu, P., Stansby, and B., Rogers, *Incompressible smoothed particle hydrodynamics for free-surface flows: A generalised diffusion-based algorithm for stability and validations for impulsive flows and propagating waves.* J. Comput. Phys., 2012. **231**(4): p. 1499-1523.
136. J. Morris, P., Fox, and Y., Zhu, *Modeling low Reynolds number incompressible flows using SPH.* J. Comput. Phys., 1997. **136**(1): p. 214-226.

137. B. Solenthaler, R., Pajarola, *Predictive-corrective incompressible SPH.* ACM Trans. Graph., 2009. **28**(3): p. 1-6.
138. X. Hu, N., Adams, *An incompressible multi-phase SPH method.* J. Comput. Phys., 2007. **227**(1): p. 264-278.
139. Zhang, M., *Simulation of surface tension in 2D and 3D with smoothed particle hydrodynamics method.* J. Comput. Phys., 2010. **229**(19): p. 7238-7259.
140. S. Šikalo, H.D., Wilhelm, I.V., Roisman, S., Jakirliæ, and C., Tropea, *Dynamic contact angle of spreading droplets: Experiments and simulations.* Phys. Fluids, 2005. **17**(6): p. 062103.
141. S. Afkhami, S., Zaleski, and M., Bussmann, *A mesh-dependent model for applying dynamic contact angles to VOF simulations.* J. Comput. Phys., 2009. **228**(15): p. 5370-5389.
142. A. Tartakovsky, P., Meakin, *Modeling of surface tension and contact angles with smoothed particle hydrodynamics.* Phys. Rev. E, 2005. **72**(2): p. 026301.
143. Verlet, L., *Computer experiments on classical fluids. I. Thermodynamical properties of Lennard-Jones molecules.* Phys. Rev., 1967. **159**(1): p. 98.
144. T.R. Saitoh, J., Makino, *A necessary condition for individual time steps in SPH simulations.* The Astrophysical J. Lett., 2009. **697**(2): p. L99.
145. H. Xiong, L., Chenand, and J., Lin, *Smoothed particle hydrodynamics modeling of free surface flow.* J. Hydrodynamics, Ser. B, 2006. **18**(3): p. 443-445.
146. Roy, T.M., *Physically based fluid modeling using smoothed particle hydrodynamics*. 1995, University of Illinois at Chicago.
147. Liu, G., *Meshfree methods: Moving beyond the finite element method*. 2010: CRC press.
148. Z. Yao, J., Wang, G., Liu, and M., Cheng, *Improved neighbor list algorithm in molecular simulations using cell decomposition and data sorting method.* Computer Phys. Commun., 2004. **161**(1): p. 27-35.
149. R.A. Dalrymple, B.D., Rogers, *Numerical modeling of water waves with the SPH method.* Coastal Eng., 2006. **53**(2): p. 141-147.
150. A. Colagrossi, M., Landrini, *Numerical simulation of interfacial flows by smoothed particle hydrodynamics.* J. Comput. Phys., 2003. **191**(2): p. 448-475.
151. M. Liu, J., Shao, and J., Chang, *On the treatment of solid boundary in smoothed particle hydrodynamics.* Sci. China Technol. Sci., 2012. **55**(1): p. 244-254.

Appendices

A. Image Processing

The experimental images of this work are taken by Photron high speed camera (Photron SA1.1, USA) with 5400 frames/s for the droplet and 2000 frames/s for the rivulet experiments with the resolution of 1024×1024. In order to obtain quantitative values for the droplet wetting lengths, contact angles and rivulet thickness, ImageJ software was for post processing the results. The main use of ImageJ is for automating the measurements of hundreds of images taken by the high speed camera. ImageJ can adjust the brightness, create binary images and track the boundaries. ImageJ creates a binary image based on the contrast between the droplet/rivulet and their background. In this matter the light intensity of each individual pixel of the recorded image is compared to the intensity of its background. If the difference is within 2%, the pixel is assumed to be part of the background. By setting all light intensities above the threshold to white and all those below the threshold to black, a binary image is created from the grey scale image. The trajectory of droplet and rivulet is then measured based on this binary image. The 50% threshold is compared to a 90% and 10% threshold (depicted in Figure A.1) for approximating the error associated with conversion to binary. The gray zone in the middle image demonstrates a region that is supposed to be a droplet if a threshold between 10% and 90% is used.

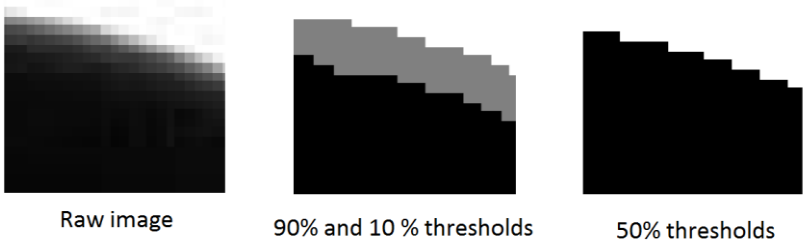

Figure A.1 Threshold variation in boundary detection

To determine the actual length scales, the size that each pixel in the image represents is required. To do so, ImageJ software is calibrated based on the image taken from an object with a known size (the object size is measured by a vernier caliber). The uncertainty of the meurmnets is dependent to the the image size, resolution and the number of pixels per dimeter of the droplet/ rivulet. Each pixel in the experimental images of droplet and rivulet of this work represents 15 and 30 µm of length scale, respectively.

B. Flat Plate

It was mentioned in the droplet experiments that the droplet was put at about 10 mm away from the leading edge of the plate. To make the clear analysis of the air flow pattern around the flat plate k-ω SST simulation was performed with ANSYS sofware. The numerical domain consisted of 230,000 hexahedral computational cells with the size of 90 µm. The boundary conditions were fixed as uniform velocity at the inlet, pressure outlet and no slip boundary at the wall. As there is 5 cm distance between the velocity inlet and the leading edge of the plate so the air flow will be developed by the time it reaches the droplet. Hence using uniform air flow in the simulation does not significantly affect the results. The stream lines around the flat plate are shown in Figure B.1 for 90 m/s of air speed.

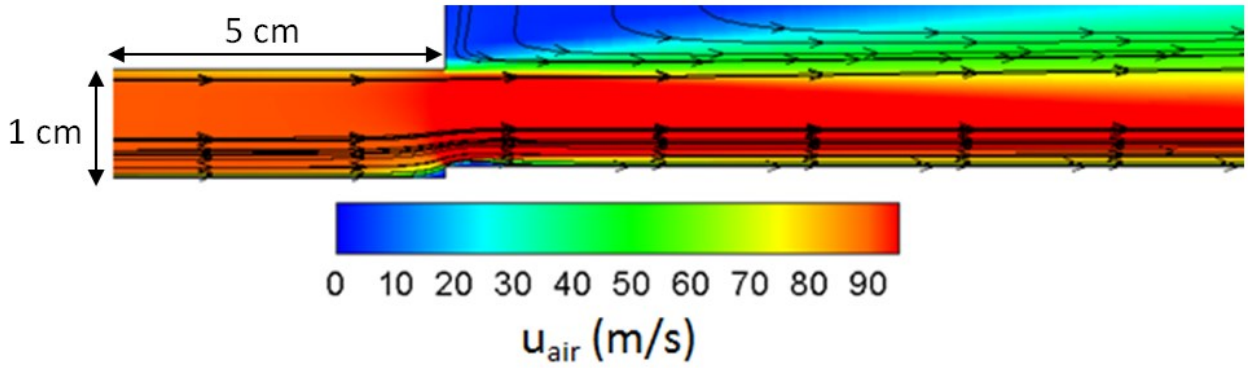

Figure B.1 Stream lines and velocity contours over the flat plate for 90 m/s of air speed

As it is indicated in Figure B.1 at about 1 cm away from the leading edge of the plate the flow is smooth and without any vortices. Based on Blasious boundary layer approximation the thickness of the boundary layer at 1 cm away from the leading edge of the plate is found to be 50 μm which is about 40 times smaller than the diameter of the droplet (2.1 mm). In other words more than 75% of the droplet area will be out of the boundary layer and will be affected by the inlet velocity. The maximum thickness of the boundary layer at the end of the plate (x= 9 cm) is found to be 0.7 mm.

C. Accuracy Analysis

It was mentioned in the thesis that the experiments were repeated at least fifteen times to reach acceptable degree of accuracy and repeatability and the results were reported based on the average values of those fifteen experiments. It should be noted that the reported experimental length scales in droplet wetting length and rivulet thickness have the standard deviation of 0.1 and 0.03 mm, respectively. The standard deviation of the reported contact angles is 1.2°.